UNIVERSITY OF OKLAHOMA

GRADUATE COLLEGE

# AN ULTRAVIOLET SURVEY OF THE DA WHITE DWARF POPULATION OF THE GALAXY

A DISSERTATION

SUBMITTED TO THE GRADUATE FACULTY

in partial fulfillment of the requirements for the

Degree of

DOCTOR OF PHILOSOPHY

By

RENAE E. WALL
Norman, Oklahoma
2023

Downloaded from SHAREOK. Persistent Handle URL: https://hdl.handle.net/11244/337948

AN ULTRAVIOLET SURVEY OF THE DA WHITE DWARF POPULATION OF THE GALAXY

A DISSERTATION APPROVED FOR THE
HOMER L. DODGE DEPARTMENT OF PHYSICS AND ASTRONOMY

BY THE COMMITTEE CONSISTING OF

Dr. Mukremin Kilic, Chair

Dr. Nathan Kaib

Dr. Xinyu Dai

Dr. Michael G Strauss

Dr. Kerry Magruder

© Copyright by RENAE E. WALL 2023
All Rights Reserved.

To my father, Eric Wall, who was always willing to listen and ask questions until he understood.

To my mother, Sandra Wall, who talked me through all my tears and wrote ”The Very Best”, which got her youngest daughter through qualifying exams, many years before she was born.

To my brother, Aaron Wall, who endured many rants over Skype.

To my sister, Audrey Wall, who began blazing this trail. For you I now complete the journey.

# Acknowledgements

Just as no man is an island, no dissertation can be created alone. I would like to take this time to thank all of the people who have made this work possible.

To my advisor, Dr. Mukremin Kilic, I thank you for all your guidance, encouragement, patience, and understanding. Without your support, I would not have been able to complete my doctorate, nor would I have half the skills and confidence I have now.

Thank you to Dr. Timothy Miller, Dr. Jenna Nugent, Dr. Hora Mishra, Dr. Alekzander Kosakowski, Dr. Kyra Dame, and all of the wonderful, crazy friends I made throughout my journey through grad school. Words cannot adequately express just how much your friendships mean to me. I will never forget all of the late night conversations we had when we'd lost our minds from too much studying. I still have pictures of our glorious black/whiteboard murals.

I thank my family for all their support and prayers. Thank you for having faith in me when I had no faith in myself.

I would particularly like to thank Dr. Michael G. Strauss. You have been an incredible example of what a Christian scientist should look like. All of the discussions we had during "Dr. Strauss Book Club" meetings had an immense impact on my life and my time in graduate school.

I would finally like to acknowledge the contributions of my committee members, Dr. Nathan Kaib, Dr. Kerry Magruder, and Dr. Xinyu Dai. Thank you for sticking with me through this journey.

# Table of Contents

**Abstract** **vii**

**1 Introduction** **1**
1.1 White Dwarf Stars . . . 1
1.2 What Can a White Dwarf Tell Us? . . . 2
1.3 Why Ultraviolet? . . . 3
1.4 GALEX . . . 4
1.5 Measuring the Ruler . . . 6
1.6 Extinction . . . 8
1.7 Dissertation Overview . . . 9

**2 GALEX Absolute Calibration and Extinction Coefficients Based on White Dwarfs** **11**
2.1 Introduction . . . 11
2.2 Sample Selection . . . 12
2.3 Synthetic Magnitudes . . . 13
2.4 GALEX Photometric Calibration . . . 13
2.5 Extinction Coefficients . . . 16
2.6 Outliers . . . 20
2.7 Conclusions . . . 22
2.8 Acknowledgements . . . 23
Appendix . . . 24
2.A 100 pc Sample . . . 24
2.B 250 pc Sample . . . 34

**3 A GALEX view of the DA White Dwarf Population** **53**
3.1 Introduction . . . 53
3.2 Sample Selection . . . 54
3.3 The Fitting Procedure . . . 55
3.4 Results from Temperature Comparison . . . 55
3.4.1 The 100 pc SDSS Sample . . . 55
3.4.2 The MWDD DA sample . . . 60
3.5 Results from UV Magnitude Comparison . . . 74
3.6 Conclusions . . . 79

**4 Conclusions** **80**
4.1 Chapter Summaries . . . 80
4.1.1 Chapter 2 . . . 80
4.1.2 Chapter 3 . . . 81
4.2 Future Work . . . 82

4.2.1 ULTRASAT . . . . . 82
4.2.2 Binaries . . . . . 83
4.2.3 Pulsations . . . . . 83
4.2.4 Beyond DA white dwarfs . . . . . 83

# Abstract

DA white dwarfs are the most common type of white dwarf in our Galaxy. Hence, it is important to study the DA white dwarf population as thoroughly as possible. In this dissertation, I present our work using the Galaxy Evolution Explorer (GALEX) data to study the DA white dwarf population in the ultraviolet.

I begin by presenting our use of 1837 DA white dwarfs with high signal-to-noise ratio spectra and *Gaia* parallaxes to verify the absolute calibration and extinction coefficients for GALEX. We use white dwarfs within 100 pc to verify the linearity correction to the GALEX data. We find that the linearity correction is valid for magnitudes brighter than 15.95 and 16.95 for the far-ultraviolet (FUV) and near-ultraviolet (NUV) bands, respectively. We also use DA white dwarfs beyond 250 pc to calculate extinction coefficients in the FUV and NUV bands: $R_{\rm FUV} = 8.01 \pm 0.07$ and $R_{\rm NUV} = 6.79 \pm 0.04$. These are consistent with the predicted extinction coefficients for Milky Way-type dust in the FUV, but smaller than predictions in the NUV. With well understood optical spectra and state-of-the-art model atmosphere analysis, these white dwarfs currently provide the best constraints on the extinction coefficients for the GALEX data.

I then present our detailed model atmosphere analysis of 14001 DA white dwarfs from the Montreal White Dwarf Database with ultraviolet photometry from the GALEX mission. We use the 100 pc sample, where the extinction is negligible, to demonstrate that there are no major systematic differences between the best-fit parameters derived from optical only data and the optical + UV photometry. GALEX FUV and NUV data improve the statistical errors in the model fits, especially for the hotter white dwarfs with spectral energy distributions that peak in the UV. Fitting the UV to optical spectral energy distributions also reveals UV-excess or UV-deficit objects. We use two different methods to identify outliers in our model fits. Known outliers include objects with unusual atmospheric compositions, strongly magnetic white dwarfs, and binary white dwarfs, including double degenerates and white dwarf + main-sequence systems. We present a list of 89 newly identified outliers based on GALEX UV data; follow-up observations of these objects will be required to constrain their nature.

I then conclude by discussing future work in UV observations of white dwarfs. Several current and upcoming large scale spectroscopic surveys are targeting $> 10^5$ white dwarfs. In addition, the ULTRASAT mission is planning an all-sky survey in the NUV band. A combination of the UV data from GALEX and ULTRASAT and optical data on these large samples of spectroscopically

confirmed DA white dwarfs will provide an excellent opportunity to identify unusual white dwarfs in the solar neighborhood.

# CHAPTER 1

# Introduction

It is human nature to be endlessly curious. Just ask any parent of a small child and they will regale you with tales of all the strange and dangerous things their child has tried to put in its mouth. From the moment we are born, we are driven to explore and understand our surroundings. It is this spirit of curiosity that drives astronomers to understand objects that are so far removed from the daily lives of the majority of Earth's over 7 billion inhabitants as to be considered inconsequential to most.

The objects studied within this dissertation are so faint that, although they are within our own galaxy, they cannot be seen with the naked eye. The objects we seek to understand are white dwarf stars. Let us begin with a definition.

## 1.1. White Dwarf Stars

White dwarfs are the end stage of life for the majority of all stars. Stars with masses $\leq 8 - 10$ $M_\odot$ ($\approx$97% of all stars) will evolve into white dwarfs (Fontaine, Brassard, & Bergeron, 2001). White dwarfs typically have a mass around 0.6 $M_\odot$ and radii comparable to Earth's ($\approx 0.01$ $R_\odot$).

During a star's main sequence lifetime, it burns through the hydrogen in the core. Once all the hydrogen has been burned inside the core, all that is left is a thin shell of hydrogen burning around a core of helium ash all surrounded by an envelope of inert hydrogen. Once there is no burning in the core, the core will begin to collapse due to gravity until it reaches the temperature and pressure required to burn helium. While the core is collapsing, the hydrogen burning shell must maintain the same temperature in order to sustain hydrogen burning. In order to maintain the temperature of the hydrogen burning shell, the envelope's temperature must decrease as the core's temperature increases. The same principle holds for the envelope's pressure. As the core's pressure increases, the envelope's pressure must decrease to maintain the proper pressure for hydrogen burning in the shell. This is called the mirror principle. Whatever temperature and pressure changes happen in the core, the opposite changes must happen in the envelope so that the temperature and pressure can be maintained in the hydrogen shell between the core and envelope. So as the core contracts and heats, the envelope cools and expands.

Once the central temperature reaches $\approx 10^8$K, helium burning will begin in the core. Once helium has been exhausted in the core, we are left with a core of carbon and oxygen ash surrounded by first a helium burning shell, then a hydrogen burning shell, all within an inert hydrogen envelope.

When helium is exhausted in the core, it again begins to collapse under the affects of gravity causing the envelope to expand again due to the mirror principle. Depending on the star's mass, the core may or may not be able to begin carbon burning. After the final core burning stage, whether that be helium or carbon, the core begins to contract one last time. As the density of the core increases, the electrons are no longer bound to individual atoms, but are instead shared equally among nearly all the atoms in the core. This makes the core analogous to a single molecule. The Pauli exclusion principle states that no two electrons can share the same energy state. Electrons are therefore forced into higher and higher energy states, greatly increasing their momentum. The highest energy electrons move near the speed of light and carry enough momentum to support the core against the force of gravity. This is called electron degeneracy pressure. During the final core contraction, the energy created by the hydrogen, helium, and (in some cases) carbon burning shells will cause the envelope to rapidly expand, leading to mass loss. What is left is a degenerate core composed of either carbon and oxygen (if only helium was burned) or oxygen and neon (if carbon was burned). This core is surrounded by a thin atmosphere of hydrogen and/or helium.

Now that you know what a white dwarf is, the next logical question is why we study them. What can a dead star possibly teach us?

### 1.2. What Can a White Dwarf Tell Us?

So far you know a little about the state of matter that comprises the majority of a white dwarf. Extremely high temperatures and pressure create an electron degenerate plasma. Now that we know that such a state of matter exists, we naturally want to know how it works. However, the extreme conditions that occur naturally inside a white dwarf cannot be reproduced here on Earth. The only way to further understand this extreme state of matter is by observing white dwarfs.

Since white dwarfs are no longer producing energy via nuclear fusion and can no longer collapse via gravity due to electron degeneracy pressure, the only thing a white dwarf will do after its formation is cool. Thanks to white dwarf cooling models, we can determine how long a white dwarf has been around (Bergeron, Leggett, & Ruiz, 2001). Using the initial - final mass ratio, we can determine what the main sequence mass of a white dwarf originally was, allowing us to determine how long it took the star to become a white dwarf. Add the cooling age to the main sequence age and you have the total age of the white dwarf. We can use the ages of white dwarfs to estimate the ages of different galactic populations (Mestel, 1952; Winget et al., 1987; Liebert, Dahn, & Monet, 1988).

White dwarfs are thought to be the progenitors of type Ia supernovae (SN Ia). SN Ia occur when a white dwarf nears the Chandrasekhar mass limit ($1.4M_{\odot}$) (Chandrasekhar, 1931). Above this mass, electron degeneracy pressure can no longer support the star against gravity. As a white dwarf approaches this mass limit (for example by accreting matter from a binary companion), the

density in the core will become sufficient to begin carbon burning. The energy produced by carbon burning causes the temperature of the white dwarf to increase, increasing the speed of the carbon burning until it reaches thermonuclear runaway. The resulting explosion completely destroys the white dwarf (Wheeler, 2000). SN Ia are used as standard candles. A standard candle is an object whose absolute magnitude is thought to be well known. If we know an object's absolute magnitude, we can use its apparent magnitude to measure the distance to that object. Since SN Ia are critical in measuring extragalactic distances, a better understanding of the white dwarf population can improve our understanding of SN Ia.

In addition to being a possible progenitor of SN Ia, close white dwarf binary systems are also an important source of gravitational waves. Over time these white dwarfs will spiral closer and closer to each other as they lose energy due to the emission of gravitational waves. Eventually these double degenerate systems will merge. The merger of these binaries will be the dominant source of the gravitational wave foreground for the upcoming *Laser Interferometer Space Antenna* (*LISA*) mission (Nelemans, Yungelson, & Portegies Zwart, 2001; Korol, Rossi, & Barausse, 2019; Nissanke et al., 2012; Korol et al., 2017; Lamberts et al., 2019).

Now that you have a broad idea of the type of information that can be gained by studying white dwarfs, let us move into more of the specifics of this dissertation. In particular we need to discuss the study of white dwarfs in the ultraviolet.

### 1.3. Why Ultraviolet?

Luckily for us Earth's atmosphere blocks most ultraviolet (UV) wavelengths; but, while they are extremely harmful to humans, UV is a critical component for the understanding of white dwarfs. For the hottest white dwarfs, the peak wavelength of their black body radiation is in the UV. To obtain the most accurate measurement of the effective temperature ($T_{\rm eff}$) of hot white dwarfs, UV data must be obtained.

UV data can also reveal interesting features in a white dwarfs' atmosphere that are not seen in optical bands. $25-50\%$ of white dwarfs are contaminated by metals (Koester, Gänsicke, & Farihi, 2014). Since most metal lines are in the UV, astronomers can gain a better understanding of the atmospheric abundances of different metals using UV data. White dwarfs with strong magnetic fields can be revealed by studying UV data. Strong magnetic fields shift the absorption features and wash them out, greatly affecting the UV output of the white dwarf. For example, the magnetic white dwarf PG 1031+234 has a very flat spectral energy distribution (SED) in the UV but a very steep slope in the optical and infrared (IR) (Schmidt et al., 1986). Schmidt et al. (1986) attempted to fit the SED using nonmagnetic white dwarf models. They found that a $T_{\rm eff} = 15000$K model fit the UV portion of the SED but failed to fit the optical/IR portion while a $25000$K model fit the optical/IR but could not fit the UV. A similar principle holds true for some white dwarfs with mixed atmospheres.

While a pure hydrogen model might be able to fit a mixed hydrogen/helium atmosphere fairly well in the optical, the same model might not be able to fit the UV data.

UV data can also reveal unseen binary companions. For white dwarf + M dwarf systems, the M dwarf will dominate in redder bands while the white dwarf will dominate in the UV. It is easier to separate the two components with the addition of UV data. In the case of double degenerate systems, if there is a significant temperature difference between the two white dwarfs, one will dominate in the UV.

A good example of the use of UV data to find unusual white dwarfs is Lajoie & Bergeron (2007). In Lajoie & Bergeron (2007) they compared the effective temperatures obtained from the optical and UV spectra of 140 DA white dwarfs from the *International Ultraviolet Explorer* (*IUE*) archive. They found that the optical and UV temperatures of the majority of stars cooler than 40000 K and within 75 pc are in fairly good agreement with $\Delta T_{\rm eff}/T_{\rm optical} \leq 10\%$. They also found that the majority of the discrepancies between the two temperature measurements were caused by interstellar reddening, which affects the UV more than the optical. By restricting their analysis to white dwarfs within 75 pc, where the extinction is negligible, they were able to identify several double degenerate candidates, as well as a DA + M dwarf system, and stars with unusual atmospheric compositions.

We now see that UV data can be critical in furthering our understanding of white dwarfs. Since most UV wavelengths are blocked by Earth's atmosphere, we must go to space to observe them.

### 1.4. GALEX

The Galaxy Evolution Explorer (GALEX) was the first space based mission to attempt an all-sky imaging survey in the UV (Martin et al., 2005). GALEX had a Ritchey-Chretin optical design with a 50 cm diameter primary mirror[1] (see figure 1.1). It utilized large format microchannel plate detectors (MCPs). Each MCP consisted of a stack of three microchannel plates separating a photocathode and a delay line detecting anode. The MCP detector was chosen over the more typical CCD for its low background noise, high red rejection, and lack of cooling requirement. However, MCPs have lower quantum efficiency (around 8%) and poor field flatness compared to CCDs. To mitigate local flatness variations, GALEX observed in a spiral dither pattern.

The primary objective of GALEX was to study star formation and the spectral evolution of galaxies in the UV. While observing distant galaxies, many foreground UV sources were also observed. In the ten years that it was operational, GALEX surveyed 26,000 square degrees of the sky as part of the All-sky Imaging Survey (AIS) in two band passes: Far Ultraviolet (FUV) with a central wavelength of 1528 Å and Near Ultraviolet (NUV) with a central wavelength of 2271 Å (Morrissey et al., 2005).

In order to get accurate data from any instrument it is critical to first calibrate that instrument.

[1] http://www.galex.caltech.edu/researcher/techdoc-ch1.html

Fig. 1. from The OnOrbit Performance of the Galaxy Evolution Explorer
Morrissey et al. 2005 ApJL 619 L7 doi:10.1086/424734
https://dx.doi.org/10.1086/424734
© 2005. The American Astronomical Society. All rights reserved. Printed in U.S.A.

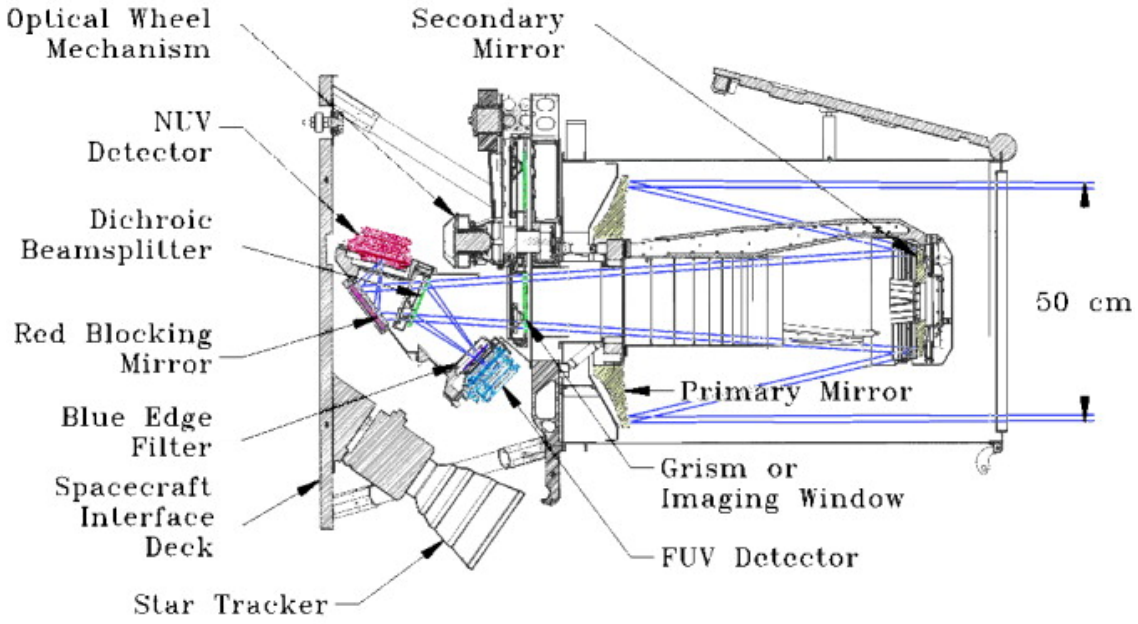


**Figure 1.1:** A cross section of the GALEX instrument. The double blue line indicates the light path.

Table 1.1. Inverse quadratic corrections from Camarota & Holberg (2014) for the FUV and NUV bands (see Eq 1.1.)

| Property | NUV | FUV |
|---|---|---|
| $c_0$ | 2.634 | 5.371 |
| $c_1$ | 26.316 | 20.000 |
| $c_2$ | -245.329 | -210.200 |

As a friend of mine put it, you need to measure your ruler.

### 1.5. Measuring the Ruler

There are many factors that must be taken into account to calibrate an instrument such as GALEX. You must determine the instrument's resolution, any background noise caused by the instrument itself, the photometric zero point, the linearity of the instrument, and many more factors. Almost all of the calibration was done on the ground in thermal vacuum and then checked once GALEX was in space (Morrissey & GALEX Science Team, 2005). In this dissertation, we are specifically interested in one particular factor: the linearity of the GALEX instrument.

There are two sources of nonlinearity in GALEX photometry: global nonlinearity and local nonlinearity. Global nonlinearity is caused by the finite time period required for the electronics to assemble photon lists and is thus well understood and easily corrected for. Local nonlinearity occurs near bright sources, making it much more difficult to correct. Morrissey et al. (2007) demonstrate that nonlinearity becomes significant ($> 10\%$) above 109 and 311 counts per second in the FUV and NUV bands, respectively (see figure 1.2). These correspond to $m_{\rm FUV} \approx 14$ mag and $m_{\rm NUV} \approx 15$ mag. Local nonlinearity complicates the standard star measurements which were used to determine the photometric zero point of GALEX.

GALEX observed 18 white dwarfs from the *Hubble Space Telescope* CALSPEC database (Bohlin, Dickinson, & Calzetti, 2001) as standard stars. However, its photometric calibration relies primarily on the dimmest star in this sample, the DB white dwarf LDS 749b, as all of the other standard stars observed are highly saturated. In fact, after Bohlin & Koester (2008) provided a better CALSPEC spectrum for LDS 749b, the GALEX magnitudes were shifted by $\approx 0.04$ mag between the GR4/5 and GR6 data releases. Hence, it is important to verify the photometric calibration using fainter stars.

Camarota & Holberg (2014) verified the GALEX photometric calibration using 99 and 107 DA white dwarfs in the FUV and NUV, respectively, with magnitudes between 10 and 17.5 from the final GR7 GALEX data release. They found that a modest linearity correction is needed in this

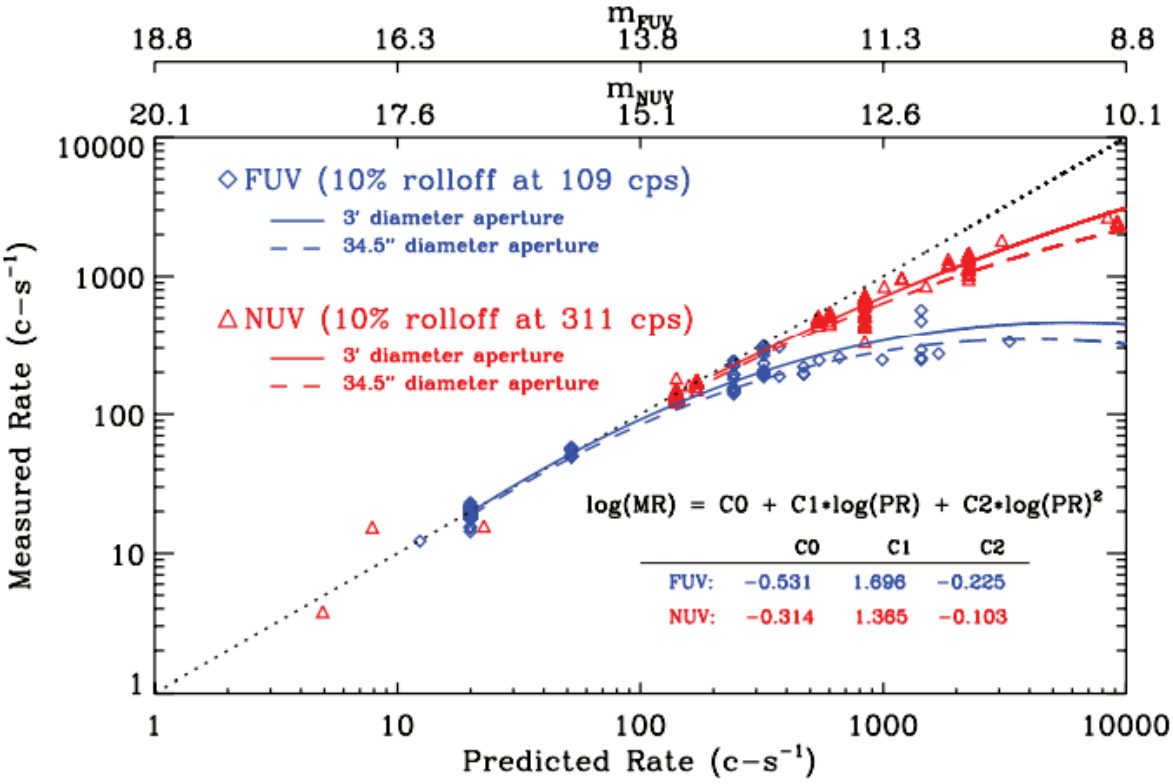


**Figure 1.2:** Figure 8 from Morrissey et al. (2007). The dotted black line is the 1:1 correlation, the red triangles are NUV measurements and the blue diamonds are FUV measurements. The red and blue solid lines are quadratic fits to the 3 arcminute diameter aperture NUV and FUV data, respectively. The red and blue dashed lines are quadratic fits to the 34.6 arcsecond diameter aperture NUV and FUV data, respectively.

magnitude range. Their corrections take the form

$$m_{\rm corr} = c_0 + (c_1 m_{\rm obs} + c_2)^{1/2}, \tag{1.1}$$

where $m_{\rm obs}$ and $m_{\rm corr}$ are the observed and corrected GALEX magnitudes, respectively. Their calculated constants $c_0$, $c_1$, and $c_2$ are given in Table 1.1. Although Camarota & Holberg (2014) postulate that their linearity correction should hold for stars as faint as 20th magnitude, they state that their corrections for stars dimmer than 16th magnitude should be treated with caution. Camarota & Holberg (2014) point out the need for a larger sample size and the characterization of extinction in the GALEX bands.

We've now discussed one factor that can affect GALEX photometry. Let us now move to another factor: extinction.

### 1.6. Extinction

The space between stars in our galaxy is not completely empty. Interstellar dust fills the void between stars. The size of this dust is such that it preferentially absorbs and scatters shorter wavelengths. As a result an object will appear to be both redder and dimmer than it actually is. Happily for us, we already have a good idea of the amount of reddening along any given line of sight. Schlafly & Finkbeiner (2011) give a fairly accurate reddening map of our galaxy. The affect of interstellar dust that concerns us in this dissertation is the amount of light absorbed by the dust: the extinction.

Extinction is quantified by an extinction coefficient. These coefficients are defined as

$$R_\lambda = \frac{A_\lambda}{E(B-V)}, \tag{1.2}$$

where $A_\lambda$ is the total absorption along the line of sight to an object and $E(B-V)$ is the reddening. There is a broad range of GALEX extinction coefficients reported in the literature. Bianchi (2011) provided theoretical estimates of $R_{\rm FUV} = 8.06$ and $R_{\rm NUV} = 7.95$ for Milky Way type dust and $R_{\rm FUV} = 12.68$ and $R_{\rm NUV} = 8.08$ for the Small Magellanic Cloud (SMC) type dust. Although theory is useful, it is preferable to collect empirical evidence for or against that theory if possible.

Yuan, Liu, & Xiang (2013) found empirical values of $R_{\rm FUV} = 4.37 - 4.89$ and $R_{\rm NUV} = 7.06 - 7.24$. They derived these extinction coefficients by using the 'standard pair' technique (Stecher, 1965). In this technique two stars of the same spectral type, one in an area with low extinction and one in an area of high extinction, are compared. The stars with low extinction are called the control sample, and the stars with high extinction are called the target sample. The stars in the control sample are used to determine the intrinsic colors of the corresponding stars in the target

sample. Yuan, Liu, & Xiang (2013) selected their initial sample from the Sloan Digital Sky Survey (SDSS) Data Release 7 (DR7). For the control sample, they selected stars with $E(B-V) < 0.03$. For their target sample, they selected stars with $E(B-V) > 0.1$. Yuan, Liu, & Xiang (2013) examined a target sample of 1396 stars and a control sample of 16405 stars from the GALEX data release GR5. Most of these stars were classified as FG dwarfs. However, there is a great deal of scatter and uncertainty in their derivation of $R_{\rm FUV}$ and $R_{\rm NUV}$, as can be seen in figure 1.3. The majority of the stars in their target sample have $T_{\rm eff} < 7000$K, so their black body curves will peak outside of the UV wavelength range. Yuan, Liu, & Xiang (2013) caution against using their GALEX extinction coefficients and state that a much larger and hotter sample is needed to derive the GALEX extinction coefficients.

### 1.7. Dissertation Overview

You now know what a white dwarf is, the type of information we can learn from their study, and why UV in particular is so important. You've been introduced to GALEX and the particular calibration factor this dissertation will focus on: linearity. You also know what extinction is and why it is so important that the GALEX extinction coefficients be re-derived.

If I have done my job correctly, you should have all the background information you need to understand this dissertation. Allow me to give you a brief walk through.

In chapter 2, I revisit the linearity calibration done by Camarota & Holberg (2014) to better constrain the magnitudes over which it is applicable. I then re-derive the GALEX extinction coefficients. I will wrap up chapter 2 by discussing some interesting objects found in my sample. Chapter 2 is a reproduction of my published work in the Monthly Notices of the Royal Astronomical Society (MNRAS) and has been reproduced with permission granted to the first-author by the copyright agreement for use in a doctoral dissertation. The reference to the original work is as follows: Wall R. E., Kilic M., Bergeron P., Rolland B., Genest-Beaulieu C., Gianninas A., 2019, MNRAS, 489, 5046.

I build off of my work from chapter 2 in chapter 3 by extending my analysis to include DA white dwarfs from the Montreal White Dwarf Database (MWDD) and data from the Panoramic Survey Telescope and Rapid Response System (Pan-STARRS). Chapter 3 is a reproduction of my published work in the Monthly Notices of the Royal Astronomical Society (MNRAS) and has been reproduced with permission granted to the first-author by the copyright agreement for use in a doctoral dissertation. The reference to the original work is as follows: Wall R. E., Kilic M., Bergeron P., Leiphart N., 2023, MNRAS, 523, 4067.

I conclude in chapter 4 with the bright future of UV in the study of white dwarfs.

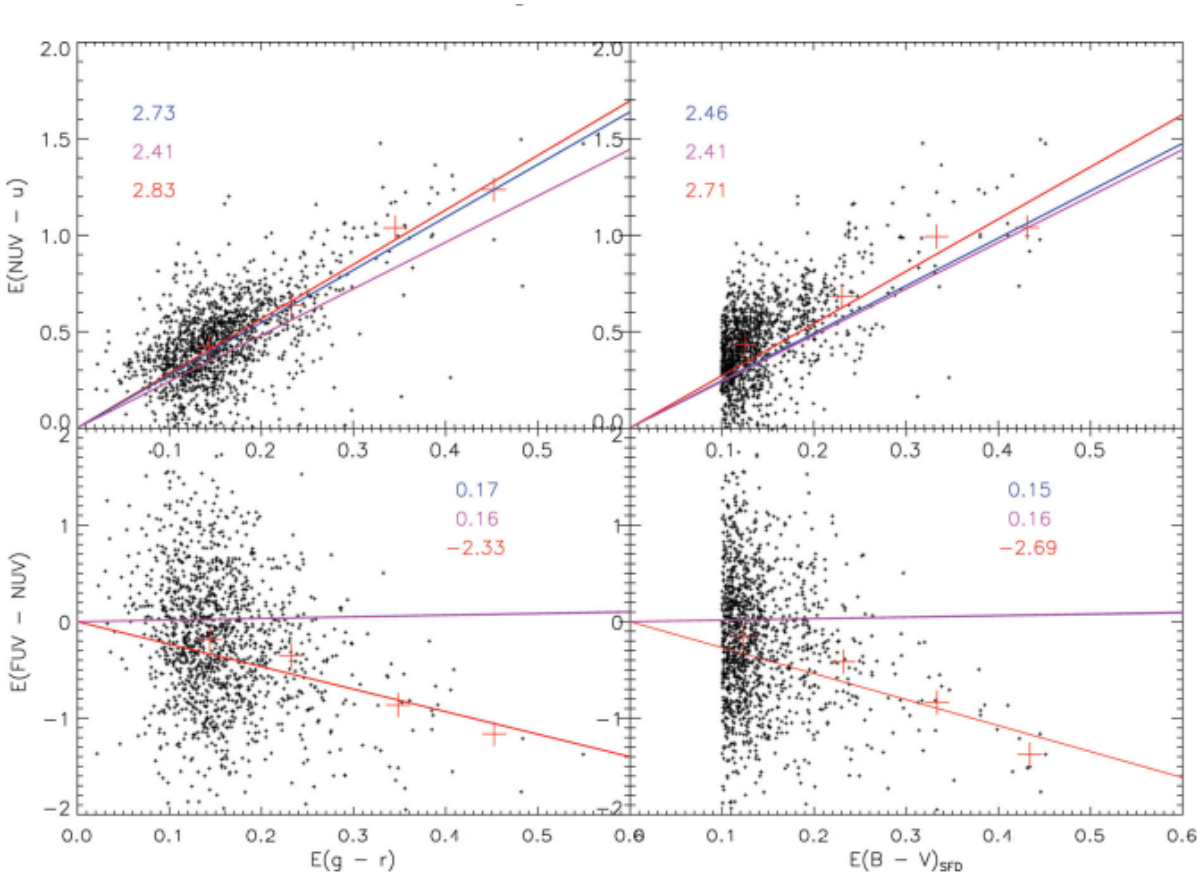


**Figure 1.3:** Figure 4 from Yuan, Liu, & Xiang (2013). Reddening coefficients of the $NUV - u$ and $FUV - NUV$ colours. (Left panels) Reddening of the $NUV - u$ (top panel) and $FUV - NUV$ (bottom panel) colours versus that of $g - r$. (Right panels) Reddening of the $NUV - u$ (top panel) and $FUV - NUV$ (bottom panel) colours versus $E(B - V)$ from Schlegel, Finkbeiner, & Davis (1998). Red pluses represent median values by binning the data points into eight groups with a bin size of 0.1 on the $x$-axis. The red lines are linear fits to the binned data. Relations predicted by the Fitzpatrick (1999), Cardelli, Clayton, & Mathis (1989), and O'Donnell (1994) reddening laws for $R(V) = 3.1$ are plotted in purple, blue, and cyan, respectively

# CHAPTER 2

# GALEX Absolute Calibration and Extinction Coefficients Based on White Dwarfs

## 2.1. Introduction

The Galaxy Evolution Explorer (GALEX) is the first space based mission to attempt an all-sky imaging survey in the ultraviolet (UV, Martin et al., 2005). In the ten years that it was operational, GALEX surveyed 26,000 square degrees of the sky as part of the All-sky Imaging Survey in two band passes: Far Ultraviolet (FUV) with a central wavelength of 1528 Å and Near Ultraviolet (NUV) with a central wavelength of 2271 Å (Morrissey et al., 2005). Although its primary goal was to study star formation and galaxy evolution, the first science goal was to determine UV calibration, particularly extinction (Martin et al., 2005).

There are two sources of nonlinearity in GALEX photometry: global nonlinearity due to the finite period required for the electronics to assemble photon lists and local nonlinearity near bright sources. Morrissey et al. (2005)(see their Fig. 8) demonstrate that nonlinearity becomes significant ($> 10\%$) above 109 and 311 counts $s^{-1}$ in the FUV and NUV bands, respectively. These correspond to $m_{\rm FUV} \approx 14$ mag and $m_{\rm NUV} \approx 15$ mag. While the first nonlinearity is well understood, the second (local nonlinearity) complicates the standard star measurements.

For photometric calibration GALEX observed 18 white dwarfs from the *Hubble Space Telescope* CALSPEC database (Bohlin, Dickinson, & Calzetti, 2001) as standard stars. However, since all of the other standard stars observed are highly saturated, its photometric calibration relies primarily on the dimmest star in this sample, LDS 749b. After Bohlin & Koester (2008) provided a better CALSPEC spectrum for LDS 749b, the GALEX magnitudes were shifted by ≈0.04 mag between the GR4/5 and GR6 data releases. Hence, it is important to verify the photometric calibration using fainter stars.

Camarota & Holberg (2014) verified the GALEX photometric calibration using 99 and 107 DA white dwarfs in the FUV and NUV, respectively, with magnitudes between 10 and 17.5 from the final GR7 GALEX data release. They found that a modest linearity correction is needed in this magnitude range. Although Camarota & Holberg (2014) postulate that their linearity correction should hold for stars as faint as 20th magnitude, they point out the need for a larger sample size and the characterization of extinction in the GALEX bands. In this work, we investigate the validity of the Camarota & Holberg (2014) linearity correction for a large sample of DA white dwarfs from the

Sloan Digital Sky Survey (SDSS), particularly probing the fainter magnitudes.

There is a broad range of GALEX extinction coefficients reported in the literature. These coefficients are defined in equation 1.2. Most of the GALEX extinction coefficients in the literature are theoretical. Bianchi (2011) provided theoretical estimates of $R_{\rm FUV} = 8.06$ and $R_{\rm NUV} = 7.95$ for Milky Way type dust and $R_{\rm FUV} = 12.68$. Yuan, Liu, & Xiang (2013) found empirical values of $R_{\rm FUV} = 4.37 - 4.89$ and $R_{\rm NUV} = 7.06 - 7.24$. They used the 'standard pair' technique (Stecher, 1965) described in section 1.6. Yuan, Liu, & Xiang (2013) examined a target sample of 1396 stars and a control sample of 16405 stars from the GALEX fifth data release. Most of these stars were classified as FG dwarfs. There is a great deal of scatter and uncertainty in their derivation of the GALEX extinction coefficients, and Yuan, Liu, & Xiang (2013) caution against using their GALEX extinction coefficients. In this work, we re-derive the GALEX extinction coefficients using a large sample of DA white dwarf stars with high S/N SDSS spectra and Gaia parallaxes to obtain a more reliable estimate.

We present the white dwarf sample used in this study in Section 2.2 and describe our calculation of the synthetic magnitudes in Section 2.3. Our analysis of nonlinearity is presented in Section 2.4 followed by our derivation of the GALEX extinction coefficients in Section 2.5. The $3\sigma$ outliers are discussed in Section 2.6, and we conclude in Section 2.7.

### 2.2. Sample Selection

In order to improve calibrations for the GALEX data, we select all spectroscopically confirmed DA white dwarfs from the SDSS data releases 7, 10, and 12 with S/N $\geq 20$ spectra (Kleinman et al., 2013; Kepler et al., 2015, 2016). This selection insures that the $T_{\rm eff}$ and $\log g$ measurements are precise enough to model the emergent stellar fluxes in the UV bands. We focus on DA white dwarfs due to our good understanding of their opacities and atmospheres (Holberg & Bergeron, 2006). We cross reference our initial sample of 3733 DA white dwarfs from the SDSS with Pan-STARRS, and we cross reference our sample once more with *Gaia DR*2, selecting all stars with parallax/error $\geq 5$. We then cross reference our sample with the GALEX catalog of unique UV sources from the All Sky Imaging Survey (GUVcat) presented in Bianchi et al. (2017). We use a search radius of $2''$ and find a total of 1837 stars with GALEX photometry.

We break our initial sample of stars into two groups based on *Gaia* distance: stars within 100 pc and stars further than 250 pc. There are 339 (627) and 451 (628) stars with FUV and NUV photometry in the 100 ($d > 250$) pc sample, respectively. We leave the examination of stars between 100 and 250 pc for future work (see chapter 4). The local interstellar medium is relatively devoid of cold neutral gas, up to about 100 pc, the boundary of the Local Bubble (Lallement et al., 2003; Redfield, 2006). Since extinction is not an issue for the 100 pc sample, we use it to verify the GALEX photometric calibration. The $d > 250$ pc sample suffers from full extinction, and we use it

to calculate the extinction coefficients in both the FUV and NUV bands.

### 2.3. Synthetic Magnitudes

Genest-Beaulieu & Bergeron (2019) found a systematic offset between temperatures derived using the spectroscopic (Bergeron, Saffer, & Liebert, 1992) and photometric (Bergeron, Ruiz, & Leggett, 1997) techniques. They determine that this offset is caused by inaccuracies in the treatment of Stark broadening in their model spectra. The photometric technique is less sensitive to the input physics of the models, so we adopted it for this work. We use SDSS *u* and Pan-STARRS *grizy* photometry and *Gaia* parallaxes to derive photometric temperatures and radii for all stars in our final sample. These temperature and radius measurements are then used to calculate a model spectrum for each white dwarf in the 100 pc sample.

To estimate the average flux in a given bandpass, $f_\lambda^m$, we use the equation

$$f_\lambda^m = \frac{\int_0^\infty f_\lambda S_m(\lambda)\lambda \mathrm{d}\lambda}{\int_0^\infty S_m(\lambda)\lambda \mathrm{d}\lambda}, \tag{2.1}$$

where $S_m(\lambda)$ is the transmission function of the corresponding bandpass, and $f_\lambda$ is the monochromatic flux from the star received at Earth (Bergeron, Ruiz, & Leggett, 1997; Gianninas et al., 2011). SDSS, Pan-STARRS, and GALEX use the AB magnitude system. We transform the average flux in a given bandpass to an average magnitude using the equation

$$m = -2.5 \log f_\nu^m - 48.6. \tag{2.2}$$

This procedure enables us to calculate the absolute magnitude of each star in each filter. We use the observed and dereddened SDSS magnitudes for the $d < 100$ and $d > 250$ pc samples, respectively. The full 100 and 250 pc samples can be found in this chapter's appendix.

### 2.4. GALEX Photometric Calibration

Our 100 pc SDSS sample contains few stars brighter than 14th magnitude. In order to constrain the fit for both faint and bright white dwarfs, we extend our sample to include the 100 pc white dwarfs from Camarota & Holberg (2014) and Gianninas et al. (2011). Figure 2.1 compares the observed and predicted synthetic magnitudes for this sample in both bands. The solid and dashed lines show a quadratic polynomial fit to the data and the 1:1 line, respectively. Stars with $T_{\rm eff}$ below 11,000 K are represented by yellow triangles. Stars below this temperature suffer from the red wing of the Ly$\alpha$ opacity, which affects the ultraviolet more strongly than the optical (Kowalski & Saumon, 2006). The $3\sigma$ outliers that are known double degenerates, white dwarf + main sequence binaries, and ZZ Cetis are marked by cyan triangles, green diamonds, and magenta pentagons, respectively. Previously unknown $3\sigma$ outliers in our polynomial fit are plotted as red squares. All $3\sigma$ outliers are

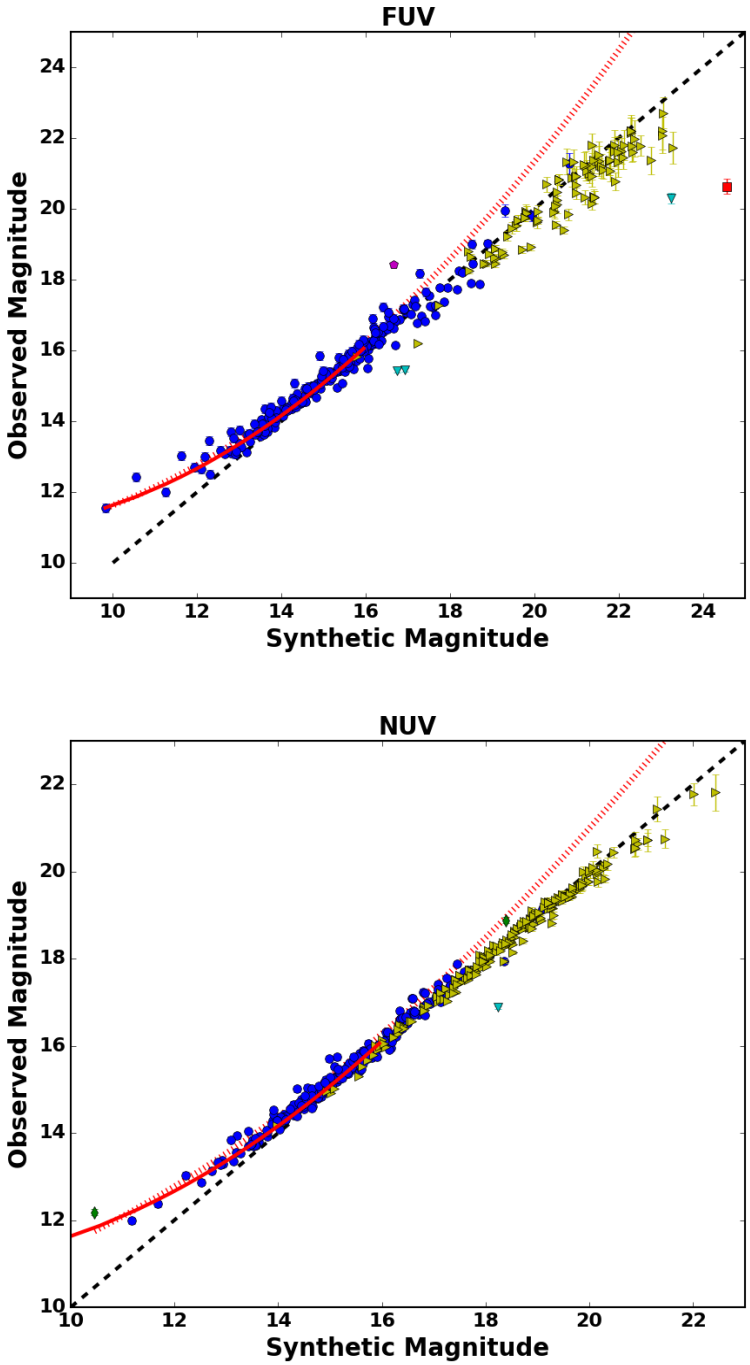


**Figure 2.1:** The linearity fit for stars within 100 pc in the FUV band (top) and the NUV band (bottom). The quadratic linearity fit from Camarota & Holberg (2014) is marked as the red dashed line. Our linearity fit is plotted in solid red. The black dashed line is the 1:1 correlation. Stars with $T_{\rm eff}$ below 11,000 K are plotted as yellow triangles. Cyan triangles are known double degenerate systems and green diamonds are previously known white dwarf + main sequence binaries. The magenta pentagon marks the ZZ Ceti WD1258+013. Previously unknown $3\sigma$ outliers are plotted as red squares.

Table 2.1. Fitting parameters for the linearity correction in the FUV and NUV bands (see Eq 2.3.)

| Property | FUV | NUV |
|---|---|---|
| $c_0$ | 13.23 | 10.49 |
| $c_1$ | -0.727 | -0.31 |
| $c_2$ | 0.057 | 0.041 |
| Range | $\leq$ 15.95 mag | $\leq$ 16.95 mag |

excluded from this fit. We further discuss these outliers in Section 2.6.

Our quadratic fits are represented by the expression

$$m_{\rm obs} = c_2 m_{\rm synth}^2 + c_1 m_{\rm synth} + c_0, \tag{2.3}$$

where $m_{\rm obs}$ and $m_{\rm synth}$ are the observed and synthetic GALEX magnitudes, respectively. The best fit values of the fitting coefficients $c_0$, $c_1$, and $c_2$ are given in Table 2.1.

Camarota & Holberg (2014) found a non-linear correlation and small offset between GALEX fluxes and predicted fluxes for their sample. Their quadratic fit is shown as a dotted line in Figure 2.1 and is based on about 100 DA white dwarfs with FUV and NUV magnitudes between 10 and 17.5 mag. However, they only have 6-8 stars fainter than 17th magnitude in their sample, hence the fit is relatively unconstrained at the faint end. The dotted line significantly underpredicts the observed magnitudes in both FUV and NUV bands, and is clearly not useful below 17th magnitude.

With a significantly larger number of fainter DA white dwarfs, we are able to test for non-linearities in the data down to magnitudes fainter than 20. We note that stars with $T_{\rm eff}$ below 11,000 K have systematically fainter synthetic magnitudes in the FUV, while there is no systematic offset in the NUV. Since these stars are affected by the red wing of the Ly$\alpha$ opacity (Kowalski & Saumon, 2006), our results indicate that this opacity source is well handled in our models for the NUV, while the modeling of this opacity should be revisited for the FUV. To remove this systematic effect from our fit, we first fit the full sample to calculate the magnitude where the full quadratic fit crosses the 1:1 line for the FUV and NUV. Only stars brighter than these magnitudes, 15.95 mag (FUV) and 16.95 mag (NUV), will require a linearity correction. To determine the linearity correction, we then fit only stars brighter than 15.95 mag (FUV) and 16.95 mag (NUV). This is our final quadratic fit which is plotted in Figure 2.1. Our linearity corrections are not statistically different from those presented in Camarota & Holberg (2014). To convert the observed GALEX magnitudes into corrected magnitudes, we find the quadratic solutions to the linearity corrections shown in Figure 2.1. Our final corrections take the form

Table 2.2. Inverse quadratic corrections for the FUV and NUV bands (see Eq 2.4.)

| Property | FUV | NUV |
|---|---|---|
| $c_0$ | 6.412 | 3.778 |
| $c_1$ | 17.63 | 24.337 |
| $c_2$ | -192.135 | -241.018 |

$$m_{\rm corr} = c_0 + (c_1 m_{\rm obs} + c_2)^{1/2}, \tag{2.4}$$

where $m_{\rm obs}$ and $m_{\rm corr}$ are the observed and corrected GALEX magnitudes, respectively. The calculated constants $c_0$, $c_1$, and $c_2$ are given in Table 2.2. These corrections are applicable to objects brighter than 15.95 mag and 16.95 mag in the FUV and NUV, respectively.

### 2.5. Extinction Coefficients

After revisiting the linearity corrections and determining the magnitudes they are valid over, we examine the sample of SDSS DA white dwarfs with *Gaia* distances beyond 250 pc. We apply the linearity corrections given in Table 2.2 only to those stars brighter than our cut-off magnitudes. Figure 2.2 shows the observed versus synthetic magnitudes for the 250 pc white dwarf sample. These stars experience full extinction, which leads to observed FUV and NUV photometry fainter than expected.

We calculate the $R$ value in the NUV and FUV bands for each star using Equation 1.2, the total absorption in each filter $A_\lambda$ (the difference between the synthetic and observed magnitude), and $E(B-V)$ from Schlafly & Finkbeiner (2011). We find 9 stars in the FUV and 18 stars in the NUV with negative $R$ values. These stars, as well as the $4\sigma$ outliers, are excluded from the weighted average of the $R$ vaules.

Figure 2.3 shows the distribution of the R values in the FUV and NUV filters. Since the R values for some stars have relatively large uncertainties, here we plot weighted histograms, where each R value only contributes its associated error towards the bin count (instead of 1). This figure reveals a relatively large spread in R for both filters, with a standard deviation $\sim 3$. This spread in R values indicates that we cannot characterize the interstellar extinction by a universal reddening law for all lines of sight within the SDSS footprint. However, our best estimate, the weighted mean values, are $R_{\rm FUV} = 8.01 \pm 0.07$ and $R_{\rm NUV} = 6.79 \pm 0.04$.

Bianchi (2011) estimated GALEX extinction coefficients using progressively reddened models for stars with $T_{\rm eff} = 15,000 - 30,000$ K. Since GALEX NUV band includes the strong broad

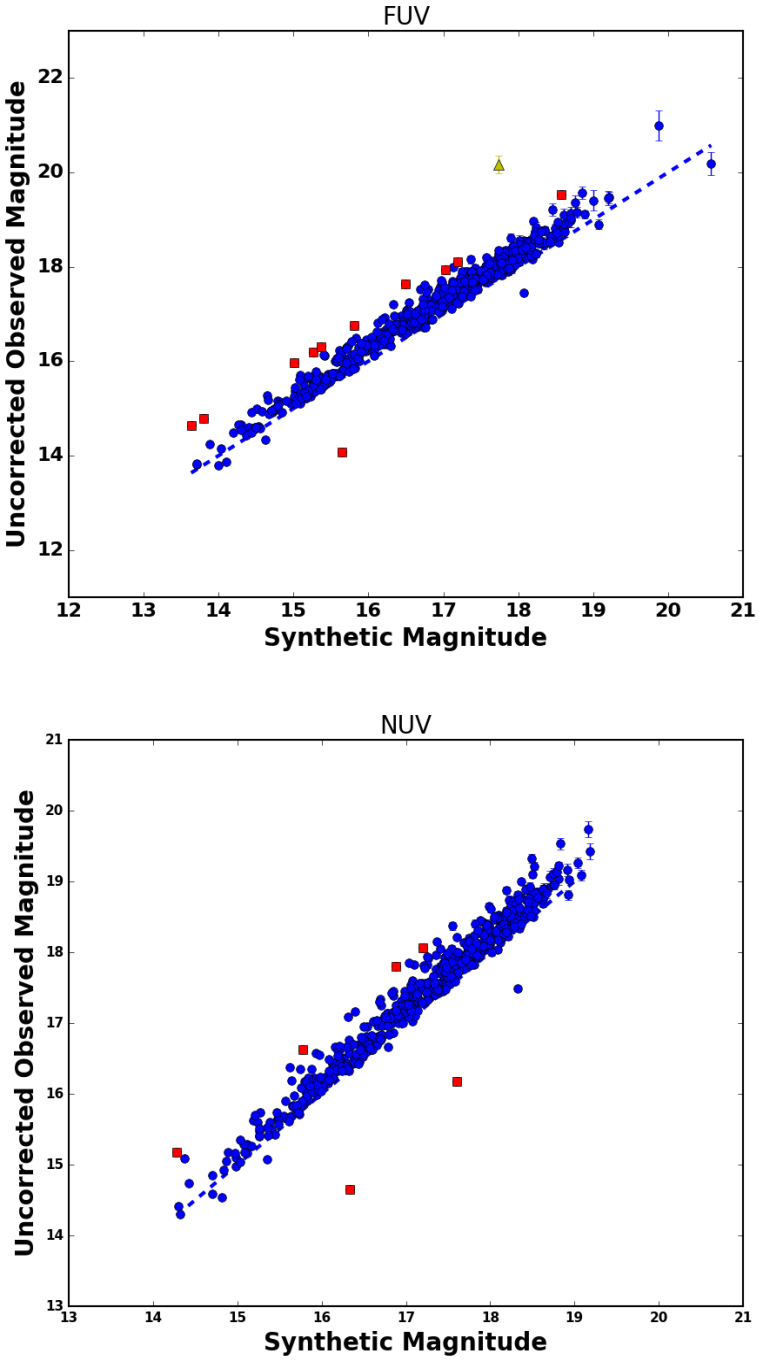


**Figure 2.2:** Uncorrected versus model magnitudes for stars beyond 250 pc in the FUV and NUV bands. The blue dashed line is the 1:1 correlation and $4\sigma$ outliers are plotted as red squares. The candidate double degenerate J211607.27+004503.17 is plotted as a yellow triangle.

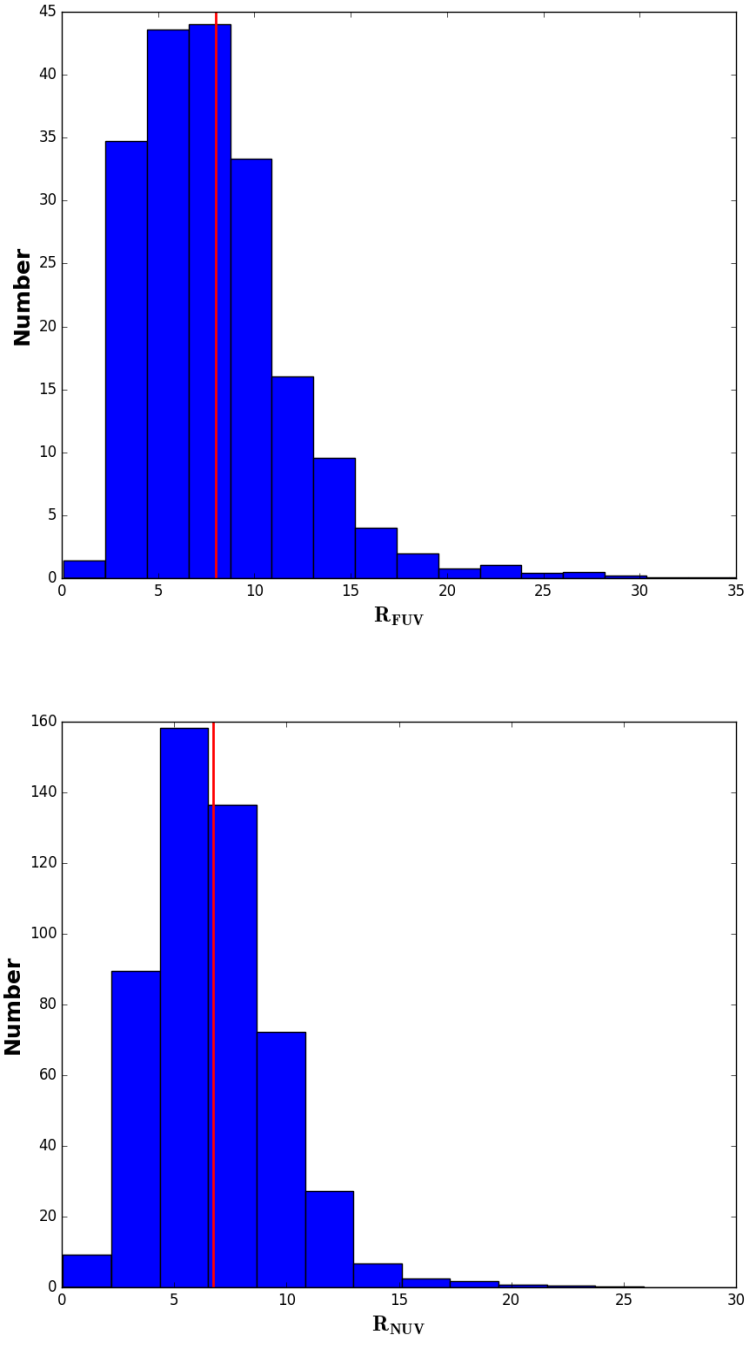


**Figure 2.3:** Histograms of weighted *R* values for FUV and NUV bands. The solid red line is the weighted average.

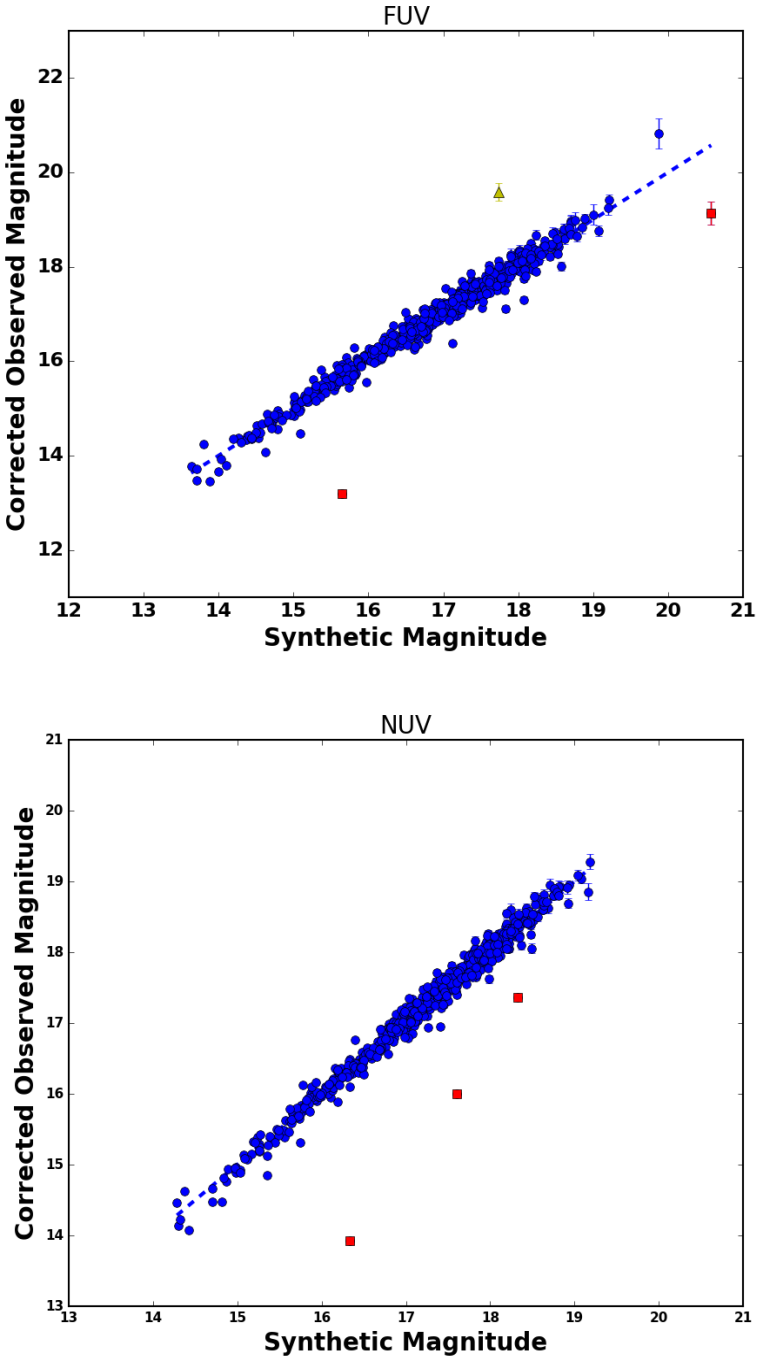


**Figure 2.4:** Extinction corrected versus model magnitudes for stars beyond 250 pc in the FUV and NUV bands. The blue dashed line is the 1:1 correlation and $4\sigma$ outliers are plotted as red squares. The candidate double degenerate J211607.27+004503.17 is plotted as a yellow triangle.

absorption feature at 2175 Å, they predict an overall absorption that is similar in both the FUV and NUV bands. For Milky Way type dust, they predict $R_{\rm FUV} \approx R_{\rm NUV} \approx 8.0$. However, for UV-steep extinction curves like those of the Large Magellanic Cloud (LMC) and the SMC, the increase in absorption is larger in the FUV and the 2175 Å bump is less pronounced, resulting in estimates of $R_{\rm FUV} = 8.6 - 12.7$ and $R_{\rm NUV} = 7.0 - 8.1$. Hence, some of the scatter seen in Figure 2.3 can be explained by the differences in extinction curves along different line of sights as sampled by our targets.

Empirical constraints on GALEX extinction by Yuan, Liu, & Xiang (2013) agree relatively well in the NUV but they differ significantly in the FUV. Yuan, Liu, & Xiang (2013) measure $R_{\rm NUV} = 7.24 \pm 0.08$ or $7.06 \pm 0.22$ and $R_{\rm FUV} = 4.89 \pm 0.60$ or $4.37 \pm 0.54$. Our FUV extinction coefficient is significantly larger than the Yuan, Liu, & Xiang (2013) estimate and in good agreement with the Bianchi (2011) estimate. Given the simplicity of DA white dwarf photospheres, white dwarfs are excellent spectrophotometric standard stars and our empirical results are significantly more precise than previous FUV and NUV extinction coefficient measurements.

Figure 2.4 shows a comparison between the observed FUV/NUV magnitudes corrected for non-linearity and extinction and the synthetic magnitudes for the $d > 250$ pc sample using our best-estimates of $R_{\rm FUV} = 8.01 \pm 0.07$ and $R_{\rm NUV} = 6.79 \pm 0.04$. These R values provide excellent corrections for our dataset, as the majority of the objects fall on or near the 1:1 line (shown as a blue dashed line). The red squares mark the $4\sigma$ outliers from the 1:1 line. The yellow triangle marks J211607.27+004503.17, a previously known candidate binary system (Baxter et al., 2014). We further discuss the unknown outliers in Section 2.6.

### 2.6. Outliers

Here we revisit the 3 and $4\sigma$ outliers identified in the 100 and 250 pc samples in Sections 2.4 and 2.5, respectively. One possible cause of a significant difference between the observed and model FUV and NUV magnitudes is the presence of an unseen companion. If two stars are sufficiently close together to be unresolved in both GALEX and the SDSS observations, one could still identify the binary nature of the system through UV-excess, like the double white dwarf SDSS J125733.63+542850.5 (Badenes et al., 2009; Kulkarni & van Kerkwijk, 2010; Marsh et al., 2011; Bours et al., 2015). Note that this method only works for systems where there is a significant temperature difference between the two white dwarfs.

Out of our twelve total outliers, seven are previously known systems. Although WD0901+140 is a visual binary (Farihi, Becklin, & Zuckerman, 2005), it was not resolved in GALEX. Of the five remaining outliers, the photometry of WD0846+335 is likely contaminated by a nearby background galaxy. In Figure 3.5.2, we plot the SEDs of the remaining four outliers. We plotted the SDSS and GUVcat fluxes as blue errorbars. Each of these objects has UV observations from other GALEX

Table 2.3. Previously known binary or variable white dwarfs that are identifed as outliers in this work.

| Object | Type | Reference |
|---|---|---|
| WD0037−006 | Double-lined double degenerate | Koester et al. (2009) |
| WD0232+035 | DA+dM | Kawka et al. (2008) |
| WD0901+140 | Visual double degenerate | Farihi, Becklin, & Zuckerman (2005) |
| WD1019+462 | WD+dM | Reid (1996) |
| WD1022+050 | Double degenerate | Bragaglia, Renzini, & Bergeron (1995) |
| WD1258+013 | ZZ Ceti | Bergeron et al. (2004) |
| J211607.27+004503.17 | Double degenerate candidate | Baxter et al. (2014) |

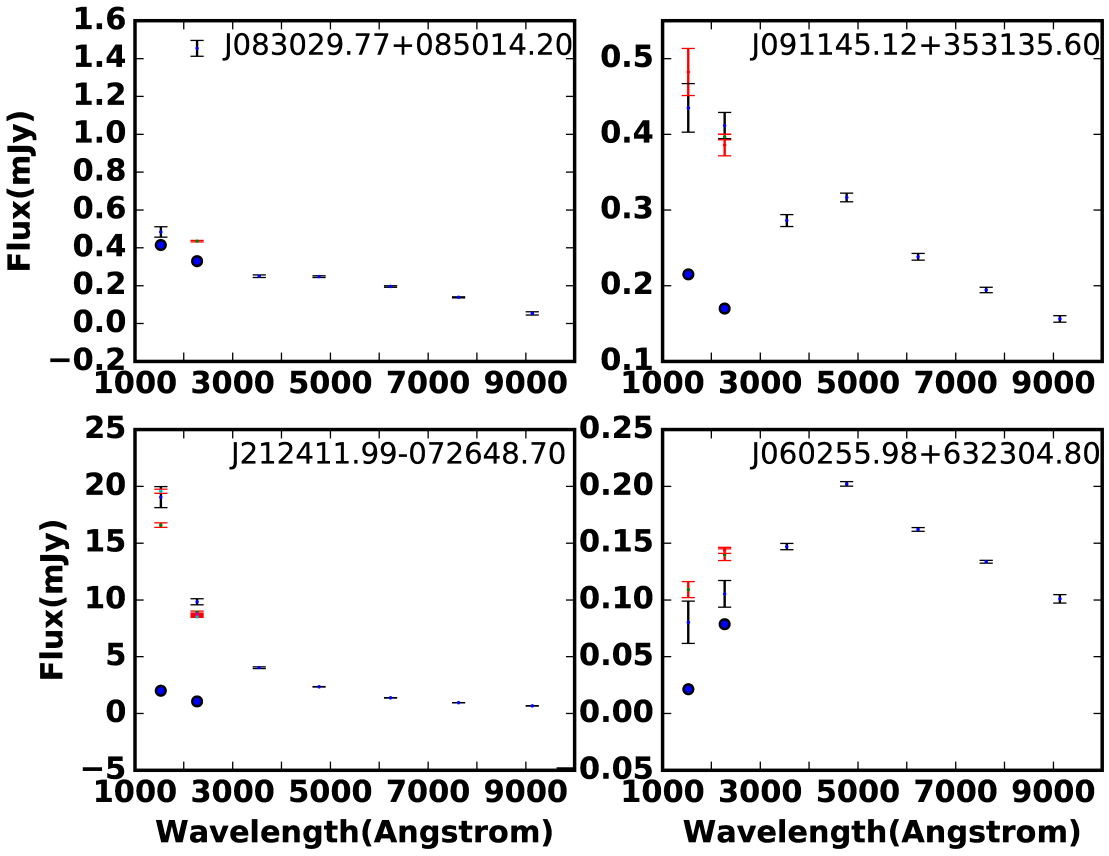


**Figure 2.5:** SEDs of four newly identified candidate UV-excess white dwarfs. Black errorbars represent fluxes from SDSS and GUVcat. Red errorbars represent fluxes from all other GALEX observations. Blue dots represent model fluxes. Note that two of these outliers, J0830+0850 and J2124−0726, likely have contaminated photometry or inaccurate photometric solutions.

surveys. These fluxes are represented by the red errorbars. Model fluxes are represented by blue dots. J083029.77+085014.20 is sufficiently near to a bright star that its photometry was contaminated in the shallow AIS survey. Deeper surveys removed this contamination, as can be seen in Figure 3.5.2. J212411.99−072648.70 has a spectroscopic $T_{\rm eff}$ of 76,364 K from Kleinman et al. (2013), well above 35,000 K, the $T_{\rm eff}$ above which the photometric technique becomes less reliable (Genest-Beaulieu & Bergeron, 2019). It is likely that the photometric $T_{\rm eff}$ is off, leading to the apparent UV excess. J060255.98+632304.80 has a $T_{\rm eff}$ of 11,078 K and a $\log g$ of 7.7, placing this star within the ZZ Ceti instability strip (10,500−13,000K $T_{\rm eff}$). The UV excess is greater in other GALEX surveys. ZZ Ceti pulsations are stronger in the UV, so the UV excess could be due to pulsations as with WD1258+013. Further observations are needed to confirm that J060255.98+632304.80 is a ZZ Ceti. There are no obvious explanations for the UV excess of J091145.12+353135.60. Follow-up UV spectroscopy or radial velocity observations would be helpful in understanding the nature of this object.

### 2.7. Conclusions

We examine a sample of 1837 DA white dwarfs that were observed by both SDSS and GALEX. By combining our SDSS sample within 100 pc and the bright white dwarf samples form Camarota & Holberg (2014) and Gianninas et al. (2011), we determine an improved linearity correction to the GALEX data. We determine that our linearity corrections are only necessary for objects brighter than 15.95 mag and 16.95 mag for the FUV and NUV bands, respectively. We present new extinction coefficients for the GALEX bands: $R_{\rm FUV} = 8.01 \pm 0.07$ and $R_{\rm NUV} = 6.79 \pm 0.04$. These white dwarfs currently provide the best constraints on the linearity corrections and extinction coefficients for GALEX data.

Here we present one application of our newly derived *R* values for identifying unusual white dwarfs. We identify seven previously known objects: three double degenerates (WD0037−006, WD0901+140, and WD1022+050), two white dwarf+main sequence binaries (WD1019+462 and WD0232+035), one ZZ Ceti (WD1258+013), and one double degenerate candidate (J211607.27+004503.17) as outliers. We find one previously unknown $3\sigma$ outlier and four previously unknown $4\sigma$ outliers. The UV-excesses of three of these objects (WD0846+335, J083029.77+085017.20, and J212411.99−072648.70) can be explained by contaminating background sources or inaccurate photometric solutions. Two outliers, J091145.12+353135.60 and J060255.98+632304.80, require follow-up spectroscopy to verify their natures. In the future, we will use our linearity corrections and our newly derived extinction coefficients to study the remainder of our SDSS sample and identify unusual objects.

## 2.8. Acknowledgements

This work is supported by the NASA Astrophysical Data Analysis Program grant NNX14AF65G. This work is supported in part by the NSERC Canada and by the Fund FRQ-NT (Québec). This work has made use of data from the European Space Agency (ESA) mission *Gaia* (https://www.cosmos.esa.int/gaia), processed by the *Gaia* Data Processing and Analysis Consortium (DPAC, https://www.cosmos.esa.int/web/gaia/dpac/consortium). Funding for the DPAC has been provided by national institutions, in particular the institutions participating in the *Gaia* Multilateral Agreement. We thank our referee, Jay Holberg, for his useful suggestions.

# Appendix

## 2.A. 100 pc Sample

Table begins on the next page.

Table 2.A.1. Properties of stars within 100 pc in our sample. Stars with WD names are from Gianninas et al. (2011).

| Star | Synthetic FUV mag | Synthetic NUV mag | Observed FUV mag | Observed NUV mag |
|---|---|---|---|---|
| J000410.42−034008.60 | 25.802 | 19.201 | ... | 19.142 ± 0.070 |
| J001339.11+001924.90 | 19.769 | 16.403 | 19.756 ± 0.103 | 16.449 ± 0.014 |
| J001339.20+001924.30 | 19.769 | 16.403 | 19.756 ± 0.103 | 16.449 ± 0.014 |
| J002049.39+004435.10 | 22.29 | 17.96 | 22.194 ± 0.369 | 17.937 ± 0.027 |
| J002049.55+004433.94 | 22.29 | 17.96 | 22.194 ± 0.369 | 17.937 ± 0.027 |
| WD0023−109 | 20.714 | 17.385 | 19.394 ± 0.093 | 17.203 ± 0.019 |
| J002634.39+353337.60 | 23.59 | 19.187 | ... | 19.132 ± 0.072 |
| J003328.03+054039.18 | 26.94 | 20.354 | ... | 20.167 ± 0.142 |
| J003511.63+001150.40 | 20.592 | 17.417 | 20.817 ± 0.151 | 17.511 ± 0.022 |
| WD0033+016 | 18.921 | 16.312 | 18.727 ± 0.077 | 16.368 ± 0.016 |
| WD0037−006 | 16.92 | 15.548 | 15.456 ± 0.016 | 15.299 ± 0.010 |
| J004511.19+090445.37 | 25.926 | 19.923 | ... | 19.922 ± 0.128 |
| WD0048+202 | 14.519 | 14.839 | 14.565 ± 0.008 | 14.837 ± 0.005 |
| J005438.84−095219.70 | 22.299 | 18.077 | 22.158 ± 0.497 | 17.942 ± 0.043 |
| WD0058−044 | 14.933 | 15.139 | 14.934 ± 0.016 | 15.182 ± 0.011 |
| WD0100−036 | 22.062 | 17.91 | 21.635 ± 0.369 | 17.885 ± 0.039 |
| WD0101+059 | 16.318 | 16.138 | 16.219 ± 0.021 | 16.132 ± 0.012 |
| WD0101+048 | 20.513 | 15.622 | 19.545 ± 0.103 | 15.528 ± 0.011 |
| WD0102+095 | 13.163 | 13.626 | 13.130 ± 0.007 | 13.801 ± 0.006 |
| J010543.14−092054.60 | 24.111 | 18.849 | ... | 18.729 ± 0.046 |
| WD0104+015 | 23.286 | 18.723 | 21.735 ± 0.448 | 18.408 ± 0.063 |
| WD0107+267 | 15.156 | 15.181 | 15.144 ± 0.008 | 15.231 ± 0.005 |
| J011055.07+143922.30 | 21.774 | 17.99 | 21.338 ± 0.387 | 18.041 ± 0.033 |
| J011055.16+143921.70 | 21.774 | 17.99 | 21.338 ± 0.387 | 18.041 ± 0.033 |
| J011104.31+220429.75 | 23.03 | 18.747 | ... | 18.853 ± 0.070 |
| WD0126+101 | 20.094 | 15.831 | 19.666 ± 0.087 | 15.789 ± 0.007 |
| WD0126+422 | 13.673 | 14.124 | 13.788 ± 0.009 | 14.278 ± 0.008 |
| WD0129−205 | 14.441 | 14.772 | 14.488 ± 0.011 | 14.799 ± 0.007 |
| WD0135−052 | 21.535 | 15.075 | 21.523 ± 0.374 | 15.013 ± 0.010 |
| J014342.45+131013.60 | 24.421 | 19.252 | ... | 19.302 ± 0.093 |
| WD0142+312 | 19.931 | 16.073 | 18.921 ± 0.085 | 15.977 ± 0.014 |
| WD0143+216 | 20.092 | 16.218 | 19.933 ± 0.155 | 16.200 ± 0.015 |
| WD0145+234 | 14.826 | 14.358 | 14.663 ± 0.014 | 14.383 ± 0.008 |
| J015259.19+010018.50 | 18.711 | 17.122 | 17.879 ± 0.030 | 17.017 ± 0.014 |
| WD0151+017 | 15.793 | 15.327 | 15.920 ± 0.017 | 15.390 ± 0.009 |
| WD0155+069 | 14.041 | 14.474 | 14.141 ± 0.017 | 14.648 ± 0.009 |

Table 2.A.1 (cont'd)

| Star | Synthetic FUV mag | Synthetic NUV mag | Observed FUV mag | Observed NUV mag |
|---|---|---|---|---|
| WD0220+222 | 15.467 | 15.608 | 15.682 ± 0.019 | 15.468 ± 0.010 |
| WD0231−054 | 15.437 | 14.645 | 15.085 ± 0.015 | 14.568 ± 0.008 |
| WD0235+064 | 15.885 | 15.713 | 15.996 ± 0.018 | 15.767 ± 0.011 |
| WD0242−174 | 14.478 | 14.828 | 14.514 ± 0.015 | 14.918 ± 0.010 |
| J030335.09+000221.90 | 23.714 | 19.203 | ... | 19.289 ± 0.041 |
| J030632.08−063854.40 | 25.438 | 19.678 | ... | 19.626 ± 0.066 |
| WD0308+188 | 13.526 | 13.794 | 14.041 ± 0.012 | 14.031 ± 0.007 |
| J031813.26−010711.70 | 15.066 | 15.003 | 15.149 ± 0.011 | 15.014 ± 0.006 |
| J032755.79−063605.80 | 25.644 | 19.523 | ... | 19.416 ± 0.098 |
| J040457.98−052324.20 | 22.967 | 18.793 | ... | 18.853 ± 0.053 |
| J041458.25+064008.20 | 16.699 | 15.801 | 16.162 ± 0.023 | 15.718 ± 0.011 |
| J053345.36+605750.10 | 17.412 | 16.278 | 16.824 ± 0.028 | 16.215 ± 0.013 |
| WD0706+294 | 15.501 | 15.533 | 15.615 ± 0.016 | 15.548 ± 0.010 |
| J073237.88+420454.30 | 16.064 | 16.242 | 16.028 ± 0.020 | 16.185 ± 0.010 |
| J073708.00+411227.50 | 17.938 | 16.412 | 17.762 ± 0.050 | 16.457 ± 0.011 |
| J074640.29+355748.10 | 27.783 | 20.932 | ... | 20.639 ± 0.134 |
| J075026.29+174029.80 | 26.348 | 19.684 | ... | 19.601 ± 0.079 |
| J075443.28+161425.20 | 24.803 | 19.4 | ... | 19.403 ± 0.080 |
| J075929.74+473509.50 | 21.551 | 17.459 | 21.221 ± 0.210 | 17.419 ± 0.010 |
| J080347.31+082914.20 | 20.548 | 18.017 | 20.246 ± 0.125 | 17.999 ± 0.031 |
| J080418.83+353859.30 | 22.542 | 18.552 | ... | 18.495 ± 0.034 |
| J080429.35+421312.70 | 21.561 | 17.961 | ... | 17.939 ± 0.033 |
| J080951.09+225054.10 | 27.755 | 20.87 | ... | 20.516 ± 0.179 |
| WD0808+423 | 17.746 | 17.652 | 17.768 ± 0.046 | 17.738 ± 0.031 |
| WD0810+234 | 15.781 | 15.927 | 15.860 ± 0.030 | 15.946 ± 0.017 |
| WD0816+297 | 15.318 | 15.532 | 15.392 ± 0.014 | 15.603 ± 0.008 |
| J082001.31+383435.00 | 24.484 | 18.481 | ... | 18.379 ± 0.059 |
| J082036.99+431005.20 | 26.769 | 19.976 | ... | 19.776 ± 0.084 |
| J082733.10+260703.10 | 26.577 | 20.302 | ... | 20.128 ± 0.102 |
| WD0826+455 | 18.455 | 15.961 | 18.237 ± 0.055 | 15.988 ± 0.009 |
| WD0826+418 | 20.998 | 18.077 | 20.930 ± 0.264 | 18.092 ± 0.043 |
| J083124.87+164158.60 | 26.305 | 19.655 | ... | 19.422 ± 0.041 |
| J083132.75+132243.90 | 15.792 | 15.928 | 15.957 ± 0.020 | 16.016 ± 0.013 |
| J083723.49+510058.40 | 25.646 | 19.474 | ... | 19.461 ± 0.095 |
| WD0836+404 | 17.173 | 16.115 | 17.254 ± 0.048 | 16.219 ± 0.020 |
| J084252.28+342422.30 | 16.057 | 16.168 | 15.785 ± 0.027 | 15.941 ± 0.019 |

Table 2.A.1 (cont'd)

| Star | Synthetic FUV mag | Synthetic NUV mag | Observed FUV mag | Observed NUV mag |
|---|---|---|---|---|
| WD0839+231 | 12.908 | 13.416 | 13.141 ± 0.007 | 13.698 ± 0.005 |
| J084457.81+453632.80 | 21.363 | 17.301 | 20.153 ± 0.178 | 17.176 ± 0.027 |
| WD0842+382 | 23.068 | 17.709 | 22.705 ± 0.439 | 17.619 ± 0.029 |
| J084909.45+342947.70 | 23.726 | 17.66 | ... | 17.522 ± 0.030 |
| J084948.62+331925.10 | 24.561 | 18.516 | 20.631 ± 0.211 | 18.142 ± 0.039 |
| J084949.62+092353.40 | 22.815 | 18.896 | ... | 19.104 ± 0.081 |
| J085458.63+275225.60 | 26.885 | 20.145 | ... | 20.469 ± 0.159 |
| WD0854+404 | 13.594 | 14.025 | 13.693 ± 0.009 | 14.118 ± 0.005 |
| J085749.63+180802.50 | 27.091 | 20.164 | ... | 19.775 ± 0.128 |
| J085757.63+254207.62 | 29.396 | 22.437 | ... | 21.820 ± 0.415 |
| J090318.55+201245.80 | 25.643 | 19.205 | ... | 19.306 ± 0.093 |
| WD0901+140 | 23.242 | 18.232 | 20.293 ± 0.155 | 16.878 ± 0.021 |
| J090638.59+070059.70 | 14.839 | 15.069 | 15.001 ± 0.014 | 15.203 ± 0.009 |
| J090712.37+364318.40 | 22.54 | 18.027 | ... | 18.036 ± 0.046 |
| J091356.83+404734.70 | 27.32 | 20.305 | ... | 19.836 ± 0.082 |
| J091635.07+385546.20 | 18.211 | 17.087 | 18.238 ± 0.081 | 17.219 ± 0.023 |
| WD0915+526 | 15.512 | 15.568 | 15.400 ± 0.026 | 15.423 ± 0.010 |
| J092252.13+524446.40 | 16.406 | 16.362 | 16.528 ± 0.035 | 16.409 ± 0.015 |
| WD0921+354 | 17.22 | 16.069 | 16.778 ± 0.033 | 16.044 ± 0.010 |
| J092551.68+354000.30 | 26.944 | 20.274 | ... | 20.070 ± 0.139 |
| J092734.28+094711.15 | 21.408 | 18.551 | 20.355 ± 0.204 | 18.630 ± 0.050 |
| J092840.28+184113.70 | 24.412 | 18.522 | ... | 18.335 ± 0.035 |
| J093610.81+074702.20 | 22.864 | 18.671 | ... | 18.742 ± 0.059 |
| J093842.01+541258.40 | 23.043 | 19.147 | 22.189 ± 0.510 | 19.305 ± 0.080 |
| J094104.43+282224.60 | 15.383 | 15.485 | 15.480 ± 0.015 | 15.565 ± 0.010 |
| WD0938+550 | 14.264 | 14.5 | 14.477 ± 0.013 | 14.559 ± 0.006 |
| J094621.44+325128.70 | 26.971 | 20.145 | ... | 19.949 ± 0.094 |
| J094631.59+134736.17 | 15.859 | 16.09 | 16.066 ± 0.031 | 16.176 ± 0.020 |
| WD0943+441 | 13.503 | 13.504 | 13.575 ± 0.009 | 13.788 ± 0.006 |
| J094850.13+131926.90 | 26.773 | 20.017 | ... | 19.982 ± 0.129 |
| J094901.28−001909.60 | 19.082 | 17.227 | 18.881 ± 0.087 | 17.307 ± 0.030 |
| WD0947+325 | 14.245 | 14.67 | 14.353 ± 0.009 | 14.747 ± 0.005 |
| J095257.92+480704.60 | 25.132 | 19.552 | ... | 19.450 ± 0.098 |
| J095259.11+073106.38 | 15.683 | 15.805 | 15.860 ± 0.021 | 15.875 ± 0.014 |
| WD0955+247 | 20.542 | 16.333 | 20.482 ± 0.283 | 16.478 ± 0.027 |
| J095850.56+014724.11 | 15.319 | 15.493 | 15.435 ± 0.014 | 15.512 ± 0.008 |

Table 2.A.1 (cont'd)

| Star | Synthetic FUV mag | Synthetic NUV mag | Observed FUV mag | Observed NUV mag |
|---|---|---|---|---|
| WD1001+333 | 21.176 | 17.887 | 21.246 ± 0.359 | 17.934 ± 0.042 |
| J100356.26+540104.50 | 21.524 | 18.263 | 21.343 ± 0.422 | 18.231 ± 0.057 |
| J100521.06+535408.40 | 27.609 | 20.879 | ... | 20.543 ± 0.178 |
| WD1003−023 | 14.374 | 14.712 | 14.654 ± 0.017 | 14.824 ± 0.011 |
| J100623.08+071212.60 | 20.47 | 17.071 | 19.923 ± 0.198 | 17.017 ± 0.016 |
| J100704.45+322947.00 | 22.134 | 18.73 | 21.795 ± 0.422 | 18.748 ± 0.066 |
| J100720.94+154133.70 | 26.133 | 19.785 | ... | 19.623 ± 0.107 |
| J100900.77+362156.30 | 28.547 | 21.464 | ... | 20.754 ± 0.206 |
| WD1005+642 | 12.792 | 13.144 | 13.099 ± 0.007 | 13.354 ± 0.005 |
| WD1008+382 | 16.518 | 16.489 | 16.611 ± 0.032 | 16.528 ± 0.021 |
| J101414.46+040137.40 | 25.045 | 18.839 | ... | 18.721 ± 0.034 |
| J101415.71+502742.60 | 26.097 | 19.852 | ... | 19.663 ± 0.116 |
| J101502.56+080636.10 | 26.048 | 19.079 | ... | 18.886 ± 0.035 |
| J101548.01+030648.40 | 17.311 | 16.181 | 16.972 ± 0.050 | 16.145 ± 0.019 |
| J101803.74+155157.74 | 14.726 | 15.058 | 14.991 ± 0.013 | 15.213 ± 0.006 |
| WD1019+129 | 14.825 | 15.13 | 15.024 ± 0.019 | 15.231 ± 0.012 |
| J102234.92+460058.80 | 23.748 | 18.385 | ... | 18.885 ± 0.071 |
| J102242.46+165842.70 | 28.026 | 21.122 | ... | 20.732 ± 0.156 |
| WD1022+050 | 16.739 | 15.015 | 15.429 ± 0.015 | 14.909 ± 0.007 |
| J102747.64+192824.20 | 26.22 | 19.716 | ... | 19.595 ± 0.050 |
| WD1026+023 | 15.315 | 14.662 | 14.960 ± 0.018 | 14.612 ± 0.005 |
| J103743.48+485720.80 | 14.397 | 14.781 | 14.520 ± 0.013 | 14.992 ± 0.009 |
| J103746.66+630441.20 | 25.888 | 19.818 | ... | 19.694 ± 0.074 |
| WD1039+412 | 18.502 | 16.823 | 17.903 ± 0.071 | 16.708 ± 0.026 |
| J104411.38+021436.70 | 26.734 | 20.174 | ... | 20.015 ± 0.059 |
| J104709.17+345346.50 | 22.336 | 17.928 | 21.591 ± 0.239 | 17.800 ± 0.023 |
| J104928.88+275422.50 | 15.997 | 15.696 | 16.136 ± 0.029 | 15.781 ± 0.016 |
| J105500.28+350625.20 | 16.947 | 16.926 | 17.065 ± 0.052 | 16.977 ± 0.022 |
| J110136.86+174155.90 | 16.096 | 16.362 | 16.221 ± 0.039 | 16.332 ± 0.021 |
| WD1101+364 | 14.657 | 14.701 | 14.836 ± 0.015 | 14.846 ± 0.008 |
| J110515.32+001626.10 | 15.812 | 15.491 | 15.850 ± 0.027 | 15.533 ± 0.007 |
| J110600.59+621017.20 | 21.303 | 18.213 | 20.994 ± 0.259 | 18.206 ± 0.047 |
| J110604.52+180231.27 | 18.517 | 17.721 | 19.000 ± 0.132 | 17.696 ± 0.038 |
| J110616.42+451855.80 | 25.261 | 19.034 | ... | 18.939 ± 0.073 |
| J111047.52+005421.40 | 22.847 | 18.7 | ... | 18.676 ± 0.036 |
| WD1108+475 | 16.376 | 15.727 | 16.270 ± 0.038 | 15.762 ± 0.016 |

Table 2.A.1 (cont'd)

| Star | Synthetic FUV mag | Synthetic NUV mag | Observed FUV mag | Observed NUV mag |
|---|---|---|---|---|
| J111425.32+380821.00 | 18.885 | 17.114 | 19.022 ± 0.110 | 17.244 ± 0.030 |
| WD1116+026 | 15.774 | 15.035 | 15.694 ± 0.028 | 15.085 ± 0.007 |
| J112146.02+155325.80 | 26.157 | 19.868 | ... | 19.746 ± 0.104 |
| WD1120+439 | 13.754 | 14.29 | 13.859 ± 0.011 | 14.401 ± 0.008 |
| J112518.85+541936.00 | 15.386 | 15.439 | 15.429 ± 0.020 | 15.457 ± 0.009 |
| J112541.71+422334.80 | 20.817 | 17.429 | 19.848 ± 0.162 | 17.231 ± 0.031 |
| J112652.44+591917.00 | 18.869 | 15.919 | 18.451 ± 0.087 | 15.915 ± 0.019 |
| J112731.56+062305.20 | 23.044 | 18.481 | 22.078 ± 0.513 | 18.469 ± 0.052 |
| J112808.00+415012.70 | 22.316 | 18.434 | 21.784 ± 0.471 | 18.347 ± 0.057 |
| WD1126+384 | 13.37 | 13.891 | 13.639 ± 0.006 | 14.290 ± 0.004 |
| J113109.07+064306.10 | 25.385 | 19.293 | ... | 19.163 ± 0.081 |
| J113205.63+363414.70 | 21.906 | 18.194 | 21.807 ± 0.412 | 18.251 ± 0.040 |
| WD1129+155 | 13.557 | 13.785 | 13.680 ± 0.010 | 13.925 ± 0.006 |
| J113325.69+183934.74 | 20.284 | 18.195 | 20.691 ± 0.209 | 18.284 ± 0.030 |
| WD1131+333 | 21.983 | 17.841 | 21.592 ± 0.465 | 17.827 ± 0.038 |
| WD1131+320 | 15.319 | 15.335 | 15.442 ± 0.024 | 15.395 ± 0.014 |
| WD1132+470 | 16.045 | 16.141 | 15.511 ± 0.022 | 15.906 ± 0.011 |
| WD1133+293 | 13.661 | 14.091 | 13.705 ± 0.009 | 14.302 ± 0.007 |
| J113631.30+153044.90 | 26.534 | 20.125 | ... | 20.024 ± 0.134 |
| J113728.31+204109.40 | 25.027 | 19.253 | ... | 19.163 ± 0.044 |
| WD1137+423 | 18.285 | 17.12 | 18.200 ± 0.071 | 17.228 ± 0.022 |
| J114012.81+232204.71 | 20.835 | 19.084 | 21.270 ± 0.302 | 19.141 ± 0.083 |
| WD1143+321 | 13.37 | 13.526 | 13.614 ± 0.009 | 13.692 ± 0.006 |
| WD1145+187 | 12.659 | 13.185 | 13.071 ± 0.008 | 13.545 ± 0.002 |
| J115020.05+251832.20 | 19.372 | 16.538 | 19.233 ± 0.135 | 16.563 ± 0.025 |
| J115052.32+683116.10 | 25.172 | 18.354 | ... | 17.941 ± 0.031 |
| WD1149+410 | 16.072 | 16.135 | 16.148 ± 0.034 | 16.219 ± 0.015 |
| J115421.54+374918.40 | 24.639 | 19.31 | ... | 19.235 ± 0.087 |
| WD1152+371 | 15.596 | 16.129 | 15.766 ± 0.027 | 16.234 ± 0.020 |
| WD1156+291 | 21.809 | 17.95 | 21.067 ± 0.296 | 17.934 ± 0.044 |
| J115939.35+353803.10 | 26.251 | 19.807 | ... | 19.616 ± 0.106 |
| J120003.29+433541.60 | 23.299 | 17.62 | ... | 17.529 ± 0.035 |
| J120347.43−002310.90 | 14.135 | 14.504 | 14.345 ± 0.007 | 14.684 ± 0.005 |
| J120733.82+395324.00 | 23.016 | 18.855 | ... | 18.924 ± 0.075 |
| J120843.33+542946.90 | 24.332 | 18.928 | ... | 18.803 ± 0.047 |
| J121101.67+365319.60 | 20.989 | 18.134 | 20.666 ± 0.251 | 18.163 ± 0.028 |

Table 2.A.1 (cont'd)

| Star | Synthetic FUV mag | Synthetic NUV mag | Observed FUV mag | Observed NUV mag |
|---|---|---|---|---|
| J121135.18+205340.80 | 27.624 | 20.411 | ... | 20.197 ± 0.157 |
| J121314.46+114049.94 | 16.907 | 16.983 | 17.141 ± 0.054 | 17.018 ± 0.031 |
| J121701.40+640402.90 | 25.357 | 19.307 | ... | 19.007 ± 0.081 |
| J121730.20+322633.60 | 25.912 | 19.833 | ... | 19.668 ± 0.111 |
| WD1216+036 | 16.157 | 16.124 | 16.186 ± 0.033 | 16.135 ± 0.020 |
| J121856.18+254557.10 | 16.236 | 16.383 | 16.399 ± 0.031 | 16.422 ± 0.023 |
| J122229.58−024332.50 | 18.541 | 17.296 | 18.459 ± 0.058 | 17.356 ± 0.023 |
| J122724.31+315023.30 | 26.842 | 19.863 | ... | 19.663 ± 0.088 |
| WD1229−012 | 13.575 | 13.903 | 13.612 ± 0.009 | 14.421 ± 0.008 |
| J123143.80+053155.40 | 23.48 | 18.879 | ... | 18.891 ± 0.058 |
| J123324.02+674529.60 | 21.238 | 18.041 | 21.077 ± 0.288 | 17.995 ± 0.029 |
| J123448.90+054718.20 | 25.673 | 19.479 | ... | 19.468 ± 0.075 |
| WD1232+479 | 14.293 | 14.409 | 14.422 ± 0.014 | 14.582 ± 0.006 |
| J123512.35+231829.70 | 24.664 | 19.058 | ... | 18.939 ± 0.064 |
| J123731.44+344822.50 | 22.524 | 18.626 | 21.783 ± 0.292 | 18.692 ± 0.048 |
| J124009.55−031014.20 | 19.796 | 16.811 | 19.932 ± 0.202 | 16.878 ± 0.026 |
| J124140.02−073305.70 | 21.005 | 17.823 | 20.438 ± 0.167 | 17.705 ± 0.027 |
| J124145.51+470621.50 | 21.361 | 18.149 | 21.801 ± 0.329 | 18.309 ± 0.043 |
| J124341.72+480534.60 | 17.862 | 17.199 | 17.364 ± 0.033 | 17.107 ± 0.012 |
| WD1243−194 | 20.059 | 17.2 | 19.620 ± 0.164 | 17.076 ± 0.020 |
| WD1244−125 | 15.201 | 14.958 | 15.212 ± 0.019 | 15.019 ± 0.007 |
| J124748.90−011109.90 | 25.858 | 19.281 | ... | 18.825 ± 0.071 |
| WD1249+182 | 14.554 | 14.888 | 14.722 ± 0.016 | 14.931 ± 0.011 |
| J125607.24+155115.20 | 23.515 | 19.124 | ... | 19.172 ± 0.047 |
| WD1253+105 | 16.699 | 16.475 | 16.819 ± 0.030 | 16.563 ± 0.014 |
| J125804.48+501445.80 | 22.917 | 18.06 | ... | 18.043 ± 0.034 |
| WD1257+047 | 13.828 | 14.236 | 13.831 ± 0.009 | 14.572 ± 0.008 |
| WD1257+032 | 15.069 | 15.316 | 15.239 ± 0.017 | 15.370 ± 0.007 |
| J130014.78+181734.40 | 21.197 | 17.658 | 20.319 ± 0.203 | 17.570 ± 0.037 |
| WD1258+593 | 15.287 | 15.354 | 15.420 ± 0.023 | 15.366 ± 0.006 |
| WD1258+013 | 16.654 | 16.568 | 18.413 ± 0.052 | 17.096 ± 0.014 |
| J130606.98+181123.10 | 24.654 | 19.477 | ... | 19.329 ± 0.070 |
| WD1304+227 | 19.712 | 17.27 | 18.845 ± 0.095 | 17.019 ± 0.031 |
| J130820.81+001330.20 | 16.35 | 16.381 | 16.465 ± 0.016 | 16.476 ± 0.011 |
| WD1310+583 | 17.243 | 14.93 | 16.199 ± 0.016 | 14.947 ± 0.005 |
| J131420.62+070051.10 | 21.592 | 18.226 | 21.209 ± 0.328 | 18.294 ± 0.053 |

Table 2.A.1 (cont'd)

| Star | Synthetic FUV mag | Synthetic NUV mag | Observed FUV mag | Observed NUV mag |
|---|---|---|---|---|
| J132011.39+471222.10 | 24.857 | 19.279 | ... | 19.232 ± 0.060 |
| WD1319+466 | 14.57 | 14.547 | 14.544 ± 0.009 | 14.688 ± 0.007 |
| J132159.59+334507.10 | 23.218 | 19.027 | ... | 19.046 ± 0.058 |
| J132435.13+622637.70 | 19.821 | 17.062 | 19.879 ± 0.191 | 17.136 ± 0.031 |
| J132436.89+085754.00 | 23.002 | 18.137 | ... | 18.149 ± 0.050 |
| J132512.98+085210.10 | 20.769 | 17.88 | 21.334 ± 0.363 | 18.077 ± 0.049 |
| J132742.07+575506.40 | 26.615 | 19.679 | ... | 19.496 ± 0.072 |
| J132937.15−013430.50 | 25.965 | 19.433 | ... | 19.368 ± 0.100 |
| J133652.06+372720.90 | 24.72 | 18.862 | ... | 18.906 ± 0.072 |
| J134027.10+322823.90 | 22.372 | 18.205 | 21.980 ± 0.511 | 18.140 ± 0.050 |
| WD1339+346 | 15.554 | 15.719 | 15.516 ± 0.014 | 15.706 ± 0.010 |
| WD1344+572 | 13.584 | 13.568 | 13.712 ± 0.005 | 13.726 ± 0.003 |
| J134701.30+255256.40 | 26.456 | 19.887 | ... | 19.989 ± 0.134 |
| WD1349+552 | 17.529 | 16.39 | 17.253 ± 0.039 | 16.407 ± 0.016 |
| J135709.49+334802.92 | 16.119 | 16.18 | 16.156 ± 0.049 | 16.227 ± 0.012 |
| J135925.32−003426.40 | 19.565 | 17.492 | 19.535 ± 0.153 | 17.613 ± 0.022 |
| J140617.23+181248.20 | 26.072 | 19.604 | ... | 19.406 ± 0.062 |
| J140625.56+160827.90 | 27.384 | 20.466 | ... | 20.444 ± 0.119 |
| J140945.24+421600.70 | 18.441 | 15.863 | 18.803 ± 0.070 | 16.014 ± 0.012 |
| WD1408+323 | 13.262 | 13.548 | 13.431 ± 0.009 | 13.717 ± 0.007 |
| J141303.60+325646.00 | 20.544 | 17.643 | 20.123 ± 0.240 | 17.559 ± 0.040 |
| J141306.54+075522.98 | 15.386 | 15.493 | 15.418 ± 0.020 | 15.550 ± 0.008 |
| J141454.74+433658.10 | 27.878 | 20.884 | ... | 20.727 ± 0.184 |
| J141600.15+000801.25 | 16.218 | 16.17 | 16.204 ± 0.028 | 16.142 ± 0.019 |
| J142211.13+305618.90 | 22.684 | 18.367 | ... | 18.280 ± 0.032 |
| J143406.76+150817.80 | 16.104 | 16.077 | 16.259 ± 0.034 | 16.141 ± 0.013 |
| J143513.93+505224.80 | 21.414 | 17.958 | 21.375 ± 0.369 | 18.054 ± 0.043 |
| J143624.32+475301.60 | 24.204 | 18.965 | ... | 18.985 ± 0.079 |
| J144111.57+451143.00 | 21.804 | 18.344 | 21.370 ± 0.220 | 18.376 ± 0.035 |
| WD1441+323 | 17.508 | 16.899 | 17.559 ± 0.046 | 17.011 ± 0.022 |
| J144416.16−005236.60 | 27.826 | 21.113 | ... | 20.715 ± 0.246 |
| J144418.26+471704.20 | 20.495 | 17.434 | 20.064 ± 0.169 | 17.514 ± 0.028 |
| J144433.80−005958.80 | 17.596 | 16.709 | 17.226 ± 0.068 | 16.713 ± 0.030 |
| J144433.80−005958.90 | 17.596 | 16.709 | 17.226 ± 0.068 | 16.713 ± 0.030 |
| WD1443+295 | 15.71 | 14.955 | 15.470 ± 0.027 | 14.971 ± 0.012 |
| WD1444+350 | 19.463 | 16.893 | 19.458 ± 0.164 | 16.916 ± 0.020 |

Table 2.A.1 (cont'd)

| Star | Synthetic FUV mag | Synthetic NUV mag | Observed FUV mag | Observed NUV mag |
|---|---|---|---|---|
| J144859.19−023230.10 | 21.632 | 18.059 | 21.109 ± 0.267 | 18.178 ± 0.038 |
| WD1448+411 | 16.197 | 16.131 | 16.220 ± 0.031 | 16.143 ± 0.018 |
| WD1448+077 | 15.385 | 15.474 | 15.559 ± 0.023 | 15.546 ± 0.015 |
| WD1449+513 | 16.236 | 16.422 | 16.276 ± 0.024 | 16.474 ± 0.017 |
| WD1449+168 | 14.349 | 14.74 | 14.387 ± 0.014 | 14.818 ± 0.010 |
| J145308.94+092502.53 | 20.9 | 18.407 | 20.881 ± 0.256 | 18.422 ± 0.048 |
| J145756.35+282749.10 | 22.173 | 18.597 | ... | 18.692 ± 0.049 |
| J150141.15+343158.90 | 14.703 | 15.108 | 14.798 ± 0.009 | 15.183 ± 0.005 |
| WD1459+305 | 13.007 | 13.491 | 13.365 ± 0.007 | 13.765 ± 0.003 |
| WD1501+032 | 15.346 | 15.445 | 15.535 ± 0.018 | 15.598 ± 0.012 |
| J150506.17+325959.50 | 21.913 | 18.01 | 21.662 ± 0.299 | 17.824 ± 0.033 |
| J150617.10+293440.50 | 23.408 | 18.953 | ... | 19.017 ± 0.081 |
| WD1503−093 | 16.016 | 15.492 | 16.113 ± 0.031 | 15.557 ± 0.010 |
| WD1507+220 | 13.996 | 14.351 | 14.227 ± 0.013 | 14.482 ± 0.009 |
| WD1508+548 | 15.212 | 15.424 | 15.341 ± 0.017 | 15.510 ± 0.009 |
| WD1507−105 | 19.283 | 16.42 | 18.704 ± 0.110 | 16.393 ± 0.017 |
| J151109.85+404801.10 | 21.426 | 17.121 | 20.320 ± 0.172 | 17.213 ± 0.020 |
| WD1509+536 | 15.953 | 15.992 | 15.966 ± 0.026 | 16.003 ± 0.017 |
| J151151.36+562450.50 | 21.374 | 17.519 | 21.199 ± 0.368 | 17.449 ± 0.037 |
| WD1515+668 | 19.231 | 16.305 | 18.782 ± 0.100 | 16.266 ± 0.019 |
| J151912.00+123946.50 | 21.99 | 18.32 | 21.319 ± 0.426 | 18.307 ± 0.068 |
| J152006.00+080327.30 | 16.264 | 16.244 | 16.263 ± 0.034 | 16.243 ± 0.021 |
| WD1519+383 | 14.919 | 15.24 | 15.058 ± 0.015 | 15.253 ± 0.008 |
| J152714.52+431302.90 | 17.121 | 16.8 | 17.288 ± 0.035 | 16.916 ± 0.018 |
| J153332.96−020655.90 | 18.169 | 17.038 | 17.734 ± 0.076 | 17.146 ± 0.023 |
| WD1531+184 | 17.069 | 16.619 | 17.012 ± 0.049 | 16.722 ± 0.026 |
| WD1531−022 | 13.2 | 13.499 | 13.635 ± 0.007 | 13.847 ± 0.003 |
| J153417.50+021848.10 | 22.792 | 17.778 | ... | 17.745 ± 0.041 |
| J153424.85+003756.10 | 23.733 | 18.924 | ... | 18.977 ± 0.077 |
| J153615.85+501350.60 | 20.941 | 17.135 | 21.324 ± 0.353 | 17.078 ± 0.032 |
| WD1537+651 | 19.096 | 15.714 | 18.597 ± 0.104 | 15.662 ± 0.017 |
| J153950.86+015400.20 | 22.777 | 18.687 | 21.368 ± 0.388 | 18.801 ± 0.073 |
| WD1537−152 | 15.629 | 15.781 | 15.664 ± 0.022 | 15.851 ± 0.016 |
| J154026.51+234334.72 | 16.229 | 16.369 | 16.349 ± 0.028 | 16.490 ± 0.018 |
| WD1541+650 | 17.642 | 16.183 | 17.002 ± 0.047 | 16.090 ± 0.020 |
| J154934.78+053517.10 | 14.551 | 15.021 | 14.627 ± 0.010 | 15.125 ± 0.009 |

Table 2.A.1 (cont'd)

| Star | Synthetic FUV mag | Synthetic NUV mag | Observed FUV mag | Observed NUV mag |
|---|---|---|---|---|
| J155004.45+220034.45 | 19.312 | 17.308 | 19.951 ± 0.166 | 17.402 ± 0.027 |
| WD1548+149 | 13.975 | 14.385 | 14.165 ± 0.009 | 14.580 ± 0.007 |
| WD1550+183 | 14.722 | 14.757 | 14.931 ± 0.012 | 14.815 ± 0.007 |
| WD1553+353 | 13.598 | 14.02 | 13.711 ± 0.007 | 14.078 ± 0.006 |
| J155937.38+252909.00 | 22.677 | 17.974 | ... | 18.022 ± 0.035 |
| J160216.99+163023.56 | 29.077 | 22.018 | ... | 21.773 ± 0.255 |
| J160353.89+080837.60 | 25.903 | 19.624 | ... | 19.479 ± 0.074 |
| J160554.53−002811.20 | 21.228 | 17.716 | 21.217 ± 0.416 | 17.735 ± 0.041 |
| J160840.92+425652.50 | 22.907 | 18.575 | ... | 18.600 ± 0.030 |
| J160949.60+161919.00 | 26.377 | 19.86 | ... | 19.689 ± 0.088 |
| J161708.73+155438.70 | 14.838 | 15.105 | 15.073 ± 0.015 | 15.283 ± 0.007 |
| WD1619+123 | 14.166 | 14.376 | 14.412 ± 0.017 | 14.551 ± 0.005 |
| J162436.83+321252.50 | 19.073 | 17.383 | 18.459 ± 0.115 | 17.341 ± 0.039 |
| WD1624+477 | 21.929 | 17.816 | 20.782 ± 0.250 | 17.647 ± 0.022 |
| J162813.26+122451.80 | 17.164 | 16.537 | 17.431 ± 0.039 | 16.767 ± 0.015 |
| J162918.99+004551.60 | 21.906 | 18.552 | 21.615 ± 0.408 | 18.586 ± 0.059 |
| WD1631+396 | 13.855 | 14.112 | 13.978 ± 0.013 | 14.421 ± 0.006 |
| J163729.21+011000.90 | 26.625 | 20.005 | ... | 20.015 ± 0.086 |
| WD1636+160 | 16.179 | 15.922 | 16.285 ± 0.022 | 15.989 ± 0.009 |
| J163920.30+403041.50 | 23.325 | 18.508 | ... | 18.542 ± 0.040 |
| WD1654+637 | 15.439 | 15.582 | 15.524 ± 0.015 | 15.608 ± 0.011 |
| J165538.93+253346.00 | 19.934 | 17.488 | 19.803 ± 0.153 | 17.557 ± 0.028 |
| J165559.38+123150.00 | 17.101 | 17.023 | 17.169 ± 0.037 | 17.127 ± 0.022 |
| J165610.85+194202.12 | 16.214 | 16.227 | 16.270 ± 0.024 | 16.267 ± 0.016 |
| J170158.82+611118.10 | 19.606 | 17.678 | 19.682 ± 0.137 | 17.741 ± 0.033 |
| J170653.98+631659.60 | 20.982 | 18.447 | 20.89 ± 0.238 | 18.36 ± 0.043 |
| J171210.43+562925.00 | 26.576 | 20.069 | ... | 20.092 ± 0.152 |
| J172229.99+264527.60 | 15.127 | 15.233 | 15.352 ± 0.018 | 15.349 ± 0.011 |
| J180623.07+231242.10 | 23.488 | 19.336 | ... | 19.342 ± 0.092 |
| J181110.59+242312.90 | 23.916 | 18.893 | ... | 18.691 ± 0.051 |
| J204446.30+153311.90 | 15.383 | 15.57 | 15.507 ± 0.017 | 15.659 ± 0.012 |
| J204531.21+152643.10 | 16.799 | 16.614 | 16.863 ± 0.031 | 16.714 ± 0.020 |
| J204616.23−064426.50 | 22.119 | 18.287 | 21.447 ± 0.324 | 18.184 ± 0.042 |
| WD2051+095 | 15.938 | 16.044 | 16.051 ± 0.025 | 16.107 ± 0.010 |
| J211507.40−074151.60 | 24.24 | 19.025 | ... | 19.051 ± 0.062 |
| J212935.22+001332.10 | 20.448 | 16.824 | 19.911 ± 0.142 | 16.829 ± 0.019 |

Table 2.A.1 (cont'd)

| Star | Synthetic FUV mag | Synthetic NUV mag | Observed FUV mag | Observed NUV mag |
|---|---|---|---|---|
| WD2136+229 | 18.503 | 16.009 | 18.653 ± 0.071 | 16.143 ± 0.014 |
| J220602.42−004632.92 | 15.346 | 15.599 | 15.445 ± 0.014 | 15.681 ± 0.011 |
| J221319.16+292538.96 | 27.937 | 21.299 | ... | 21.438 ± 0.287 |
| WD2220+133 | 14.329 | 14.778 | 14.468 ± 0.015 | 14.919 ± 0.006 |
| WD2226+061 | 14.28 | 14.489 | 14.540 ± 0.011 | 14.613 ± 0.007 |
| WD2240−017 | 21.367 | 17.446 | 20.920 ± 0.288 | 17.419 ± 0.029 |
| J224529.48−100244.30 | 23.05 | 18.393 | ... | 18.339 ± 0.036 |
| WD2254+126 | 17.654 | 16.335 | 17.279 ± 0.036 | 16.376 ± 0.016 |
| WD2303+242 | 17.732 | 16.032 | 17.269 ± 0.029 | 16.06 ± 0.012 |
| WD2306+130 | 15.849 | 15.632 | 15.779 ± 0.019 | 15.611 ± 0.011 |
| WD2306+124 | 14.143 | 14.511 | 14.294 ± 0.009 | 14.673 ± 0.007 |
| WD2314+064 | 15.481 | 15.712 | 15.593 ± 0.024 | 15.818 ± 0.013 |
| WD2318+126 | 16.668 | 16.499 | 16.612 ± 0.028 | 16.513 ± 0.017 |
| WD2322+206 | 16.314 | 15.893 | 16.176 ± 0.023 | 15.917 ± 0.012 |
| WD2333−049 | 19.056 | 16.568 | 18.629 ± 0.107 | 16.565 ± 0.022 |
| WD2336−079 | 15.799 | 13.971 | 15.826 ± 0.026 | 14.173 ± 0.007 |
| WD2347+128 | 18.799 | 16.812 | 18.459 ± 0.082 | 16.800 ± 0.017 |

## 2.B. 250 pc Sample

Table begins on the next page.

Table 2.B.1. Properties of stars beyond 250 pc in our sample. Stars with WD names are from Gianninas et al. (2011).

| Star | Synthetic FUV mag | Synthetic NUV mag | Observed FUV mag | Observed NUV mag |
|---|---|---|---|---|
| J000302.59+240555.80 | 18.699 | 18.73 | 19.461 ± 0.077 | 19.241 ± 0.039 |
| J000626.69+242441.70 | 18.196 | 18.372 | 18.964 ± 0.067 | 18.995 ± 0.031 |
| J001043.55+253829.18 | 15.968 | 16.526 | 16.395 ± 0.020 | 16.890 ± 0.010 |
| J001549.44+245604.91 | 15.691 | 16.253 | 16.038 ± 0.016 | 16.558 ± 0.009 |
| J001712.70+250443.04 | 17.95 | 18.125 | 18.218 ± 0.047 | 18.391 ± 0.026 |
| J002126.69−093714.20 | 17.688 | 17.946 | 18.049 ± 0.035 | 18.252 ± 0.024 |
| WD0019+150 | 15.3 | 15.863 | 15.697 ± 0.018 | 16.160 ± 0.013 |
| J002636.48−100330.50 | 17.116 | 17.444 | 17.552 ± 0.050 | 17.757 ± 0.024 |
| J002806.49+010112.20 | 16.185 | 16.67 | 16.477 ± 0.028 | 16.885 ± 0.022 |
| J003533.74+240253.17 | 17.293 | 17.688 | 17.683 ± 0.057 | 18.139 ± 0.048 |
| J004346.36+254910.50 | 18.482 | 18.482 | 18.695 ± 0.120 | 18.647 ± 0.065 |
| J004648.66+250915.10 | 17.924 | 18.095 | 18.405 ± 0.091 | 18.525 ± 0.043 |
| J005547.78−084507.30 | 13.795 | 14.376 | 14.885 ± 0.014 | 15.160 ± 0.011 |
| J010810.17+183120.46 | 16.957 | 17.351 | 17.586 ± 0.065 | 17.956 ± 0.044 |
| J011100.64+001807.20 | 19.873 | 19.182 | 20.996 ± 0.320 | 19.425 ± 0.109 |
| J011428.32+215310.79 | 16.21 | 16.764 | 16.439 ± 0.034 | 17.012 ± 0.027 |
| J011541.62+310404.20 | 16.432 | 16.952 | 16.963 ± 0.042 | 17.318 ± 0.030 |
| J012041.19+395307.20 | 17.423 | 17.683 | 17.671 ± 0.067 | 17.923 ± 0.033 |
| J012318.14+330014.34 | 17.713 | 17.892 | 17.927 ± 0.043 | 18.12 ± 0.029 |
| J012601.53+332523.49 | 16.21 | 16.702 | 16.917 ± 0.042 | 17.252 ± 0.022 |
| J013250.66+234308.54 | 17.761 | 17.915 | 18.289 ± 0.047 | 18.428 ± 0.029 |
| J013909.83+073941.58 | 18.603 | 18.685 | 19.107 ± 0.123 | 18.897 ± 0.076 |
| J014341.57+222201.56 | 18.849 | 18.833 | 19.571 ± 0.137 | 19.533 ± 0.080 |
| J014413.38+140719.40 | 18.055 | 18.141 | 18.456 ± 0.083 | 18.394 ± 0.055 |
| J014557.72+130610.80 | 16.94 | 17.462 | 17.498 ± 0.055 | 17.922 ± 0.044 |
| J014729.02+235141.11 | 17.182 | 17.444 | 17.652 ± 0.055 | 17.845 ± 0.041 |
| J014847.62−000120.80 | 17.719 | 17.938 | 18.158 ± 0.055 | 18.305 ± 0.036 |
| J015211.73−090502.59 | 17.956 | 18.276 | 18.343 ± 0.060 | 18.483 ± 0.040 |
| J015525.57+064233.41 | 16.331 | 16.852 | 17.205 ± 0.053 | 17.393 ± 0.033 |
| J020952.21+055430.90 | 15.615 | 16.154 | 16.228 ± 0.035 | 16.718 ± 0.025 |
| J021348.57+054223.00 | 18.262 | 18.297 | 18.534 ± 0.088 | 18.545 ± 0.032 |
| J021517.11+001440.50 | 16.876 | 17.236 | 17.289 ± 0.037 | 17.508 ± 0.021 |
| J022446.30−074820.20 | 17.313 | 17.519 | 17.517 ± 0.054 | 17.761 ± 0.042 |
| J023543.18−055442.07 | 17.218 | 17.469 | 17.420 ± 0.052 | 17.603 ± 0.037 |
| J025325.82−002751.60 | 17.305 | 17.598 | 17.906 ± 0.077 | 17.995 ± 0.045 |
| J025507.00−080852.20 | 16.78 | 17.157 | 17.280 ± 0.044 | 17.467 ± 0.026 |

Table 2.B.1 (cont'd)

| Star | Synthetic FUV mag | Synthetic NUV mag | Observed FUV mag | Observed NUV mag |
|---|---|---|---|---|
| J031504.58−065727.10 | 16.982 | 17.263 | 17.671 ± 0.035 | 17.914 ± 0.027 |
| J032215.59−054707.30 | 16.673 | 17.027 | 16.741 ± 0.039 | 17.182 ± 0.031 |
| J032400.23+055536.70 | 18.568 | 18.493 | 19.524 ± 0.089 | 19.328 ± 0.064 |
| J032430.71+040054.90 | 18.072 | 18.221 | 18.562 ± 0.075 | 18.743 ± 0.052 |
| J032615.34+000221.70 | 17.129 | 17.552 | 18.000 ± 0.071 | 18.370 ± 0.056 |
| J032726.26−071150.00 | 15.585 | 16.188 | 16.047 ± 0.028 | 16.667 ± 0.022 |
| J033257.68−070434.90 | 15.557 | 16.124 | 16.012 ± 0.023 | 16.480 ± 0.018 |
| J035416.31+095738.40 | 17.833 | 17.982 | 18.346 ± 0.072 | 18.653 ± 0.051 |
| J042353.85+065353.10 | 17.126 | 17.404 | 17.692 ± 0.046 | 18.055 ± 0.036 |
| J044424.97−053436.10 | 16.339 | 16.81 | 16.674 ± 0.029 | 17.075 ± 0.025 |
| J060055.10+643234.50 | 16.77 | 17.251 | 17.342 ± 0.056 | 17.819 ± 0.043 |
| J060255.98+632304.80 | 20.575 | 19.161 | 20.192 ± 0.246 | 19.737 ± 0.117 |
| J061938.24+635656.50 | 13.634 | 14.284 | 14.734 ± 0.012 | 15.244 ± 0.008 |
| J064924.84+273256.90 | 16.787 | 17.265 | 17.185 ± 0.033 | 17.471 ± 0.029 |
| J070954.46+403210.20 | 17.839 | 18.017 | 18.102 ± 0.057 | 18.250 ± 0.038 |
| J071201.60+381655.30 | 16.685 | 17.142 | 16.957 ± 0.041 | 17.356 ± 0.023 |
| J072020.88+364706.30 | 15.737 | 16.188 | 15.959 ± 0.017 | 16.367 ± 0.014 |
| J072308.84+370214.40 | 16.576 | 17.112 | 16.880 ± 0.031 | 17.336 ± 0.025 |
| J072559.68+353836.30 | 17.328 | 17.568 | 17.600 ± 0.039 | 17.763 ± 0.023 |
| J072837.66+405049.52 | 17.226 | 17.595 | 17.588 ± 0.040 | 17.813 ± 0.026 |
| J073247.77+213346.80 | 18.042 | 18.212 | 18.316 ± 0.061 | 18.354 ± 0.043 |
| J073511.20+265708.35 | 15.538 | 16.103 | 15.829 ± 0.017 | 16.289 ± 0.010 |
| J073702.90+473749.20 | 16.543 | 16.886 | 17.248 ± 0.036 | 17.795 ± 0.028 |
| J073852.47+220331.10 | 16.646 | 17.06 | 16.931 ± 0.029 | 17.208 ± 0.023 |
| J074059.12+380810.20 | 15.647 | 16.215 | 16.191 ± 0.022 | 16.673 ± 0.015 |
| J074206.21+265355.14 | 17.457 | 17.836 | 17.774 ± 0.048 | 17.974 ± 0.026 |
| J074243.02+394512.38 | 16.571 | 17.109 | 16.975 ± 0.029 | 17.450 ± 0.025 |
| J074747.06+243802.10 | 17.539 | 17.789 | 17.815 ± 0.045 | 17.998 ± 0.032 |
| J074749.82+664949.70 | 18.034 | 18.224 | 18.289 ± 0.084 | 18.382 ± 0.058 |
| J074803.72+300001.80 | 16.576 | 17.11 | 16.949 ± 0.039 | 17.404 ± 0.024 |
| J075052.61+135622.56 | 16.751 | 17.18 | 17.052 ± 0.034 | 17.305 ± 0.023 |
| J075115.11+433513.90 | 17.693 | 17.997 | 18.058 ± 0.054 | 18.181 ± 0.033 |
| J075129.40+340128.34 | 16.844 | 17.284 | 17.127 ± 0.045 | 17.487 ± 0.026 |
| J075144.34+243954.40 | 17.152 | 17.503 | 17.583 ± 0.042 | 17.752 ± 0.030 |
| J075301.85+831017.10 | 16.641 | 17.1 | 16.755 ± 0.028 | 17.178 ± 0.023 |
| J075405.35+132708.70 | 14.029 | 14.707 | 14.287 ± 0.009 | 14.935 ± 0.008 |

Table 2.B.1 (cont'd)

| Star | Synthetic FUV mag | Synthetic NUV mag | Observed FUV mag | Observed NUV mag |
|---|---|---|---|---|
| J075455.50+164217.10 | 18.058 | 18.179 | 18.426 ± 0.067 | 18.335 ± 0.046 |
| J075722.06+521043.32 | 17.984 | 18.271 | 18.255 ± 0.073 | 18.720 ± 0.062 |
| J075821.12+274101.72 | 16.445 | 16.996 | 16.661 ± 0.029 | 17.150 ± 0.021 |
| J075825.99+200040.32 | 17.443 | 17.765 | 17.728 ± 0.060 | 18.017 ± 0.040 |
| J080020.33+455730.74 | 17.221 | 17.5 | 17.547 ± 0.049 | 17.896 ± 0.045 |
| J080405.14+394436.10 | 17.663 | 17.735 | 18.004 ± 0.082 | 18.016 ± 0.042 |
| J080624.33+395307.12 | 17.782 | 18.007 | 18.22 ± 0.079 | 18.307 ± 0.049 |
| J080644.92+193427.70 | 16.611 | 17.106 | 16.912 ± 0.055 | 17.370 ± 0.038 |
| J080751.70+282907.50 | 17.649 | 17.887 | 17.897 ± 0.050 | 17.967 ± 0.028 |
| J080758.75+134419.10 | 16.108 | 16.685 | 16.366 ± 0.025 | 16.815 ± 0.022 |
| J080808.67+063815.40 | 16.527 | 17.0 | 16.849 ± 0.029 | 17.296 ± 0.023 |
| J080920.82+383358.10 | 17.717 | 17.971 | 17.820 ± 0.069 | 18.120 ± 0.037 |
| J080921.89+192400.10 | 14.63 | 15.354 | 14.46 ± 0.016 | 15.142 ± 0.005 |
| J080954.58+322315.30 | 16.66 | 17.111 | 16.878 ± 0.043 | 17.313 ± 0.024 |
| J081035.27−063234.70 | 16.917 | 17.442 | 17.384 ± 0.061 | 17.800 ± 0.040 |
| J081234.94+040852.10 | 15.575 | 16.075 | 15.825 ± 0.022 | 16.189 ± 0.017 |
| J081254.33+501620.30 | 15.575 | 16.133 | 15.985 ± 0.022 | 16.482 ± 0.015 |
| J081331.82+272203.96 | 14.714 | 15.259 | 15.010 ± 0.014 | 15.521 ± 0.010 |
| J081540.18+081238.40 | 16.048 | 16.564 | 16.310 ± 0.021 | 16.778 ± 0.017 |
| J081640.91+362148.71 | 18.092 | 18.369 | 18.427 ± 0.063 | 18.771 ± 0.049 |
| J081658.25+444953.40 | 16.717 | 17.071 | 17.143 ± 0.032 | 17.387 ± 0.024 |
| J081721.55+164710.18 | 16.58 | 17.08 | 16.807 ± 0.026 | 17.029 ± 0.014 |
| J081806.88+121155.39 | 15.565 | 16.126 | 15.771 ± 0.019 | 16.264 ± 0.017 |
| WD0814+569 | 14.441 | 15.037 | 15.005 ± 0.017 | 15.406 ± 0.014 |
| J081845.58+485855.20 | 16.814 | 17.204 | 17.165 ± 0.049 | 17.520 ± 0.036 |
| J081934.42+322412.06 | 16.187 | 16.711 | 16.621 ± 0.035 | 17.032 ± 0.018 |
| J082010.35+454301.81 | 17.804 | 17.95 | 18.199 ± 0.086 | 18.404 ± 0.056 |
| J082220.50+494246.37 | 15.946 | 16.45 | 16.347 ± 0.032 | 16.769 ± 0.025 |
| J082251.66+452928.10 | 16.865 | 17.264 | 17.217 ± 0.045 | 17.551 ± 0.034 |
| J082407.44+314210.51 | 17.972 | 18.14 | 18.283 ± 0.054 | 18.406 ± 0.040 |
| J082437.69+474851.88 | 15.99 | 16.481 | 16.299 ± 0.030 | 16.706 ± 0.024 |
| J082706.21+311536.00 | 16.047 | 16.595 | 16.341 ± 0.023 | 16.852 ± 0.019 |
| J082717.14+163250.39 | 17.369 | 17.601 | 17.551 ± 0.063 | 17.747 ± 0.042 |
| J082944.47+530101.00 | 16.522 | 17.08 | 17.086 ± 0.032 | 17.596 ± 0.026 |
| J082954.66+485226.70 | 17.059 | 17.414 | 17.413 ± 0.038 | 17.710 ± 0.028 |
| J083029.77+085014.20 | 17.355 | 17.605 | 17.397 ± 0.036 | 16.214 ± 0.015 |

Table 2.B.1 (cont'd)

| Star | Synthetic FUV mag | Synthetic NUV mag | Observed FUV mag | Observed NUV mag |
|---|---|---|---|---|
| J083115.34−051815.90 | 15.009 | 15.565 | 15.250 ± 0.021 | 15.704 ± 0.016 |
| J083138.31+422135.10 | 17.377 | 17.734 | 17.722 ± 0.045 | 18.035 ± 0.021 |
| J083238.24+550532.30 | 16.884 | 17.276 | 17.264 ± 0.036 | 17.517 ± 0.025 |
| J083330.83−044857.20 | 18.071 | 18.242 | 18.346 ± 0.065 | 18.461 ± 0.042 |
| J083337.06+481451.50 | 17.458 | 17.655 | 17.665 ± 0.060 | 17.820 ± 0.044 |
| J083423.17+043745.02 | 17.712 | 17.946 | 17.949 ± 0.052 | 18.107 ± 0.039 |
| J083650.28+155326.40 | 14.759 | 15.402 | 15.057 ± 0.014 | 15.553 ± 0.006 |
| J083838.53+065240.08 | 14.783 | 15.475 | 15.236 ± 0.014 | 15.7 ± 0.011 |
| J084151.11+225316.20 | 16.114 | 16.667 | 16.477 ± 0.039 | 16.957 ± 0.028 |
| J084430.27+480327.50 | 17.618 | 17.928 | 17.910 ± 0.065 | 18.162 ± 0.048 |
| J084529.99+290718.20 | 17.219 | 17.413 | 17.434 ± 0.041 | 17.494 ± 0.027 |
| J084607.76+544012.80 | 17.358 | 17.772 | 17.804 ± 0.050 | 18.156 ± 0.038 |
| J084618.45+154419.93 | 15.708 | 16.334 | 16.291 ± 0.035 | 16.723 ± 0.027 |
| J084639.28+091406.80 | 15.417 | 16.082 | 16.112 ± 0.020 | 16.538 ± 0.016 |
| J085135.27+161837.08 | 16.758 | 17.009 | 16.967 ± 0.038 | 17.134 ± 0.028 |
| J085209.16+841150.30 | 16.702 | 17.23 | 16.991 ± 0.029 | 17.519 ± 0.026 |
| J085230.99+533901.80 | 15.817 | 16.398 | 15.948 ± 0.024 | 16.544 ± 0.020 |
| J085314.76+133620.38 | 16.065 | 16.494 | 16.217 ± 0.019 | 16.578 ± 0.016 |
| J085528.43+610211.30 | 15.022 | 15.571 | 15.439 ± 0.014 | 15.943 ± 0.011 |
| J085634.52+502748.30 | 15.581 | 16.14 | 15.781 ± 0.028 | 16.264 ± 0.014 |
| J085638.83+093818.06 | 17.359 | 17.705 | 17.597 ± 0.051 | 17.942 ± 0.036 |
| J085727.50+025805.20 | 17.14 | 17.416 | 17.330 ± 0.043 | 17.567 ± 0.031 |
| J085727.50+025805.20 | 17.14 | 17.416 | 17.330 ± 0.043 | 17.567 ± 0.031 |
| J085804.06+531031.90 | 16.443 | 16.994 | 16.849 ± 0.042 | 17.319 ± 0.023 |
| J085838.73+170147.93 | 17.32 | 17.634 | 17.629 ± 0.056 | 17.777 ± 0.041 |
| J085944.19+504051.00 | 15.391 | 15.954 | 15.702 ± 0.022 | 16.191 ± 0.013 |
| J090029.66+181941.80 | 15.984 | 16.396 | 16.239 ± 0.036 | 16.589 ± 0.024 |
| J090059.86+062920.60 | 16.511 | 16.96 | 17.074 ± 0.049 | 17.310 ± 0.031 |
| J090136.12+162704.20 | 15.025 | 15.673 | 15.523 ± 0.016 | 16.013 ± 0.014 |
| J090250.50+173149.30 | 17.295 | 17.629 | 17.551 ± 0.042 | 17.867 ± 0.034 |
| J090254.09+575821.90 | 17.646 | 17.825 | 17.778 ± 0.042 | 17.895 ± 0.031 |
| J090348.57+083456.50 | 17.357 | 17.607 | 17.819 ± 0.045 | 17.831 ± 0.031 |
| J090352.80+193643.60 | 14.53 | 15.115 | 14.724 ± 0.017 | 15.349 ± 0.012 |
| J090416.45+584301.10 | 16.397 | 16.852 | 16.658 ± 0.032 | 17.017 ± 0.021 |
| J090431.82+143747.50 | 16.525 | 17.056 | 17.042 ± 0.031 | 17.538 ± 0.027 |
| J090525.49+394339.10 | 17.729 | 17.843 | 17.861 ± 0.061 | 18.007 ± 0.031 |

Table 2.B.1 (cont'd)

| Star | Synthetic FUV mag | Synthetic NUV mag | Observed FUV mag | Observed NUV mag |
|---|---|---|---|---|
| J090611.00+414114.30 | 15.368 | 15.942 | 15.486 ± 0.014 | 16.025 ± 0.010 |
| J090726.02+174135.88 | 16.811 | 17.258 | 17.164 ± 0.040 | 17.44 ± 0.028 |
| J090757.30+084524.90 | 18.522 | 18.467 | 18.809 ± 0.066 | 18.858 ± 0.040 |
| J091008.92+835535.50 | 18.188 | 18.116 | 18.160 ± 0.052 | 18.136 ± 0.035 |
| J091109.46+165345.40 | 16.464 | 16.974 | 16.871 ± 0.033 | 17.298 ± 0.026 |
| J091145.12+353135.60 | 18.069 | 18.325 | 17.452 ± 0.062 | 17.489 ± 0.037 |
| J091258.85+091815.60 | 16.699 | 17.076 | 17.127 ± 0.034 | 17.431 ± 0.019 |
| J091438.68+233127.60 | 15.973 | 16.476 | 16.450 ± 0.044 | 16.783 ± 0.014 |
| J091601.87+200758.10 | 15.25 | 15.803 | 15.660 ± 0.022 | 16.078 ± 0.011 |
| J091616.66+155727.50 | 16.607 | 17.077 | 16.811 ± 0.037 | 17.321 ± 0.027 |
| J091719.14+195438.66 | 14.697 | 15.263 | 15.014 ± 0.016 | 15.456 ± 0.007 |
| J091729.86+122727.90 | 16.51 | 16.942 | 16.746 ± 0.027 | 17.170 ± 0.024 |
| J091841.84+061702.10 | 13.711 | 14.302 | 14.003 ± 0.007 | 14.549 ± 0.006 |
| J092010.55+045721.10 | 14.512 | 15.188 | 15.077 ± 0.013 | 15.670 ± 0.010 |
| WD0920+306 | 15.356 | 15.615 | 15.493 ± 0.016 | 15.656 ± 0.010 |
| J092404.84+593128.80 | 16.514 | 16.947 | 16.792 ± 0.028 | 17.068 ± 0.010 |
| J092415.31+563750.60 | 17.114 | 17.45 | 17.308 ± 0.046 | 17.628 ± 0.035 |
| J092416.44+671013.20 | 15.836 | 16.337 | 16.492 ± 0.035 | 16.786 ± 0.027 |
| J092454.58+543422.30 | 15.736 | 16.266 | 16.069 ± 0.030 | 16.557 ± 0.015 |
| J092526.56+535312.30 | 17.424 | 17.76 | 17.685 ± 0.055 | 17.921 ± 0.029 |
| J092553.76+540748.40 | 17.866 | 18.149 | 17.895 ± 0.063 | 18.268 ± 0.034 |
| J092646.30+122135.68 | 16.548 | 16.971 | 16.831 ± 0.028 | 17.194 ± 0.022 |
| J092905.46+061118.70 | 15.724 | 16.325 | 16.328 ± 0.022 | 16.836 ± 0.018 |
| J093000.80+651412.50 | 16.244 | 16.754 | 16.674 ± 0.038 | 17.048 ± 0.027 |
| J093047.08+160012.53 | 14.81 | 15.383 | 15.220 ± 0.018 | 15.650 ± 0.015 |
| J093058.92+074454.40 | 15.348 | 15.91 | 15.785 ± 0.019 | 16.275 ± 0.015 |
| J093132.67+115454.29 | 16.543 | 17.0 | 16.760 ± 0.032 | 17.225 ± 0.023 |
| J093311.28+205250.70 | 16.675 | 17.068 | 17.041 ± 0.032 | 17.363 ± 0.023 |
| J093410.29+553149.60 | 18.696 | 18.748 | 19.136 ± 0.133 | 18.945 ± 0.049 |
| J093515.96+562042.11 | 15.58 | 16.219 | 16.056 ± 0.028 | 16.518 ± 0.022 |
| WD0934+337 | 15.031 | 15.488 | 15.189 ± 0.013 | 15.617 ± 0.009 |
| J093921.83+264401.10 | 15.009 | 15.649 | 15.334 ± 0.016 | 15.870 ± 0.012 |
| J093957.04+644634.20 | 15.266 | 15.772 | 16.190 ± 0.028 | 16.679 ± 0.021 |
| J094200.06+312920.20 | 16.276 | 16.595 | 16.442 ± 0.023 | 16.686 ± 0.017 |
| J094203.19+544630.20 | 15.405 | 15.958 | 15.631 ± 0.023 | 16.112 ± 0.013 |
| J094342.17+000923.20 | 16.798 | 17.207 | 17.521 ± 0.053 | 17.812 ± 0.040 |

Table 2.B.1 (cont'd)

| Star | Synthetic FUV mag | Synthetic NUV mag | Observed FUV mag | Observed NUV mag |
|---|---|---|---|---|
| J094537.90+503038.05 | 18.132 | 18.343 | 18.425 ± 0.093 | 18.340 ± 0.053 |
| J094658.77+471024.28 | 17.078 | 17.379 | 17.207 ± 0.046 | 17.526 ± 0.036 |
| J094913.84+315930.10 | 16.534 | 16.916 | 16.719 ± 0.027 | 16.998 ± 0.021 |
| J094927.59+042508.40 | 15.137 | 15.751 | 15.576 ± 0.016 | 16.131 ± 0.013 |
| J094940.37+032425.50 | 14.964 | 15.55 | 15.177 ± 0.013 | 15.732 ± 0.011 |
| J095005.33+495548.94 | 15.174 | 15.718 | 15.293 ± 0.018 | 15.827 ± 0.015 |
| J095329.07+092409.60 | 15.26 | 15.866 | 15.692 ± 0.023 | 16.244 ± 0.014 |
| J095536.62+041112.40 | 16.42 | 16.86 | 16.664 ± 0.027 | 17.076 ± 0.020 |
| J095629.73+641430.20 | 17.266 | 17.529 | 17.437 ± 0.047 | 17.657 ± 0.035 |
| J095951.46+355244.29 | 17.268 | 17.569 | 17.416 ± 0.039 | 17.667 ± 0.028 |
| J100200.17+151007.39 | 16.803 | 17.272 | 17.083 ± 0.043 | 17.544 ± 0.035 |
| J100605.29+450404.19 | 15.226 | 15.787 | 15.337 ± 0.020 | 15.893 ± 0.016 |
| J100651.72+490053.88 | 17.789 | 17.926 | 17.942 ± 0.067 | 18.05 ± 0.043 |
| J100756.04+180848.70 | 17.181 | 17.517 | 17.534 ± 0.042 | 17.811 ± 0.029 |
| J100931.54+025646.07 | 17.388 | 17.719 | 17.683 ± 0.068 | 17.975 ± 0.056 |
| J101039.45+542519.30 | 16.299 | 16.8 | 16.658 ± 0.034 | 17.040 ± 0.028 |
| J101205.63+615651.90 | 15.645 | 16.228 | 16.011 ± 0.018 | 16.475 ± 0.012 |
| J101328.17+061207.40 | 14.38 | 14.984 | 14.670 ± 0.017 | 15.165 ± 0.006 |
| WD1011+335 | 16.979 | 17.34 | 17.170 ± 0.053 | 17.558 ± 0.039 |
| J101612.78+390115.06 | 16.733 | 17.102 | 16.718 ± 0.034 | 17.169 ± 0.028 |
| J101924.90+280748.00 | 15.776 | 16.324 | 16.131 ± 0.021 | 16.629 ± 0.017 |
| J102010.07−014228.98 | 17.741 | 17.985 | 18.277 ± 0.063 | 18.370 ± 0.043 |
| J102016.09+054919.16 | 17.325 | 17.649 | 17.752 ± 0.067 | 17.870 ± 0.032 |
| J102042.68+041302.80 | 16.943 | 17.297 | 17.049 ± 0.048 | 17.422 ± 0.022 |
| J102157.96+291931.30 | 17.818 | 18.025 | 18.078 ± 0.049 | 18.239 ± 0.036 |
| J102443.90+121437.97 | 17.364 | 17.654 | 17.769 ± 0.065 | 17.958 ± 0.026 |
| J102449.53+230710.13 | 17.615 | 17.892 | 17.786 ± 0.051 | 18.020 ± 0.034 |
| J102549.72+003906.20 | 14.299 | 14.864 | 14.761 ± 0.020 | 15.128 ± 0.014 |
| J102625.20+040534.30 | 16.002 | 16.487 | 16.336 ± 0.034 | 16.756 ± 0.028 |
| J102632.82+621313.52 | 18.338 | 18.509 | 18.470 ± 0.092 | 18.496 ± 0.040 |
| J102955.94+145355.28 | 17.024 | 17.217 | 17.931 ± 0.052 | 17.774 ± 0.024 |
| J103016.66+494520.70 | 15.31 | 15.881 | 15.542 ± 0.021 | 16.097 ± 0.017 |
| J103032.45+633317.70 | 15.065 | 15.626 | 15.211 ± 0.020 | 15.715 ± 0.015 |
| J103158.27+012053.59 | 17.972 | 18.176 | 18.260 ± 0.086 | 18.457 ± 0.028 |
| J103233.61+475908.96 | 17.201 | 17.525 | 17.325 ± 0.050 | 17.556 ± 0.021 |
| J103326.58+614816.79 | 17.788 | 18.122 | 17.828 ± 0.048 | 18.189 ± 0.037 |

Table 2.B.1 (cont'd)

| Star | Synthetic FUV mag | Synthetic NUV mag | Observed FUV mag | Observed NUV mag |
|---|---|---|---|---|
| J103500.15+180750.70 | 17.094 | 17.351 | 17.300 ± 0.058 | 17.562 ± 0.018 |
| J103510.47+605546.06 | 17.359 | 17.806 | 17.654 ± 0.037 | 17.830 ± 0.032 |
| J103906.00+654555.50 | 16.616 | 17.099 | 16.847 ± 0.040 | 17.294 ± 0.031 |
| J103935.39+084559.20 | 16.431 | 16.817 | 16.598 ± 0.033 | 16.990 ± 0.020 |
| J104002.57+195305.28 | 16.251 | 16.747 | 16.621 ± 0.035 | 17.015 ± 0.019 |
| J104109.60+500945.07 | 16.2 | 16.705 | 16.367 ± 0.033 | 16.874 ± 0.028 |
| J104216.68+123112.97 | 17.577 | 17.841 | 17.838 ± 0.070 | 18.114 ± 0.028 |
| J104314.98+353519.64 | 15.847 | 16.301 | 16.182 ± 0.031 | 16.475 ± 0.022 |
| J104419.01+405553.00 | 15.4 | 15.925 | 15.571 ± 0.022 | 16.072 ± 0.018 |
| J104546.43+091825.16 | 16.314 | 16.855 | 16.617 ± 0.035 | 17.150 ± 0.015 |
| J104650.65+533521.50 | 17.977 | 18.084 | 18.079 ± 0.072 | 18.231 ± 0.025 |
| J104744.13+663734.30 | 16.985 | 17.32 | 17.071 ± 0.041 | 17.416 ± 0.030 |
| J105331.07+435656.26 | 17.81 | 17.994 | 17.936 ± 0.052 | 18.107 ± 0.023 |
| J105525.18+441608.29 | 16.843 | 17.105 | 16.884 ± 0.029 | 17.096 ± 0.014 |
| J105549.60−010025.88 | 17.916 | 18.141 | 18.385 ± 0.087 | 18.490 ± 0.042 |
| J105725.64+640352.10 | 17.827 | 18.069 | 18.048 ± 0.052 | 18.265 ± 0.038 |
| J105802.33+361156.60 | 16.191 | 16.716 | 16.574 ± 0.039 | 16.964 ± 0.030 |
| J105811.27+475752.00 | 15.645 | 16.203 | 15.89 ± 0.019 | 16.420 ± 0.013 |
| J105827.19+172117.57 | 17.588 | 17.776 | 17.867 ± 0.067 | 18.033 ± 0.048 |
| J105842.58+175331.52 | 16.669 | 17.071 | 16.881 ± 0.041 | 17.272 ± 0.031 |
| J110219.76+121253.90 | 16.795 | 17.262 | 17.104 ± 0.048 | 17.544 ± 0.038 |
| J110603.15+472253.46 | 15.458 | 15.908 | 15.819 ± 0.023 | 16.149 ± 0.012 |
| J110606.72+514002.37 | 17.638 | 17.87 | 17.825 ± 0.068 | 17.995 ± 0.020 |
| J110631.93+505302.00 | 15.955 | 16.477 | 16.212 ± 0.028 | 16.704 ± 0.011 |
| J110750.61+164011.57 | 17.441 | 17.754 | 17.726 ± 0.052 | 17.961 ± 0.037 |
| J111205.50+630148.49 | 17.337 | 17.776 | 17.564 ± 0.050 | 17.963 ± 0.039 |
| J111353.35+595322.80 | 17.915 | 18.208 | 18.112 ± 0.090 | 18.227 ± 0.056 |
| J111356.47+131614.59 | 15.256 | 15.828 | 15.532 ± 0.020 | 15.940 ± 0.016 |
| J111603.78+494343.90 | 15.524 | 16.132 | 15.847 ± 0.014 | 16.313 ± 0.008 |
| J111859.80+535725.00 | 17.715 | 18.05 | 17.919 ± 0.063 | 18.198 ± 0.038 |
| J112002.74+442828.32 | 18.604 | 18.639 | 18.825 ± 0.105 | 18.899 ± 0.074 |
| J112013.68+485231.02 | 17.422 | 17.66 | 17.640 ± 0.045 | 17.745 ± 0.018 |
| J112215.99+671145.90 | 14.364 | 14.981 | 14.547 ± 0.016 | 15.049 ± 0.011 |
| J112254.17+620606.32 | 16.743 | 17.285 | 16.971 ± 0.037 | 17.361 ± 0.027 |
| J112311.08+425830.55 | 17.668 | 17.84 | 17.777 ± 0.063 | 17.958 ± 0.043 |
| J112432.14+405950.25 | 17.004 | 17.335 | 17.332 ± 0.049 | 17.541 ± 0.034 |

Table 2.B.1 (cont'd)

| Star | Synthetic FUV mag | Synthetic NUV mag | Observed FUV mag | Observed NUV mag |
|---|---|---|---|---|
| J112531.09+570406.11 | 17.468 | 17.65 | 17.793 ± 0.049 | 17.768 ± 0.029 |
| J112613.52−002109.70 | 17.418 | 17.662 | 17.600 ± 0.053 | 17.859 ± 0.038 |
| J112627.62+240903.80 | 16.63 | 17.049 | 17.036 ± 0.052 | 17.334 ± 0.033 |
| J112729.52+672230.80 | 17.094 | 17.392 | 17.148 ± 0.046 | 17.427 ± 0.024 |
| J112740.90−024638.80 | 16.346 | 16.752 | 16.777 ± 0.043 | 17.094 ± 0.029 |
| J112815.61+171408.90 | 14.404 | 15.074 | 14.703 ± 0.018 | 15.345 ± 0.012 |
| J112905.44+092327.85 | 17.073 | 17.375 | 17.493 ± 0.048 | 17.714 ± 0.034 |
| J113027.71+450558.62 | 16.971 | 17.28 | 17.114 ± 0.030 | 17.422 ± 0.020 |
| J113118.07+573937.39 | 17.643 | 17.808 | 17.986 ± 0.078 | 18.097 ± 0.051 |
| J113205.55+370847.36 | 16.119 | 16.658 | 16.320 ± 0.022 | 16.753 ± 0.015 |
| J113251.95+223356.46 | 17.004 | 17.461 | 17.352 ± 0.056 | 17.679 ± 0.041 |
| J113254.32+460714.34 | 17.977 | 18.184 | 18.276 ± 0.089 | 18.459 ± 0.042 |
| WD1131+315 | 16.701 | 17.125 | 16.893 ± 0.047 | 17.417 ± 0.037 |
| J113652.75+145448.02 | 17.245 | 17.404 | 17.902 ± 0.069 | 17.802 ± 0.044 |
| J113934.58+332515.10 | 16.342 | 16.851 | 16.638 ± 0.040 | 16.939 ± 0.029 |
| J114033.35+453644.30 | 17.577 | 17.811 | 17.812 ± 0.073 | 18.036 ± 0.042 |
| J114404.71+052951.40 | 16.273 | 16.671 | 16.534 ± 0.031 | 16.886 ± 0.024 |
| J114551.39+101508.40 | 16.085 | 16.593 | 16.473 ± 0.033 | 16.899 ± 0.026 |
| J115317.34+191152.80 | 14.58 | 15.24 | 15.024 ± 0.021 | 15.652 ± 0.014 |
| J115446.94+265740.10 | 15.996 | 16.503 | 16.34 ± 0.031 | 16.717 ± 0.024 |
| J115552.00+184914.66 | 16.89 | 17.359 | 17.235 ± 0.060 | 17.520 ± 0.024 |
| J115632.07+113848.70 | 17.116 | 17.465 | 17.411 ± 0.051 | 17.652 ± 0.039 |
| J115712.38+125239.72 | 17.568 | 17.803 | 17.992 ± 0.082 | 17.986 ± 0.041 |
| J115804.65+595902.13 | 18.188 | 18.437 | 18.486 ± 0.096 | 18.58 ± 0.066 |
| J120226.21+300035.10 | 16.64 | 17.139 | 16.996 ± 0.046 | 17.336 ± 0.036 |
| J120621.23+464122.80 | 16.233 | 16.71 | 16.439 ± 0.033 | 16.914 ± 0.026 |
| J120715.23+105338.33 | 17.379 | 17.738 | 17.860 ± 0.069 | 18.048 ± 0.047 |
| J120924.26+095256.60 | 15.455 | 16.045 | 15.777 ± 0.027 | 16.278 ± 0.021 |
| J121235.73+085449.25 | 17.908 | 18.145 | 18.152 ± 0.089 | 18.268 ± 0.060 |
| J121756.20+021046.50 | 14.484 | 15.165 | 14.697 ± 0.013 | 15.319 ± 0.011 |
| J122221.95+171539.40 | 16.511 | 16.984 | 16.774 ± 0.038 | 17.177 ± 0.031 |
| J122452.26+435531.74 | 17.818 | 17.974 | 17.977 ± 0.084 | 18.097 ± 0.045 |
| J122638.84+175201.45 | 16.378 | 16.788 | 16.716 ± 0.039 | 17.055 ± 0.028 |
| J122722.85+021507.50 | 15.652 | 16.212 | 15.987 ± 0.031 | 16.417 ± 0.021 |
| J122748.80+195548.32 | 17.223 | 17.543 | 17.777 ± 0.081 | 18.044 ± 0.049 |
| J123004.20+085616.58 | 18.616 | 18.81 | 18.738 ± 0.113 | 19.033 ± 0.089 |

Table 2.B.1 (cont'd)

| Star | Synthetic FUV mag | Synthetic NUV mag | Observed FUV mag | Observed NUV mag |
|---|---|---|---|---|
| J123531.70+643734.70 | 16.59 | 17.128 | 16.879 ± 0.052 | 17.403 ± 0.035 |
| J123549.89+154319.30 | 16.744 | 17.009 | 17.042 ± 0.057 | 17.337 ± 0.034 |
| J123602.42+664445.21 | 18.01 | 18.181 | 18.108 ± 0.076 | 18.333 ± 0.057 |
| J123647.46+560438.86 | 17.038 | 17.435 | 17.190 ± 0.034 | 17.45 ± 0.025 |
| J123723.82+051009.00 | 16.467 | 16.983 | 16.809 ± 0.031 | 17.282 ± 0.024 |
| J123846.73+170620.80 | 15.647 | 16.207 | 15.853 ± 0.026 | 16.490 ± 0.022 |
| J123925.55+450803.32 | 18.613 | 18.704 | 18.918 ± 0.118 | 19.057 ± 0.089 |
| J124038.83+152859.99 | 16.584 | 17.016 | 16.763 ± 0.041 | 17.187 ± 0.029 |
| J124337.74+302921.40 | 16.532 | 16.969 | 16.620 ± 0.023 | 16.994 ± 0.015 |
| J124352.76+083616.52 | 18.026 | 18.127 | 18.318 ± 0.078 | 18.388 ± 0.042 |
| J124407.67+582351.90 | 15.275 | 15.834 | 15.434 ± 0.020 | 15.961 ± 0.009 |
| J124435.66−075304.70 | 17.115 | 17.457 | 17.373 ± 0.036 | 17.650 ± 0.028 |
| J124506.95+601019.30 | 14.106 | 14.812 | 14.047 ± 0.012 | 14.659 ± 0.009 |
| J124838.42+681327.48 | 18.043 | 18.22 | 18.244 ± 0.086 | 18.385 ± 0.059 |
| J124915.21+062052.94 | 15.784 | 16.362 | 16.001 ± 0.033 | 16.479 ± 0.013 |
| J125400.30+581948.15 | 15.878 | 16.451 | 16.014 ± 0.027 | 16.505 ± 0.011 |
| J125706.73+613507.95 | 17.162 | 17.569 | 17.565 ± 0.037 | 17.833 ± 0.018 |
| J125721.07+192451.70 | 15.193 | 15.781 | 15.372 ± 0.020 | 15.918 ± 0.011 |
| J125726.90+065834.70 | 16.329 | 16.795 | 16.646 ± 0.043 | 17.114 ± 0.017 |
| J125943.88+680400.91 | 15.1 | 15.66 | 15.412 ± 0.024 | 15.880 ± 0.019 |
| J130033.76+661600.83 | 14.559 | 15.116 | 14.690 ± 0.013 | 15.229 ± 0.011 |
| J130052.13+192931.70 | 14.672 | 15.265 | 14.974 ± 0.019 | 15.462 ± 0.009 |
| J130053.20+603628.50 | 18.891 | 18.936 | 19.113 ± 0.089 | 19.024 ± 0.043 |
| J130215.21−000111.53 | 18.189 | 18.314 | 18.517 ± 0.052 | 18.490 ± 0.030 |
| J130548.66+462135.55 | 16.742 | 17.23 | 16.876 ± 0.029 | 17.307 ± 0.024 |
| J130846.75+493000.80 | 15.995 | 16.552 | 16.247 ± 0.020 | 16.669 ± 0.014 |
| J130900.74−005434.30 | 17.284 | 17.576 | 17.624 ± 0.034 | 17.830 ± 0.023 |
| J131154.92+425451.70 | 17.409 | 17.738 | 17.579 ± 0.048 | 17.875 ± 0.028 |
| J131201.48+394827.90 | 17.993 | 17.996 | 18.393 ± 0.055 | 18.244 ± 0.038 |
| J131208.13+514159.52 | 16.657 | 17.09 | 16.800 ± 0.045 | 17.266 ± 0.023 |
| J131241.62+044609.05 | 18.01 | 18.19 | 18.555 ± 0.113 | 18.584 ± 0.058 |
| J131336.81+145910.68 | 18.016 | 18.243 | 18.475 ± 0.089 | 18.466 ± 0.062 |
| J131447.40+022558.30 | 17.321 | 17.647 | 17.730 ± 0.058 | 17.943 ± 0.043 |
| J131454.53+525831.04 | 17.082 | 17.491 | 17.271 ± 0.047 | 17.676 ± 0.030 |
| J131639.94+582651.51 | 18.042 | 18.212 | 18.310 ± 0.093 | 18.402 ± 0.039 |
| J131730.94+041752.04 | 16.619 | 17.133 | 16.792 ± 0.042 | 17.377 ± 0.036 |

Table 2.B.1 (cont'd)

| Star | Synthetic FUV mag | Synthetic NUV mag | Observed FUV mag | Observed NUV mag |
|---|---|---|---|---|
| J131737.68+102346.14 | 17.573 | 17.842 | 17.729 ± 0.045 | 17.969 ± 0.032 |
| J131926.96+425923.09 | 16.766 | 17.288 | 17.092 ± 0.032 | 17.591 ± 0.026 |
| J131930.11+241020.46 | 17.167 | 17.485 | 17.483 ± 0.051 | 17.647 ± 0.022 |
| J132010.48+340249.90 | 16.238 | 16.795 | 16.369 ± 0.031 | 16.912 ± 0.025 |
| J132033.41+303522.71 | 17.265 | 17.649 | 17.400 ± 0.071 | 17.766 ± 0.040 |
| WD1320+645 | 14.845 | 15.359 | 15.007 ± 0.010 | 15.469 ± 0.006 |
| J132324.13+293834.28 | 17.762 | 17.944 | 17.847 ± 0.064 | 18.040 ± 0.045 |
| J132329.25+294622.57 | 17.052 | 17.379 | 17.202 ± 0.048 | 17.564 ± 0.036 |
| J132331.18+105742.98 | 17.216 | 17.619 | 17.631 ± 0.071 | 17.866 ± 0.044 |
| J132336.77+373711.68 | 18.536 | 18.63 | 18.526 ± 0.068 | 18.681 ± 0.044 |
| J132537.21+012926.30 | 18.122 | 18.325 | 18.322 ± 0.080 | 18.553 ± 0.064 |
| J132603.42+632706.86 | 16.878 | 17.434 | 17.255 ± 0.049 | 17.751 ± 0.020 |
| J132615.83+170017.35 | 17.665 | 17.905 | 17.858 ± 0.063 | 18.050 ± 0.029 |
| J132709.96+385723.69 | 17.208 | 17.474 | 17.216 ± 0.032 | 17.479 ± 0.021 |
| J132747.10+303303.01 | 17.738 | 18.06 | 18.211 ± 0.081 | 18.267 ± 0.053 |
| J132918.24+282324.25 | 17.18 | 17.566 | 17.247 ± 0.041 | 17.644 ± 0.029 |
| J133137.06+010632.10 | 15.66 | 16.228 | 15.922 ± 0.027 | 16.431 ± 0.021 |
| J133137.57+184354.40 | 15.084 | 15.644 | 15.181 ± 0.020 | 15.733 ± 0.015 |
| J133154.09+354503.85 | 15.293 | 15.875 | 15.666 ± 0.031 | 16.069 ± 0.018 |
| J133154.14+004119.57 | 15.939 | 16.516 | 16.288 ± 0.031 | 16.773 ± 0.027 |
| J133207.33+665453.40 | 15.41 | 15.951 | 15.726 ± 0.029 | 16.110 ± 0.021 |
| J133507.26+432923.97 | 17.457 | 17.683 | 17.521 ± 0.068 | 17.765 ± 0.043 |
| WD1333+510 | 15.169 | 15.726 | 15.334 ± 0.025 | 15.785 ± 0.017 |
| J133620.80+352325.10 | 15.045 | 15.733 | 15.256 ± 0.021 | 15.755 ± 0.015 |
| J133631.48+200422.37 | 15.933 | 16.374 | 16.238 ± 0.032 | 16.532 ± 0.018 |
| J133739.67+455833.25 | 16.493 | 17.023 | 16.588 ± 0.033 | 17.087 ± 0.027 |
| J133756.50+081312.00 | 17.131 | 17.527 | 17.580 ± 0.053 | 17.928 ± 0.044 |
| J133824.21+115430.40 | 15.576 | 16.143 | 15.841 ± 0.032 | 16.408 ± 0.016 |
| J134142.53+661707.40 | 17.116 | 17.587 | 17.400 ± 0.057 | 17.784 ± 0.044 |
| J134259.84+022209.62 | 16.988 | 17.227 | 17.359 ± 0.055 | 17.511 ± 0.036 |
| J134422.63+271009.80 | 16.005 | 16.546 | 16.339 ± 0.036 | 16.765 ± 0.026 |
| J134437.93+113340.40 | 16.559 | 17.02 | 16.986 ± 0.053 | 17.276 ± 0.023 |
| J134501.72+151008.40 | 16.475 | 16.984 | 16.833 ± 0.041 | 17.250 ± 0.022 |
| J134540.19+165611.30 | 15.884 | 16.426 | 16.14 ± 0.030 | 16.587 ± 0.016 |
| J134739.43+265509.80 | 17.179 | 17.579 | 17.415 ± 0.064 | 17.805 ± 0.023 |
| J134847.01+065124.90 | 15.656 | 16.167 | 15.994 ± 0.022 | 16.385 ± 0.012 |

Table 2.B.1 (cont'd)

| Star | Synthetic FUV mag | Synthetic NUV mag | Observed FUV mag | Observed NUV mag |
|---|---|---|---|---|
| J134914.30+344241.72 | 17.731 | 17.982 | 17.893 ± 0.085 | 18.202 ± 0.061 |
| J134920.68+273508.40 | 15.425 | 15.98 | 15.767 ± 0.025 | 16.146 ± 0.010 |
| J135425.59+253508.59 | 16.119 | 16.551 | 16.408 ± 0.039 | 16.789 ± 0.020 |
| J135451.44+253047.92 | 15.495 | 16.053 | 15.685 ± 0.027 | 16.221 ± 0.022 |
| J135618.81+150847.94 | 18.241 | 18.359 | 18.842 ± 0.102 | 18.584 ± 0.041 |
| J135647.65+014448.30 | 17.657 | 17.778 | 17.931 ± 0.067 | 18.023 ± 0.047 |
| J135733.28+060757.90 | 16.794 | 17.225 | 17.126 ± 0.045 | 17.552 ± 0.036 |
| J135734.71+280111.35 | 15.267 | 15.817 | 15.569 ± 0.031 | 16.006 ± 0.024 |
| J135911.25+380659.04 | 17.339 | 17.629 | 17.438 ± 0.046 | 17.755 ± 0.031 |
| J135942.49+310255.52 | 16.613 | 16.982 | 16.727 ± 0.040 | 17.149 ± 0.022 |
| J135955.80+041113.24 | 17.933 | 18.102 | 18.441 ± 0.063 | 18.335 ± 0.031 |
| J140008.90+145246.99 | 15.181 | 15.748 | 15.408 ± 0.019 | 15.852 ± 0.013 |
| J140020.94+622809.47 | 16.932 | 17.276 | 17.079 ± 0.046 | 17.488 ± 0.036 |
| J140159.50+163551.32 | 18.014 | 18.252 | 18.302 ± 0.076 | 18.436 ± 0.038 |
| J140308.28+113255.43 | 16.091 | 16.559 | 16.338 ± 0.032 | 16.725 ± 0.017 |
| J140327.76+002119.60 | 14.799 | 15.488 | 15.165 ± 0.024 | 15.680 ± 0.008 |
| J140350.78+321859.80 | 15.44 | 16.003 | 15.644 ± 0.026 | 16.140 ± 0.020 |
| J140402.74+363916.80 | 17.9 | 18.247 | 18.311 ± 0.131 | 18.656 ± 0.082 |
| J140542.26+241243.20 | 17.114 | 17.507 | 17.596 ± 0.058 | 17.830 ± 0.025 |
| J140623.02+273103.32 | 16.143 | 16.701 | 16.345 ± 0.047 | 16.840 ± 0.018 |
| J140623.68+140529.26 | 17.098 | 17.36 | 17.360 ± 0.053 | 17.534 ± 0.027 |
| J140642.21+363755.20 | 15.86 | 16.397 | 16.073 ± 0.041 | 16.525 ± 0.015 |
| J140857.39+415213.80 | 15.572 | 16.124 | 15.789 ± 0.022 | 16.288 ± 0.020 |
| J140949.89+362005.20 | 18.696 | 18.761 | 18.986 ± 0.157 | 18.943 ± 0.052 |
| J141106.09+240208.59 | 16.528 | 16.944 | 17.054 ± 0.053 | 17.309 ± 0.021 |
| J141229.65+590112.90 | 15.099 | 15.705 | 15.297 ± 0.019 | 15.777 ± 0.011 |
| J141335.29+373907.20 | 19.206 | 19.079 | 19.466 ± 0.123 | 19.086 ± 0.070 |
| J141340.17+371323.00 | 18.071 | 18.254 | 18.239 ± 0.105 | 18.378 ± 0.064 |
| J141414.09+265346.60 | 16.293 | 16.789 | 16.322 ± 0.039 | 16.726 ± 0.030 |
| J141631.38+274815.37 | 17.915 | 18.204 | 17.957 ± 0.094 | 18.360 ± 0.071 |
| J141941.60+032244.08 | 18.356 | 18.487 | 18.783 ± 0.064 | 18.686 ± 0.035 |
| J142113.03+274018.34 | 17.683 | 17.926 | 18.008 ± 0.097 | 18.109 ± 0.067 |
| J142328.99+461106.20 | 17.748 | 18.071 | 17.904 ± 0.067 | 18.264 ± 0.054 |
| J142509.50+461348.00 | 18.489 | 18.554 | 18.819 ± 0.098 | 18.846 ± 0.069 |
| J142621.00+040009.86 | 18.019 | 18.177 | 18.275 ± 0.089 | 18.390 ± 0.040 |
| J142752.24+145740.40 | 17.391 | 17.614 | 17.691 ± 0.066 | 17.718 ± 0.041 |

Table 2.B.1 (cont'd)

| Star | Synthetic FUV mag | Synthetic NUV mag | Observed FUV mag | Observed NUV mag |
|---|---|---|---|---|
| WD1427+410 | 15.516 | 16.087 | 15.834 ± 0.028 | 16.248 ± 0.021 |
| J143315.92+252853.10 | 15.646 | 16.091 | 15.995 ± 0.043 | 16.370 ± 0.032 |
| J143345.68+311609.30 | 16.86 | 17.266 | 16.890 ± 0.053 | 17.336 ± 0.035 |
| J143616.49+465547.10 | 17.561 | 17.883 | 17.667 ± 0.062 | 17.964 ± 0.046 |
| J143801.04+010738.30 | 16.298 | 16.773 | 16.660 ± 0.023 | 17.142 ± 0.017 |
| J143801.04+010738.30 | 16.298 | 16.773 | 16.660 ± 0.023 | 17.142 ± 0.017 |
| J143812.99+123252.87 | 17.919 | 18.091 | 18.116 ± 0.079 | 18.266 ± 0.055 |
| J143831.47+292319.40 | 16.564 | 17.061 | 16.742 ± 0.039 | 17.252 ± 0.034 |
| J143901.42+113839.40 | 16.527 | 16.953 | 16.904 ± 0.044 | 17.251 ± 0.034 |
| J143906.08−005102.56 | 17.423 | 17.751 | 17.971 ± 0.077 | 18.199 ± 0.048 |
| J144208.86−002737.00 | 16.309 | 16.837 | 16.710 ± 0.035 | 17.152 ± 0.028 |
| J144307.67+605111.20 | 17.221 | 17.533 | 17.437 ± 0.043 | 17.673 ± 0.026 |
| J144711.77+140649.10 | 18.676 | 18.427 | 18.949 ± 0.110 | 18.735 ± 0.069 |
| J144801.75+471500.55 | 17.614 | 17.977 | 18.012 ± 0.061 | 18.365 ± 0.044 |
| J144823.68+444344.40 | 16.787 | 17.011 | 17.098 ± 0.036 | 17.230 ± 0.024 |
| J145024.57+123840.85 | 17.443 | 17.721 | 17.728 ± 0.078 | 17.960 ± 0.052 |
| J145101.86+620349.40 | 16.286 | 16.778 | 16.469 ± 0.037 | 16.962 ± 0.027 |
| J145104.16+371541.87 | 18.163 | 18.352 | 18.567 ± 0.071 | 18.424 ± 0.043 |
| J145350.14+234928.67 | 17.453 | 17.796 | 17.881 ± 0.081 | 18.197 ± 0.056 |
| J145420.83+223658.18 | 16.727 | 17.192 | 17.323 ± 0.068 | 17.561 ± 0.051 |
| J145726.29+364340.60 | 15.197 | 15.764 | 15.460 ± 0.016 | 15.939 ± 0.010 |
| J145734.43+334952.20 | 16.456 | 16.975 | 16.776 ± 0.039 | 17.185 ± 0.018 |
| J145802.94+411723.75 | 17.923 | 18.225 | 18.161 ± 0.075 | 18.358 ± 0.047 |
| J145913.99+041146.50 | 16.798 | 17.194 | 17.202 ± 0.035 | 17.499 ± 0.025 |
| J150050.71+040430.00 | 16.369 | 16.882 | 16.801 ± 0.031 | 17.248 ± 0.023 |
| J150153.77+020304.14 | 17.012 | 17.357 | 17.428 ± 0.049 | 17.767 ± 0.034 |
| J150204.71+423729.50 | 17.884 | 18.084 | 17.928 ± 0.053 | 18.031 ± 0.033 |
| J150445.84+111641.09 | 17.199 | 17.478 | 17.651 ± 0.072 | 17.794 ± 0.049 |
| J150501.20+074416.40 | 17.215 | 17.667 | 17.638 ± 0.076 | 17.925 ± 0.045 |
| J150602.91+360731.58 | 17.925 | 18.19 | 18.186 ± 0.063 | 18.380 ± 0.039 |
| J150820.73+524159.00 | 18.199 | 18.29 | 18.510 ± 0.056 | 18.434 ± 0.037 |
| J150918.45+340044.60 | 16.597 | 16.976 | 16.945 ± 0.040 | 17.234 ± 0.025 |
| J150928.51+462321.10 | 15.86 | 16.405 | 16.178 ± 0.025 | 16.616 ± 0.019 |
| J150949.52+565002.08 | 17.848 | 18.068 | 18.121 ± 0.098 | 18.297 ± 0.054 |
| J151139.63+453631.97 | 17.973 | 18.161 | 18.283 ± 0.069 | 18.399 ± 0.042 |
| J151234.03+165832.88 | 16.39 | 16.913 | 16.671 ± 0.033 | 17.171 ± 0.027 |

Table 2.B.1 (cont'd)

| Star | Synthetic FUV mag | Synthetic NUV mag | Observed FUV mag | Observed NUV mag |
|---|---|---|---|---|
| J151343.51+443436.30 | 16.052 | 16.492 | 16.216 ± 0.021 | 16.613 ± 0.012 |
| J151531.23+340058.00 | 17.61 | 17.817 | 18.141 ± 0.079 | 18.151 ± 0.030 |
| J151616.34+374912.06 | 17.147 | 17.513 | 17.436 ± 0.042 | 17.667 ± 0.027 |
| J151622.01+355945.17 | 18.119 | 18.292 | 18.541 ± 0.081 | 18.537 ± 0.039 |
| J151638.14+341201.20 | 16.894 | 17.394 | 17.365 ± 0.048 | 17.713 ± 0.026 |
| J151732.48+425340.49 | 16.341 | 16.805 | 16.765 ± 0.035 | 17.071 ± 0.025 |
| J151817.26+581923.20 | 16.733 | 17.105 | 16.907 ± 0.024 | 17.201 ± 0.021 |
| J151949.00+190504.60 | 17.903 | 18.188 | 18.616 ± 0.081 | 18.874 ± 0.055 |
| J152001.71+423855.00 | 16.952 | 17.428 | 17.416 ± 0.042 | 17.784 ± 0.034 |
| J152035.38+235036.96 | 16.797 | 17.23 | 17.052 ± 0.057 | 17.564 ± 0.039 |
| J152138.67+053333.98 | 16.903 | 17.257 | 17.152 ± 0.039 | 17.565 ± 0.033 |
| J152139.00+103015.80 | 14.261 | 14.887 | 14.756 ± 0.011 | 15.236 ± 0.009 |
| J152354.80+053941.30 | 16.566 | 16.968 | 16.988 ± 0.040 | 17.261 ± 0.027 |
| J152408.24+550048.99 | 16.557 | 17.077 | 16.826 ± 0.052 | 17.206 ± 0.032 |
| J152421.85+391952.40 | 17.122 | 17.506 | 17.446 ± 0.051 | 17.749 ± 0.028 |
| J152447.44+493448.00 | 17.684 | 17.928 | 18.025 ± 0.075 | 18.090 ± 0.046 |
| J152643.13+063149.94 | 16.571 | 17.046 | 16.934 ± 0.054 | 17.259 ± 0.033 |
| J152724.61+070128.56 | 16.656 | 17.165 | 17.073 ± 0.054 | 17.561 ± 0.037 |
| J152759.13+012406.19 | 14.903 | 15.464 | 15.236 ± 0.024 | 15.782 ± 0.017 |
| J152800.53+361510.81 | 17.535 | 17.806 | 17.709 ± 0.057 | 17.984 ± 0.035 |
| J152907.43+445330.66 | 16.832 | 17.243 | 17.169 ± 0.039 | 17.431 ± 0.029 |
| J152957.97+573200.08 | 16.991 | 17.387 | 17.207 ± 0.050 | 17.467 ± 0.037 |
| J153103.51+505133.00 | 17.038 | 17.499 | 17.322 ± 0.032 | 17.650 ± 0.025 |
| J153331.97+383824.38 | 17.962 | 18.165 | 18.055 ± 0.051 | 18.258 ± 0.038 |
| J153437.70−004719.30 | 15.775 | 16.315 | 16.419 ± 0.034 | 17.090 ± 0.019 |
| J153647.76+081826.57 | 18.116 | 18.293 | 18.438 ± 0.078 | 18.679 ± 0.066 |
| J153716.29+584802.73 | 18.234 | 18.368 | 18.288 ± 0.063 | 18.486 ± 0.044 |
| J153931.54+000118.40 | 16.34 | 16.853 | 16.968 ± 0.032 | 17.448 ± 0.026 |
| J154113.97+560843.54 | 17.608 | 17.962 | 18.034 ± 0.074 | 18.323 ± 0.054 |
| J154254.21+061228.60 | 16.03 | 16.499 | 16.355 ± 0.023 | 16.836 ± 0.019 |
| J154318.28+492240.70 | 15.368 | 15.943 | 15.714 ± 0.023 | 16.168 ± 0.012 |
| J154406.51+384757.65 | 17.77 | 17.966 | 18.069 ± 0.055 | 18.176 ± 0.037 |
| J154448.26+455039.10 | 15.399 | 15.99 | 15.576 ± 0.017 | 16.084 ± 0.012 |
| J154456.80+451522.00 | 13.998 | 14.706 | 13.993 ± 0.011 | 14.708 ± 0.009 |
| J154456.81+422620.70 | 16.813 | 17.297 | 17.042 ± 0.050 | 17.445 ± 0.035 |
| J154601.39+021050.92 | 16.686 | 17.205 | 17.533 ± 0.055 | 18.066 ± 0.047 |

Table 2.B.1 (cont'd)

| Star | Synthetic FUV mag | Synthetic NUV mag | Observed FUV mag | Observed NUV mag |
|---|---|---|---|---|
| J154640.62+334644.47 | 18.295 | 18.531 | 18.5 ± 0.051 | 18.841 ± 0.048 |
| J154724.19+065522.80 | 17.237 | 17.637 | 17.673 ± 0.042 | 17.918 ± 0.033 |
| J154746.78+245055.30 | 16.037 | 16.544 | 16.515 ± 0.030 | 16.952 ± 0.022 |
| J154912.51+292338.80 | 18.229 | 18.46 | 18.542 ± 0.094 | 18.766 ± 0.033 |
| J154922.17+334601.10 | 16.236 | 16.804 | 16.569 ± 0.033 | 17.088 ± 0.027 |
| J154950.00+205043.40 | 15.273 | 15.836 | 15.781 ± 0.020 | 16.275 ± 0.012 |
| J154950.06+215753.57 | 17.565 | 17.809 | 18.004 ± 0.068 | 18.233 ± 0.040 |
| J155035.21+402558.60 | 13.712 | 14.326 | 14.015 ± 0.010 | 14.454 ± 0.008 |
| J155108.25+454313.22 | 15.702 | 16.298 | 15.959 ± 0.022 | 16.436 ± 0.010 |
| J155512.50+074554.22 | 17.245 | 17.586 | 17.442 ± 0.037 | 17.827 ± 0.022 |
| J155552.40+172920.04 | 15.595 | 16.194 | 16.088 ± 0.020 | 16.597 ± 0.017 |
| J155559.89+172008.23 | 17.201 | 17.547 | 17.655 ± 0.045 | 17.858 ± 0.031 |
| J155920.38+264454.10 | 18.756 | 18.749 | 19.353 ± 0.162 | 19.113 ± 0.070 |
| J160135.34+361439.80 | 16.976 | 17.325 | 17.264 ± 0.047 | 17.658 ± 0.036 |
| J160215.04+491314.00 | 16.048 | 16.547 | 16.381 ± 0.025 | 16.757 ± 0.020 |
| J160317.78+413308.96 | 16.74 | 17.252 | 16.955 ± 0.037 | 17.328 ± 0.017 |
| J160442.26+032827.10 | 17.814 | 18.008 | 18.306 ± 0.080 | 18.607 ± 0.042 |
| J160515.39+503137.96 | 17.112 | 17.35 | 17.114 ± 0.041 | 17.400 ± 0.023 |
| J160550.54+060738.10 | 14.65 | 15.271 | 15.346 ± 0.020 | 15.780 ± 0.016 |
| J160614.05+204253.80 | 16.77 | 17.1 | 17.466 ± 0.051 | 17.830 ± 0.024 |
| J160631.60+250651.10 | 16.172 | 16.609 | 16.497 ± 0.028 | 17.030 ± 0.014 |
| J160647.63+050605.00 | 17.379 | 17.756 | 17.905 ± 0.069 | 18.158 ± 0.051 |
| J160647.64+050605.00 | 17.379 | 17.756 | 17.905 ± 0.069 | 18.158 ± 0.051 |
| J160710.27+511829.20 | 16.826 | 17.331 | 17.179 ± 0.040 | 17.547 ± 0.025 |
| J160905.16+285104.75 | 18.124 | 18.278 | 18.504 ± 0.095 | 18.581 ± 0.069 |
| J161018.32+054237.60 | 18.698 | 18.788 | 19.033 ± 0.084 | 19.135 ± 0.059 |
| J161117.52+401703.26 | 17.43 | 17.573 | 17.742 ± 0.081 | 17.608 ± 0.019 |
| J161205.78+543455.85 | 15.152 | 15.704 | 15.407 ± 0.017 | 15.880 ± 0.008 |
| J161226.56+425111.45 | 15.741 | 16.324 | 15.875 ± 0.021 | 16.373 ± 0.011 |
| J161239.12+091548.90 | 16.554 | 16.996 | 16.776 ± 0.034 | 17.263 ± 0.024 |
| J161333.44+103605.40 | 18.03 | 18.102 | 18.249 ± 0.071 | 18.484 ± 0.046 |
| J161409.82+425226.22 | 16.756 | 17.14 | 16.725 ± 0.033 | 17.170 ± 0.016 |
| J161432.10+185458.75 | 15.866 | 16.379 | 16.284 ± 0.041 | 16.758 ± 0.016 |
| J161441.99+370548.20 | 14.745 | 15.45 | 15.082 ± 0.017 | 15.474 ± 0.013 |
| J161500.81+034457.90 | 17.955 | 18.081 | 18.349 ± 0.060 | 18.507 ± 0.034 |
| J161505.25+295512.94 | 17.404 | 17.817 | 17.733 ± 0.064 | 18.130 ± 0.029 |

Table 2.B.1 (cont'd)

| Star | Synthetic FUV mag | Synthetic NUV mag | Observed FUV mag | Observed NUV mag |
|---|---|---|---|---|
| J161528.68+535152.54 | 18.101 | 18.362 | 18.374 ± 0.091 | 18.581 ± 0.031 |
| J161547.53+361121.52 | 17.872 | 18.195 | 18.104 ± 0.061 | 18.337 ± 0.049 |
| J161554.03+433840.42 | 17.994 | 18.247 | 18.171 ± 0.062 | 18.328 ± 0.029 |
| J161613.10+252012.70 | 15.808 | 16.398 | 16.765 ± 0.038 | 17.161 ± 0.016 |
| J161710.37+215413.50 | 18.454 | 18.525 | 19.215 ± 0.135 | 19.218 ± 0.062 |
| J161722.83+252756.70 | 16.753 | 17.248 | 17.620 ± 0.051 | 17.937 ± 0.024 |
| J161725.34+071838.27 | 17.791 | 18.044 | 18.214 ± 0.060 | 18.457 ± 0.042 |
| J161756.73+532254.41 | 17.517 | 17.794 | 17.801 ± 0.048 | 18.073 ± 0.039 |
| J161905.60+083333.40 | 16.551 | 16.986 | 17.055 ± 0.038 | 17.453 ± 0.020 |
| J161928.28+365403.20 | 18.324 | 18.524 | 18.510 ± 0.056 | 18.583 ± 0.038 |
| J161940.02+222958.30 | 14.661 | 15.212 | 15.251 ± 0.020 | 15.738 ± 0.015 |
| J162005.04+114943.40 | 15.279 | 15.844 | 15.727 ± 0.025 | 16.224 ± 0.012 |
| J162020.89+214542.98 | 15.808 | 16.291 | 16.163 ± 0.036 | 16.722 ± 0.025 |
| J162024.41−000545.90 | 16.519 | 16.832 | 17.005 ± 0.024 | 17.424 ± 0.020 |
| J162034.43+374347.35 | 17.367 | 17.665 | 17.678 ± 0.053 | 17.887 ± 0.023 |
| J162106.46+434126.90 | 16.079 | 16.602 | 16.229 ± 0.028 | 16.688 ± 0.023 |
| J162158.81+202402.09 | 17.021 | 17.489 | 17.556 ± 0.060 | 17.988 ± 0.032 |
| J162301.57+303040.18 | 17.382 | 17.637 | 17.742 ± 0.060 | 17.867 ± 0.025 |
| J162324.90−011123.80 | 17.511 | 17.714 | 17.792 ± 0.046 | 18.101 ± 0.036 |
| J162746.83+631839.60 | 16.206 | 16.691 | 16.443 ± 0.027 | 16.838 ± 0.023 |
| J162825.98+333450.60 | 16.321 | 16.822 | 16.702 ± 0.025 | 17.073 ± 0.023 |
| J162912.30+375952.66 | 17.881 | 18.092 | 17.981 ± 0.063 | 18.175 ± 0.043 |
| J163218.84+404618.90 | 16.847 | 17.356 | 17.069 ± 0.045 | 17.465 ± 0.024 |
| J163328.05+233346.40 | 16.279 | 16.761 | 16.791 ± 0.044 | 17.074 ± 0.018 |
| J163336.71+140629.30 | 18.222 | 18.415 | 18.744 ± 0.091 | 18.89 ± 0.061 |
| J163338.87+303041.90 | 17.755 | 18.015 | 18.165 ± 0.089 | 18.003 ± 0.047 |
| J163348.91+323616.34 | 18.532 | 18.623 | 18.647 ± 0.084 | 18.750 ± 0.047 |
| J163351.20+294504.43 | 16.902 | 17.411 | 17.39 ± 0.053 | 17.745 ± 0.021 |
| J163453.38+182758.90 | 18.783 | 18.814 | 19.158 ± 0.106 | 19.226 ± 0.049 |
| J163511.64+111849.90 | 16.125 | 16.692 | 16.805 ± 0.030 | 17.332 ± 0.018 |
| J163524.38+444349.80 | 17.289 | 17.801 | 17.698 ± 0.056 | 17.978 ± 0.043 |
| J163559.97+464154.75 | 18.46 | 18.631 | 18.602 ± 0.070 | 18.792 ± 0.039 |
| J163609.00+560135.00 | 16.753 | 17.247 | 17.094 ± 0.043 | 17.443 ± 0.030 |
| J163659.28+354519.80 | 17.537 | 17.864 | 17.731 ± 0.058 | 18.078 ± 0.045 |
| J163920.38+201638.75 | 17.573 | 17.956 | 18.195 ± 0.068 | 18.386 ± 0.047 |
| J163936.15+474312.36 | 17.368 | 17.587 | 17.377 ± 0.039 | 17.583 ± 0.024 |

Table 2.B.1 (cont'd)

| Star | Synthetic FUV mag | Synthetic NUV mag | Observed FUV mag | Observed NUV mag |
|---|---|---|---|---|
| J163939.51+480655.25 | 16.64 | 16.963 | 16.815 ± 0.037 | 17.140 ± 0.027 |
| J163944.64+383346.84 | 15.857 | 16.391 | 16.057 ± 0.026 | 16.492 ± 0.021 |
| J164205.63+405330.70 | 17.621 | 17.861 | 17.788 ± 0.060 | 17.953 ± 0.031 |
| J164224.69+231359.50 | 15.299 | 15.881 | 15.882 ± 0.022 | 16.404 ± 0.014 |
| J164250.03+303716.25 | 19.202 | 19.043 | 19.453 ± 0.151 | 19.257 ± 0.074 |
| J164255.17+393105.20 | 16.074 | 16.571 | 16.335 ± 0.029 | 16.716 ± 0.020 |
| J164311.10+425000.74 | 18.163 | 18.289 | 18.231 ± 0.090 | 18.356 ± 0.036 |
| J164407.41+303143.07 | 16.442 | 16.926 | 16.661 ± 0.041 | 17.096 ± 0.025 |
| J164418.87+384230.70 | 17.274 | 17.532 | 17.483 ± 0.052 | 17.661 ± 0.038 |
| J164424.24+382830.61 | 14.439 | 15.032 | 14.600 ± 0.013 | 15.108 ± 0.011 |
| J164448.07+293059.36 | 18.422 | 18.621 | 18.651 ± 0.099 | 18.893 ± 0.054 |
| J164631.11+445315.18 | 18.166 | 18.414 | 18.366 ± 0.078 | 18.518 ± 0.054 |
| J164741.53+195746.94 | 18.088 | 18.329 | 18.440 ± 0.067 | 18.814 ± 0.052 |
| J164812.58+331154.17 | 17.92 | 18.189 | 18.134 ± 0.075 | 18.284 ± 0.053 |
| J164936.08+263016.70 | 17.194 | 17.605 | 18.106 ± 0.069 | 18.214 ± 0.036 |
| J164936.63+450941.76 | 17.418 | 17.776 | 17.509 ± 0.075 | 17.828 ± 0.046 |
| J164947.18+262409.50 | 15.011 | 15.627 | 15.965 ± 0.017 | 16.421 ± 0.016 |
| J164950.07+312421.64 | 18.335 | 18.523 | 18.514 ± 0.082 | 18.703 ± 0.056 |
| J164952.57+222334.12 | 18.269 | 18.454 | 18.504 ± 0.075 | 18.711 ± 0.031 |
| J165128.84+633438.30 | 18.445 | 18.431 | 18.645 ± 0.072 | 18.546 ± 0.044 |
| J165148.75+261531.00 | 15.372 | 15.935 | 16.302 ± 0.021 | 16.626 ± 0.018 |
| J165228.26+232735.00 | 17.17 | 17.618 | 17.526 ± 0.061 | 18.000 ± 0.026 |
| J165249.28+384123.18 | 14.496 | 15.084 | 14.698 ± 0.014 | 15.242 ± 0.008 |
| J165337.76+181322.26 | 18.212 | 18.467 | 18.667 ± 0.093 | 18.926 ± 0.055 |
| J165424.17+171539.02 | 17.571 | 17.879 | 18.031 ± 0.055 | 18.445 ± 0.046 |
| J165449.68+402325.10 | 18.515 | 18.662 | 18.734 ± 0.106 | 18.834 ± 0.069 |
| J165534.64+123347.20 | 17.489 | 17.747 | 17.918 ± 0.052 | 18.154 ± 0.036 |
| J165657.05+403828.30 | 15.801 | 16.305 | 15.934 ± 0.026 | 16.401 ± 0.021 |
| WD1655+210 | 14.705 | 15.265 | 15.037 ± 0.018 | 15.558 ± 0.012 |
| J165812.62+382042.60 | 17.003 | 17.373 | 17.163 ± 0.048 | 17.472 ± 0.026 |
| J165817.76+291024.80 | 18.999 | 18.919 | 19.404 ± 0.213 | 19.167 ± 0.088 |
| J165818.04+404139.00 | 19.075 | 18.923 | 18.900 ± 0.108 | 18.808 ± 0.068 |
| J165826.66+363341.17 | 17.423 | 17.83 | 17.741 ± 0.058 | 18.079 ± 0.045 |
| J165828.47+445314.78 | 16.94 | 17.194 | 17.055 ± 0.056 | 17.293 ± 0.034 |
| J165851.11+341853.30 | 14.197 | 14.834 | 14.600 ± 0.011 | 15.006 ± 0.006 |
| J165929.07+263539.00 | 16.561 | 16.898 | 16.843 ± 0.033 | 17.118 ± 0.023 |

Table 2.B.1 (cont'd)

| Star | Synthetic FUV mag | Synthetic NUV mag | Observed FUV mag | Observed NUV mag |
|---|---|---|---|---|
| J165944.10+454557.74 | 15.612 | 16.242 | 15.782 ± 0.025 | 16.372 ± 0.023 |
| J170057.08+260359.80 | 17.564 | 17.898 | 17.943 ± 0.049 | 18.265 ± 0.038 |
| J170130.92+283028.30 | 17.756 | 17.979 | 18.055 ± 0.072 | 18.110 ± 0.049 |
| J170330.99+272850.80 | 16.106 | 16.65 | 16.616 ± 0.041 | 17.043 ± 0.031 |
| J170356.56+281323.20 | 17.134 | 17.442 | 17.664 ± 0.074 | 17.843 ± 0.042 |
| J170447.08+400458.80 | 17.624 | 17.992 | 17.823 ± 0.065 | 18.174 ± 0.034 |
| J170510.23+385357.40 | 16.989 | 17.441 | 17.267 ± 0.048 | 17.759 ± 0.042 |
| J170530.82+271523.30 | 15.168 | 15.793 | 15.746 ± 0.028 | 16.215 ± 0.017 |
| J170537.75+423346.48 | 16.073 | 16.437 | 16.118 ± 0.031 | 16.477 ± 0.018 |
| J170843.51+274921.00 | 16.497 | 17.039 | 17.638 ± 0.056 | 17.854 ± 0.039 |
| J170927.83+231020.70 | 17.774 | 17.844 | 18.092 ± 0.063 | 17.958 ± 0.041 |
| J171118.78+371021.70 | 17.25 | 17.651 | 17.371 ± 0.045 | 17.854 ± 0.041 |
| J171125.53+272405.15 | 15.198 | 15.814 | 15.776 ± 0.024 | 16.221 ± 0.020 |
| J171306.73+565525.60 | 17.118 | 17.465 | 17.410 ± 0.061 | 17.727 ± 0.045 |
| J171438.40+394539.40 | 18.05 | 18.337 | 18.377 ± 0.105 | 18.752 ± 0.068 |
| J171536.37+363040.32 | 17.715 | 17.911 | 17.850 ± 0.050 | 18.088 ± 0.039 |
| J172645.53+264227.30 | 17.388 | 17.712 | 17.674 ± 0.052 | 17.894 ± 0.037 |
| J173117.84+312302.04 | 18.357 | 18.564 | 18.765 ± 0.085 | 18.774 ± 0.061 |
| J173133.30+330804.30 | 18.271 | 18.44 | 18.566 ± 0.083 | 18.605 ± 0.037 |
| J173217.07+640716.90 | 16.573 | 17.056 | 16.808 ± 0.035 | 17.177 ± 0.025 |
| J173455.32+650823.50 | 16.318 | 16.877 | 16.679 ± 0.031 | 17.169 ± 0.025 |
| J173842.24+645534.30 | 15.902 | 16.453 | 16.208 ± 0.022 | 16.688 ± 0.018 |
| J181424.14+785403.00 | 14.787 | 15.35 | 15.127 ± 0.012 | 15.570 ± 0.011 |
| J192808.84+623438.10 | 18.241 | 18.368 | 18.269 ± 0.072 | 18.400 ± 0.053 |
| J193659.11+624921.40 | 17.623 | 17.929 | 17.875 ± 0.059 | 18.244 ± 0.047 |
| J202253.35+141153.10 | 15.084 | 15.745 | 15.801 ± 0.019 | 16.395 ± 0.016 |
| J204331.23+001119.90 | 17.112 | 17.461 | 17.506 ± 0.050 | 17.845 ± 0.037 |
| J204410.84+004515.30 | 17.077 | 17.484 | 17.346 ± 0.036 | 17.789 ± 0.029 |
| J204421.19−051856.00 | 18.424 | 18.482 | 18.537 ± 0.077 | 18.512 ± 0.048 |
| J204533.11+153307.70 | 16.731 | 17.06 | 17.210 ± 0.036 | 17.506 ± 0.030 |
| J205059.51+012146.90 | 15.973 | 16.495 | 16.348 ± 0.022 | 16.950 ± 0.016 |
| J205440.40+154816.50 | 15.903 | 16.468 | 16.389 ± 0.026 | 16.871 ± 0.023 |
| J210928.33−053843.20 | 15.403 | 15.97 | 16.145 ± 0.014 | 16.605 ± 0.012 |
| J211229.48−064051.80 | 15.699 | 16.208 | 16.262 ± 0.020 | 16.732 ± 0.017 |
| J211607.27+004503.17 | 17.735 | 18.082 | 20.175 ± 0.188 | 18.491 ± 0.055 |
| J212411.99−072648.70 | 15.644 | 16.331 | 14.224 ± 0.012 | 14.764 ± 0.008 |

Table 2.B.1 (cont'd)

| Star | Synthetic FUV mag | Synthetic NUV mag | Observed FUV mag | Observed NUV mag |
|---|---|---|---|---|
| J213225.88+005428.91 | 17.577 | 17.827 | $17.832 \pm 0.051$ | $18.125 \pm 0.037$ |
| J214903.12+054704.81 | 16.965 | 17.369 | $17.703 \pm 0.039$ | $18.150 \pm 0.033$ |
| J223405.82+232510.99 | 15.421 | 15.982 | $15.702 \pm 0.020$ | $16.277 \pm 0.015$ |
| J223558.35+133140.60 | 18.305 | 18.348 | $18.739 \pm 0.110$ | $18.618 \pm 0.065$ |
| J225247.41+270433.79 | 17.523 | 17.776 | $17.725 \pm 0.043$ | $18.052 \pm 0.031$ |
| J230255.02−084005.70 | 14.303 | 14.97 | $14.654 \pm 0.011$ | $15.233 \pm 0.010$ |
| J231340.86+063527.41 | 18.524 | 18.503 | $18.947 \pm 0.057$ | $19.094 \pm 0.042$ |
| J231640.19−010951.62 | 17.361 | 17.817 | $18.154 \pm 0.077$ | $18.405 \pm 0.058$ |
| J232230.96+152258.95 | 17.735 | 18.049 | $18.341 \pm 0.060$ | $18.505 \pm 0.042$ |
| J233157.66+144345.75 | 17.607 | 17.856 | $18.063 \pm 0.047$ | $18.308 \pm 0.030$ |
| WD2331+290 | 13.881 | 14.42 | $14.370 \pm 0.012$ | $14.837 \pm 0.004$ |
| J234528.67+394643.80 | 15.079 | 15.643 | $15.695 \pm 0.013$ | $16.236 \pm 0.013$ |
| J234733.92+440241.50 | 16.615 | 17.026 | $16.835 \pm 0.030$ | $17.267 \pm 0.023$ |
| J234738.64+423620.80 | 16.182 | 16.685 | $16.892 \pm 0.029$ | $17.302 \pm 0.023$ |
| J235148.35+362011.10 | 16.624 | 16.986 | $17.007 \pm 0.032$ | $17.391 \pm 0.026$ |
| J235315.25+153640.40 | 18.167 | 18.24 | $18.423 \pm 0.049$ | $18.510 \pm 0.025$ |
| J235353.61+355725.40 | 18.1 | 18.19 | $18.415 \pm 0.076$ | $18.558 \pm 0.047$ |

# CHAPTER 3

# A GALEX view of the DA White Dwarf Population

## 3.1. Introduction

Prior to *Gaia*, the majority of the white dwarfs in the solar neighborhood were identified through Sloan Digital Sky Survey spectroscopy, which specifically targeted hot and blue white dwarfs as flux standards (e.g., Kleinman et al., 2013). Many of the SDSS white dwarfs have spectral energy distributions that peak in the UV. Hence, GALEX FUV and NUV data can help constrain the physical parameters of these white dwarfs. GALEX data will also be useful for cooler white dwarfs; UV photometry will be used to confirm the temperature derived from the optical data, or to constrain the far red wing of the Lyman $\alpha$ line that dominates the opacity in the blue part of the spectral energy distribution of cool hydrogen atmosphere white dwarfs (Kowalski & Saumon, 2006). Yet, GALEX data are under-utilized in the analysis of white dwarfs in the literature, perhaps due to the relatively strong extinction observed in the UV.

Wall et al. (2019) used 1837 DA white dwarfs with high signal to noise ratio spectra and *Gaia* parallaxes to verify the absolute calibration of the FUV and NUV data, and refined the linearity corrections derived by Camarota & Holberg (2014). They also empirically derived extinction coefficients for both bands, finding $R_{\rm FUV} = 8.01$ and $R_{\rm NUV} = 6.72$, where $R$ is the ratio of the total absorption $A_\lambda$ to reddening $E(B-V)$ along the line of sight to an object. Wall et al. (2019) highlighted the utility of their newly derived extinction coefficients for identifying white dwarfs with unusual UV photometry. By comparing the observed GALEX magnitudes to predictions from the model atmosphere calculations, they found 12 outliers in the UV, seven of which were previously known, including three double degenerates, two white dwarf + main-sequence star binaries, one ZZ Ceti, and one double degenerate candidate (see chapter 2).

Lajoie & Bergeron (2007) compared the effective temperatures obtained from the optical and UV spectra of 140 DA white dwarfs from the *IUE* archive. They found that the optical and UV temperatures of the majority of stars cooler than 40000 K and within 75 pc are in fairly good agreement with $\Delta T_{\rm eff}/T_{\rm optical} \leq 10\%$. They also found that the majority of the discrepancies between the two temperature measurements were caused by interstellar reddening, which affects the UV more than the optical. By restricting their analysis to white dwarfs within 75 pc, where the extinction is negligible, they were able to identify several double degenerate candidates, as well as a DA + M dwarf system, and stars with unusual atmospheric compositions. Lajoie & Bergeron (2007) thus demonstrated that unusual white dwarfs can be identified by comparing temperatures

derived solely from optical data and UV data.

In this work, we expand the analysis of optical and UV temperature measurements to the DA white dwarfs in the Montreal White Dwarf Database (MWDD) aided by GALEX UV data and *Gaia* Data Release 3 astrometry. To identify unusual white dwarfs, we use two methods. First, we compare the UV and optical temperatures in a manner similar to Lajoie & Bergeron (2007). We refer to this as the temperature comparison method. Our second method follows the analysis of Wall et al. (2019) and compares the observed and predicted GALEX magnitudes. We refer to this as the magnitude comparison method.

We provide the details of our sample selection in Section 3.2, the model atmosphere fitting procedure in Section 3.3, and the results from the temperature comparison method for the 100 pc sample and the entire MWDD sample in Section 3.4. Section 3.5 presents the results from the magnitude comparison method. We conclude in Section 3.6.

### 3.2. Sample Selection

We started with all spectroscopically confirmed DA white dwarfs from the Montreal White Dwarf Database (Dufour et al., 2017) using the September 2022 version of the database. This sample includes over 30000 stars. We removed known white dwarf + main-sequence binaries and variables from the sample. We then collected the SDSS and Pan-STARRS1 photometry using the cross-match tables provided by *Gaia* DR3. We found 25840 DA white dwarfs with *Gaia* astrometry and Pan-STARRS1 photometry, 20898 of which are also detected in the SDSS.

*Gaia* DR3 does not provide a cross-matched catalog with GALEX, which performed its all-sky imaging survey between 2003 and 2009. The reference epoch for the *Gaia* DR3 positions is 2016. Assuming a 10 year baseline between the GALEX mission and *Gaia* DR3, we propagated the *Gaia* DR3 positions to the GALEX epoch using *Gaia* proper motions. We then cross-referenced our sample with the GALEX catalogue of unique UV sources from the all-sky imaging survey (GUVcat) presented in Bianchi et al. (2017). We used a cross-match radius of 3 arcseconds with GUVcat. We found 18456 DA white dwarfs with GALEX data.

Some of the DA white dwarfs in our sample are bright enough to be saturated in Pan-STARRS, SDSS, or GALEX. The saturation occurs at $g, r, i \sim 13.5$, $z \sim 13$, and $y \sim 12$ mag in Pan-STARRS (Magnier et al., 2013). We remove objects brighter than these limits. To make sure that there are at least three optical filters available for our model fits, we limit our sample to objects with at least Pan-STARRS $g, r, i$ photometry available.

We apply the linearity corrections for the GALEX FUV and NUV bands as measured by Wall et al. (2019). These corrections are $\geq 0.5$ mag for FUV and NUV magnitudes brighter than 13th mag. To avoid issues with saturation and large linearity corrections in the GALEX bands, we further remove objects with FUV and NUV magnitudes brighter than that limit. We further limit our sample

to objects with a $3\sigma$ significant distance measurement (Bailer-Jones et al., 2021) so that we can reliably constrain the radii (and therefore mass and surface gravity) of the stars in our sample. Our final sample contains 14001 DA white dwarfs with photometry in at least one of the GALEX filters and the Pan-STARRS $gri$ filters. However, more than half of the stars in our final selection, 7574 of them, have GALEX FUV, NUV, SDSS $u$, and Pan-STARRS $gri(zy)$ photometry available.

### 3.3. The Fitting Procedure

We use the photometric technique as detailed in Bergeron et al. (2019), and perform two sets of fits; 1) using only the optical data, and 2) using both the optical and the UV data. In the first set of fits we use the SDSS $u$ (if available) along with the Pan-STARRS $grizy$ photometry to model the spectral energy distribution of each DA white dwarf, and in the second set of fits we add the GALEX FUV (if available) and NUV data.

We correct the SDSS $u$ magnitude to the AB magnitude system using the corrections provided by Eisenstein et al. (2006). For the reasons outlined in Bergeron et al. (2019), we adopt a lower limit of 0.03 mag uncertainty in all bandpasses, and use the de-reddening procedure outlined in Harris et al. (2006) where the extinction is assumed to be zero for stars within 100 pc, to be maximum for those located at distances 250 pc away from the Galactic plane, and to vary linearly along the line of sight between these two regimes.

We convert the observed magnitudes into average fluxes using the appropriate zero points, and compare with the average synthetic fluxes calculated from pure hydrogen atmosphere models. We define a $\chi^2$ value in terms of the difference between observed and model fluxes over all bandpasses, properly weighted by the photometric uncertainties, which is then minimized using the nonlinear least-squares method of Levenberg-Marquardt (Press et al., 1986) to obtain the best fitting parameters. We obtain the uncertainties of each fitted parameter directly from the covariance matrix of the fitting algorithm, while we calculate the uncertainties for all other quantities derived from these parameters by propagating in quadrature the appropriate measurement errors.

We fit for the effective temperature and the solid angle, $\pi(R/D)^2$, where $R$ is the radius of the star and $D$ is its distance. Since the distance is known from *Gaia* parallaxes, we constrain the radius of the star directly, and therefore the mass based on the evolutionary models for white dwarfs. The details of our fitting method, including the model grids used are further discussed in Bergeron et al. (2019) and Genest-Beaulieu & Bergeron (2019).

### 3.4. Results from Temperature Comparison

#### 3.4.1. The 100 pc SDSS Sample

We use the 100 pc white dwarf sample in the SDSS footprint to test if the temperatures obtained from the optical and the UV data agree, and also to test the feasibility of identifying UV-excess or

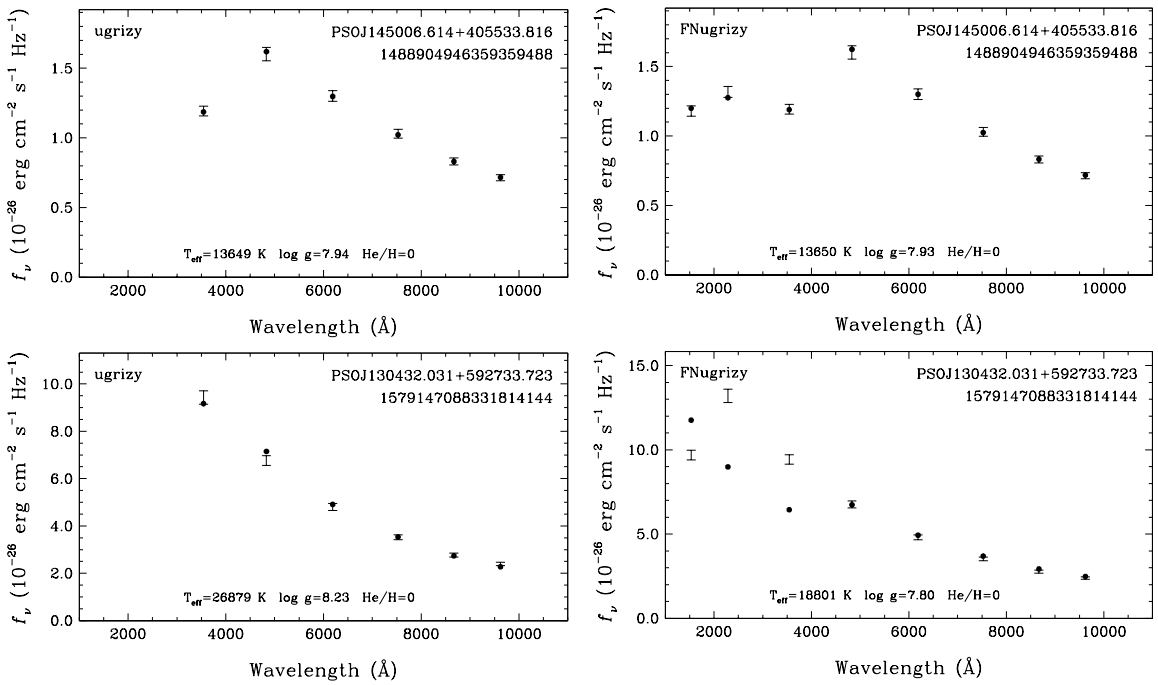


**Figure 3.4.1:** *Top:* Model fits to WD 1448+411, a spectroscopically confirmed DA white dwarf in the 100 pc SDSS sample. Each panel shows the best-fitting pure hydrogen atmosphere white dwarf model (filled dots) to the photometry (error bars). The labels in each panel include the Pan-STARRS coordinates, the *Gaia* DR3 Source ID, and the photometry used in the fitting: $FNugrizy$ means GALEX FUV + NUV + SDSS $u$ + Pan-STARRS $grizy$. The left panel shows the model fits based on the optical data only, whereas the right panel shows the fit using both optical and the UV data. The best-fitting model parameters are given in each panel. *Bottom:* Model fits to GD 323 (WD 1302+597), a spectroscopically confirmed DAB white dwarf, assuming a pure H atmosphere.

UV-deficit objects. Kilic et al. (2020) presented a detailed model atmosphere analysis of the 100 pc white dwarf sample in the SDSS footprint and identified 1508 DA white dwarfs. Cross-matching this sample with GUVcat (Bianchi et al., 2017), we find 847 DA white dwarfs with GALEX data; 377 have both FUV and NUV photometry available, while 470 have only NUV data available.

The top panels in Figure 3.4.1 show our fits for WD 1448+411, a spectroscopically confirmed DA white dwarf (Gianninas et al., 2011) in the 100 pc SDSS sample. The top left panel shows the SDSS $u$ and Pan-STARRS $grizy$ photometry (error bars) along with the predicted fluxes from the best-fitting pure hydrogen atmosphere model (filled dots). The labels in the same panel give the Pan-STARRS coordinates, *Gaia* DR3 Source ID, and the photometry used in the fitting. The top right panel shows the same model fits, but with the addition of the GALEX FUV and NUV photometry. The temperature and surface gravity estimates from both sets of fits, based on either the optical data only (left panel) or a combination of the optical and UV data (right panel), agree remarkably well for this star. Hence, the spectral energy distribution of WD 1448+411 in the 0.1-1 $\mu$m range is consistent with an isolated pure hydrogen atmosphere white dwarf.

The bottom panels in Figure 3.4.1 show the model fits for another white dwarf in the 100 pc SDSS sample. GD 323 (WD 1302+597) is a spectroscopically confirmed DAB white dwarf (Wesemael et al., 1993). The use of pure hydrogen atmosphere models to fit its spectral energy distribution is obviously inappropriate. However, we use GD 323 to demonstrate how fitting the UV to optical spectral energy distribution can reveal object with unusual atmospheric composition. The bottom left panel in Figure 3.4.1 shows our model fits using only the optical data from the SDSS and Pan-STARRS. Assuming a pure hydrogen composition, GD 323 would have the best-fitting $T_{\rm eff} = 26879 \pm 1310$ K and $\log g = 8.230 \pm 0.047$. This solution provides an excellent match to the optical photometry. The bottom right panel shows the same model fits with the addition of the GALEX FUV and NUV data. The best-fitting model parameters are significantly different, and clearly the pure hydrogen atmosphere models cannot match the UV portion of the spectral energy distribution of GD 323. Hence, a comparison between the two sets of model fits based on optical and/or UV data has the potential to identify DAB or other types of unusual objects among the DA white dwarf population in the solar neighborhood.

Figure 3.4.2 shows a comparison between the model fits using optical data only versus a combination of the optical + UV data for the DA white dwarfs in the 100 pc SDSS sample. Blue dots and red triangles mark the magnetic and DAB white dwarfs, respectively. The majority of the objects in this figure fall very close to the 1:1 line, shown in red, confirming that they are consistent with pure hydrogen atmosphere white dwarfs.

Excluding the five significant outliers labeled in the figure, the effective temperature and $\log g$ derived from the GALEX+optical data are slightly higher than the values obtained from the optical data only by $50^{+215}_{-71}$ K and $0.01^{+0.04}_{-0.01}$ dex, respectively. Hence, there are no major systematic

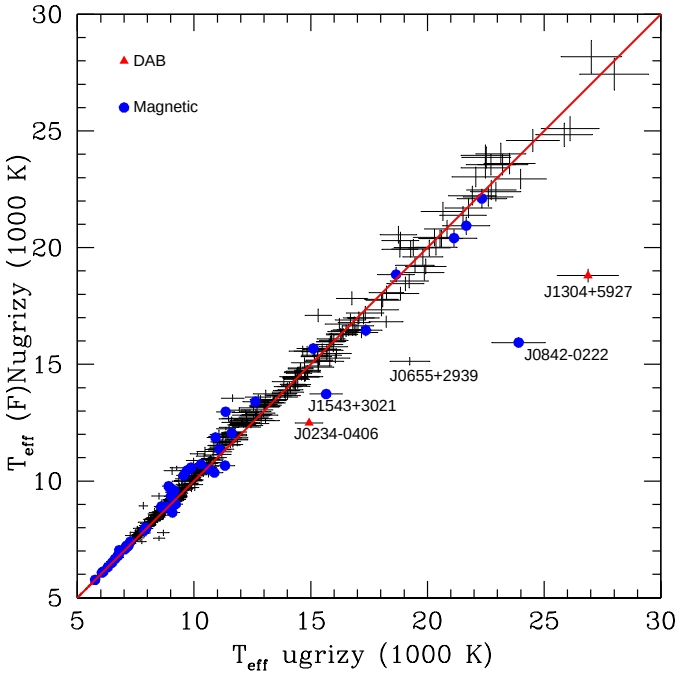


**Figure 3.4.2:** A comparison between the effective temperature derived from optical only data versus a combination of the UV and optical data for the DA white dwarfs in the 100 pc SDSS ∩ GALEX sample. Unusual objects, magnetic DAH and mixed composition DAB white dwarfs, are labeled with blue dots and red triangles, respectively.

differences between the best-fit parameters derived from optical only data and the optical + UV photometry. However, the addition of the GALEX FUV and NUV data helps improve the statistical errors in the model fits, especially for the hotter white dwarfs where the spectral energy distribution peaks in the UV. For example, for white dwarfs with $T_{\rm eff} < 10000$ K, the statistical errors in optical + UV temperature estimates are on average better by a factor of 1.3 compared to the errors based on the optical data only, but they are better by a factor of 2.5 for $T_{\rm eff} > 15000$ K.

The five significant outliers in Figure 3.4.2 all appear to be fainter than expected in the UV, and that is why their best-fitting temperatures based on the optical + UV model fits are cooler than those based on the optical data. These outliers include two DA white dwarfs with unusual atmospheric composition. J1304+5927 (GD 323, see Figure 3.4.1) and J0234−0406 (PSO J038.5646−04.1025). The latter was originally classified as a DA white dwarf based on a low-resolution spectrum obtained by Kilic et al. (2020). Higher signal-to-noise ratio follow-up spectroscopy by Gentile Fusillo et al. (2021) demonstrated that J0234−0406 is in fact a DABZ white dwarf that hosts a gaseous debris disk. Even though its spectral appearance is visually dominated by broad Balmer absorption lines, the atmosphere of J0234−0406 is actually dominated by helium, and that is why it is an outlier in Figure 3.4.2.

J0842−0222 (PSO J130.5623−02.3741) and J1543+3021 (PSO J235.8127+30.3595) are both

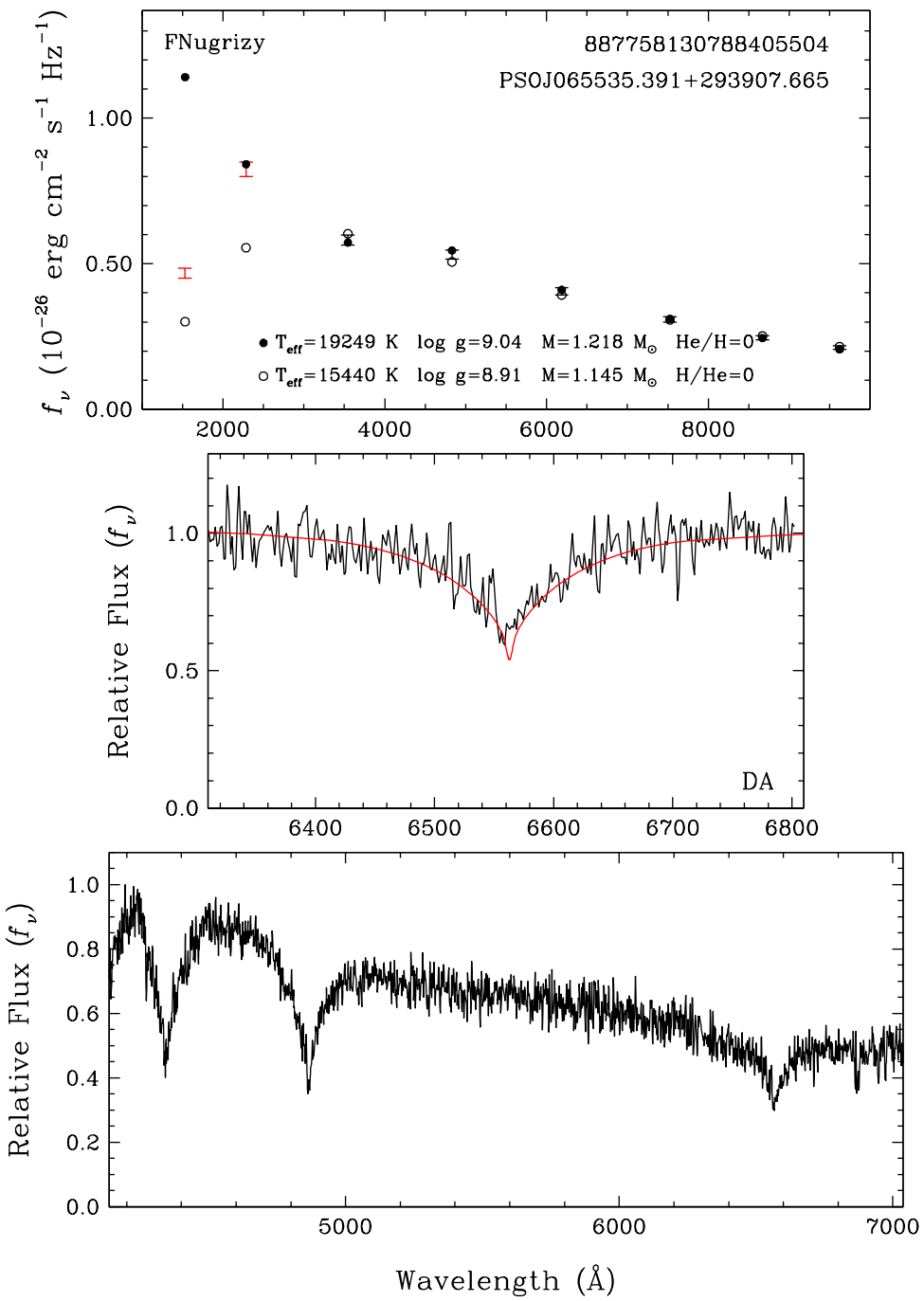


**Figure 3.4.3:** Model atmosphere fits to the DA white dwarf J0655+2939. The top panel shows the best-fitting H (filled dots) and He (open circles) atmosphere white dwarf models to the optical photometry (black error bars). The middle panel shows the observed spectrum (black line) along with the predicted spectrum (red line) based on the pure H atmosphere solution. The bottom panel shows a broader wavelength range.

strongly magnetic and massive white dwarfs with $M > 1.1\ M_{\odot}$ and unusual optical spectra. Schmidt et al. (1986) noted problems with fitting the UV and optical spectral energy distribution of the strongly magnetic white dwarf PG 1031+234 with a field stronger than 200 MG. They found that the IUE and optical/infrared fits cannot be reconciled and that there is no Balmer discontinuity in the spectrum of this object. They attribute this to the blanketing due to hydrogen lines being grossly different, and the addition of a strong opacity source (cyclotron absorption). GD 229 is another example of a magnetic white dwarf with inconsistent UV and optical temperature estimates (Green & Liebert, 1981). Out of the 51 magnetic white dwarfs shown in Figure 3.4.2, only J0842−0222 and J1543+3021 have significantly discrepant UV and optical temperatures. Hence, such inconsistencies seem to impact a fraction of the magnetic white dwarfs in the solar neighborhood.

Another outlier, J0655+2939 (PSO J103.8966+29.6527), is also a massive white dwarf with $M \sim 1.2\ M_{\odot}$. We obtained follow-up optical spectroscopy of J0655+2939 using the KOSMOS spectrograph on the APO 3.5m telescope on UT 2023 Jan 28. We used the blue grism in the high slit position with a $2.05''$ slit, providing wavelength coverage from 4150 Å to 7050 Å and a resolution of 1.42 Å per pixel in the $2 \times 2$ binned mode.

Figure 3.4.3 shows our model fits for J0655+2939. The top panel shows the best-fitting H (filled dots) and He (open circles) atmosphere white dwarf models to the optical photometry (black error bars). Note that the GALEX photometry (red error bars) are not used in these fits. The middle panel shows the observed spectrum (black line) along with the predicted spectrum (red line) based on the pure H atmosphere solution. The bottom panel shows the entire KOSMOS spectrum. We confirm J0655+2939 as a DA white dwarf. Even though its Balmer lines and the optical + NUV photometry agree with the pure H atmosphere solution, J0655+2939 is significantly fainter than expected in the GALEX FUV band. The source of this discrepancy is unclear, but the observed H$\alpha$ line core is also slightly shallower than expected based on the pure H atmosphere model. This could indicate Zeeman splitting of the line core, but our low resolution spectrum does not permit a definitive interpretation of the source of discrepancy for this object.

### 3.4.2. The MWDD DA sample

The 100 pc SDSS DA white dwarf sample discussed in the previous section clearly demonstrates that 1) there are no large-scale systematic differences between the model fits using optical only data ($ugriz$) and a combination of optical + UV data, and 2) GALEX FUV and NUV data can be used to identify unusual DA white dwarfs with helium-rich atmospheres or strong magnetic fields. We now expand our study to the entire Montreal White Dwarf Database DA white dwarf sample in the Pan-STARRS ∩ GALEX footprint.

Figure 3.4.4 shows a comparison between the effective temperatures derived from optical and UV data for the DA white dwarfs in the SDSS footprint. The difference from Figure 3.4.2 is that

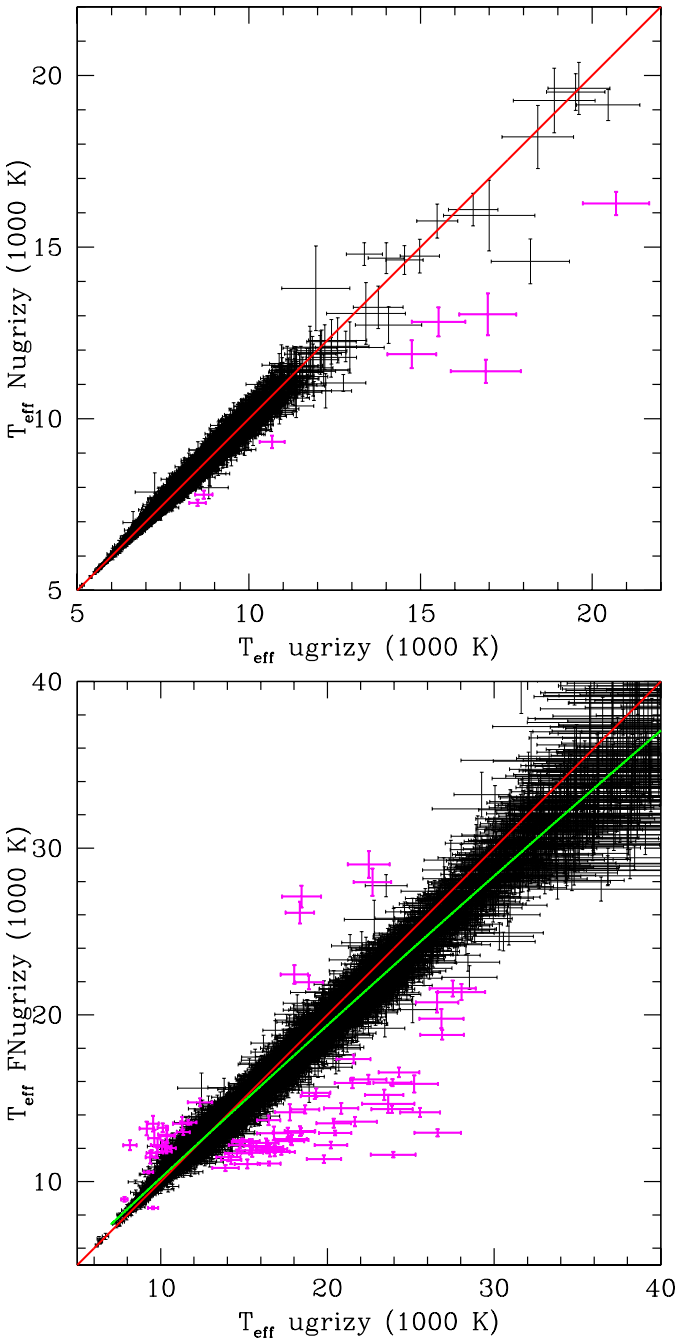


**Figure 3.4.4:** A comparison between the effective temperature derived from optical only data (SDSS $u$ and Pan-STARRS $grizy$) versus the optical + UV data for the DA white dwarfs in the SDSS footprint. The top panel shows objects with only NUV data, whereas the bottom panel includes objects with both FUV and NUV data. The 1:1 line is shown in red. The green line is the best-fitting polynomial to the data. The $3\sigma$ outliers are shown in magenta.

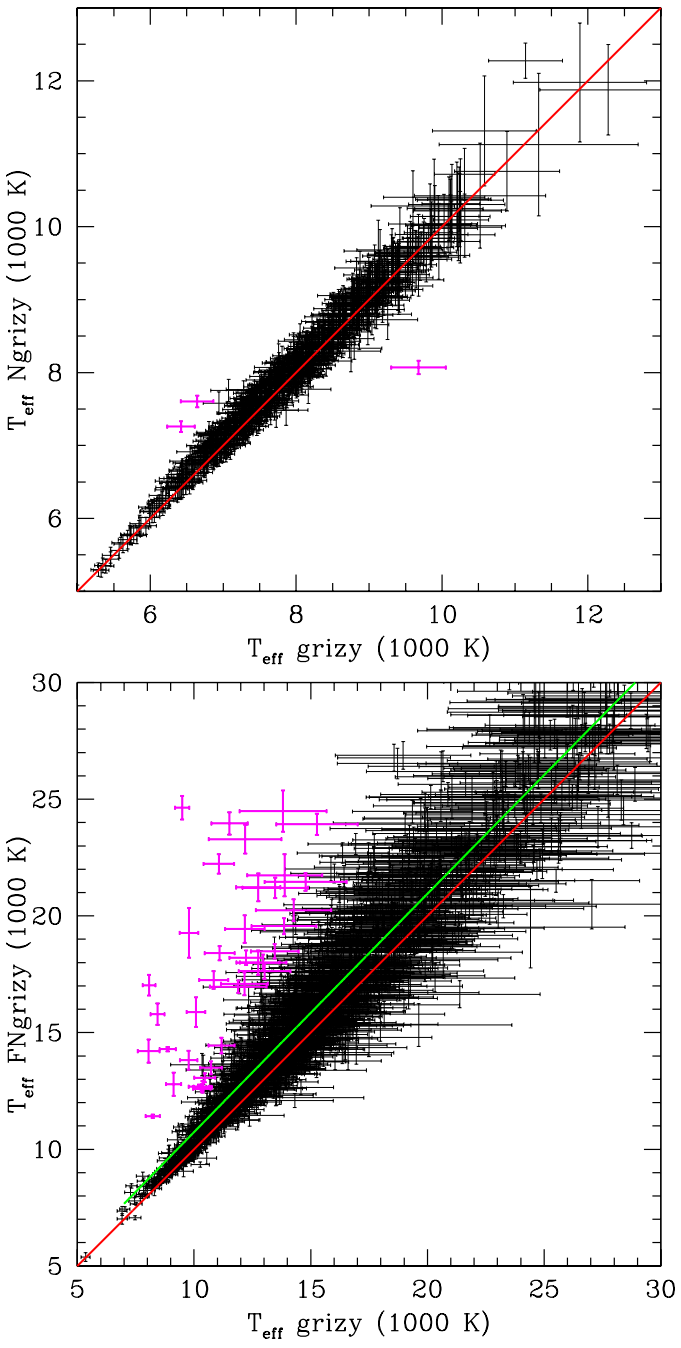


**Figure 3.4.5:** Same as Figure 3.4.4, but for the DA white dwarfs outside of the SDSS footprint.

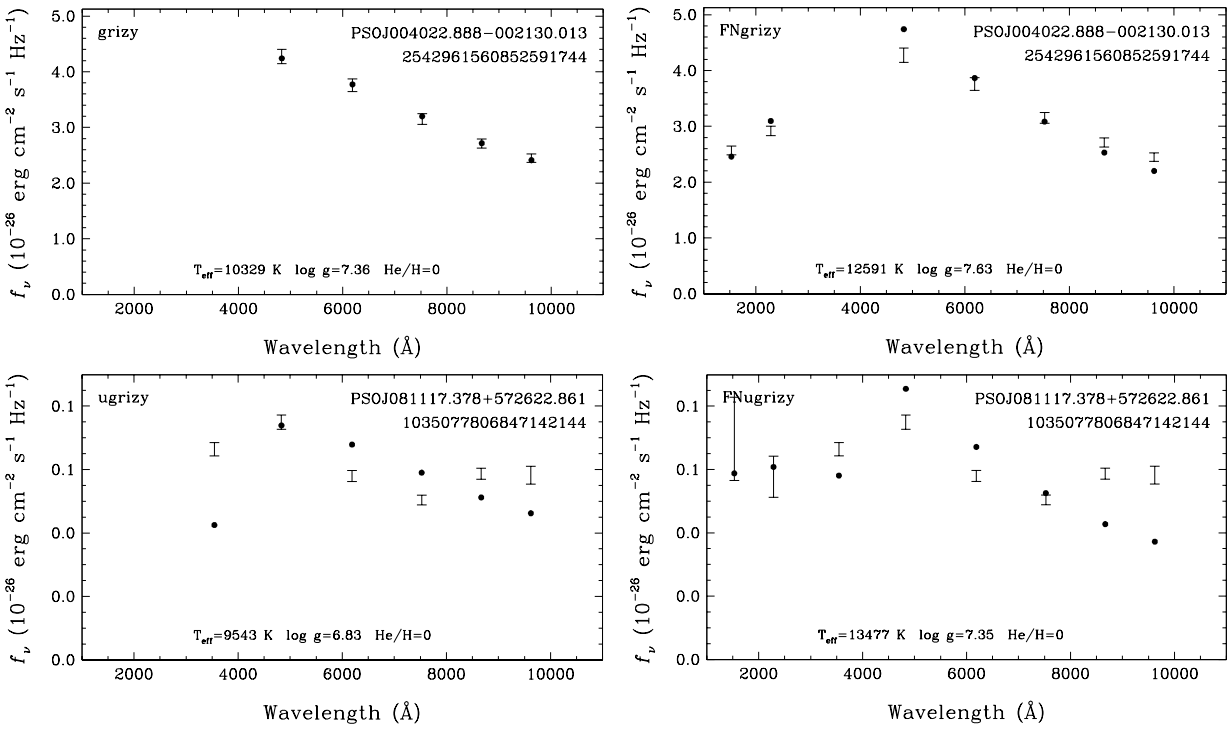


**Figure 3.4.6:** Fits to the optical (left) and optical + UV (right) spectral energy distributions of two of the outliers in our DA white dwarf sample. The top panels show the fits for the double-lined spectroscopic binary WD 0037−006, and the bottom panels show the fits for a previously known DA + M dwarf binary.

the sample shown here extends beyond 100 pc, and therefore is corrected for reddening using the de-reddening procedure from Harris et al. (2006) and the GALEX extinction coefficients from Wall et al. (2019). The top panel includes objects with only NUV data, whereas the bottom panel includes objects with both FUV and NUV data. The red line shows the 1:1 line, and the green line is the best-fitting polynomial to the data. The magenta points mark the outliers that are $3\sigma$ away from both lines. The best-fitting polynomial takes the form

$$y = c_2 x^2 + c_1 x + c_0, \tag{3.1}$$

where y is the $T_{\rm eff} FNugrizy/1000$ and x is $T_{\rm eff} ugrizy/1000$. The coefficients are given in table 3.4.1. The sample with the NUV data only (top panel) is limited mostly to white dwarfs with temperatures between 5000 and 12000 K. This is simply an observational bias; hotter white dwarfs would be brighter in the FUV, and therefore they would have been detected in both NUV and FUV bands.

A comparison between the model parameters obtained from $ugrizy$ and $Nugrizy$ (top panel) shows that there are no systematic differences between the two sets of fits. We find eight $3\sigma$ outliers based on this analysis, all very similar to the outliers shown in Figure 3.4.2 with UV flux deficits.

On the other hand, we do find a systematic trend in the temperature measurements from the fits using the GALEX FUV, NUV, SDSS $u$, and Pan-STARRS $grizy$ filters shown in the bottom panel. Here the best-fitting polynomial shows that the temperatures based on the optical + UV data are slightly underestimated compared to the temperatures obtained from the optical data only. The difference is $-180$ K at 15000 K, $-620$ K at 20000 K, and $-1670$ K at 30000 K. Note that the average temperature errors based on the optical data are 670, 970, and 1850 K at 15000, 20000, and 30000 K, respectively. Hence, the observed systematic shift in this figure is consistent with the optical constraints on the same systems within $1\sigma$. We identify 83 outliers $3\sigma$ away from both the 1:1 line and the best-fitting polynomial (red and green lines in the figure) including a number of UV-excess objects.

Figure 3.4.5 shows a similar comparison for the DA white dwarfs outside of the SDSS footprint. These do not have SDSS $u$-band measurements, hence our model fits are based on the Pan-STARRS $grizy$ and GALEX FUV and NUV bands. The top panel shows the model fits for the DA sample with only NUV data available. Here the 1:1 line provides an excellent match to the parameters obtained from both the optical and the optical + UV analysis. We identify only 3 outliers based on this subsample.

The bottom panel in Figure 3.4.5 reveals a systematic trend in the temperature measurements based on the GALEX FUV + NUV + $grizy$ data compared to the temperatures derived from the optical only data. The best-fitting polynomial takes the form of equation 3.1 where y is the

Table 3.4.1. Coefficients for the best-fitting polynomials in figures 3.4.4 and 3.4.5.

| Coefficient | Figure 3.4.4 | Figure 3.4.5 |
|---|---|---|
| $c_0$ | 0.82743420 | 0.48395959 |
| $c_1$ | 0.94949536 | 1.02740975 |
| $c_2$ | -0.00109481 | -0.00021316 |

$T_{\rm eff}FNgrizy/1000$ and x is $T_{\rm eff}grizy/1000$. The coefficients are given in table 3.4.1. This trend is similar to the one seen for the SDSS sample (bottom panel in Figure 3.4.4) but it is in the opposite direction. The optical + UV analysis leads to temperatures that are slightly over-estimated compared to the analysis using the optical data only. The difference is +850, +950, and +1090 K at 15000, 20000, and 30000 K, respectively. The average temperature errors based on the optical data are 670, 2810, and 6040 K at 15000, 20000, and 30000 K, respectively. Again, the observed systematic trend is consistent with the results from the optical only analysis within $1\sigma$. We identify 41 outliers, all of which are UV-excess objects, based on this diagram.

In total we identify 135 outliers based on this analysis. Because the full width at half-maximum of the GALEX point spread function is about 5 arcsec (Morrissey et al., 2007), blending and contamination from background sources is an issue. We checked the Pan-STARRS stacked images for each of these outliers to identify nearby sources that could impact GALEX, SDSS, or Pan-STARRS photometry measurements. We found that 24 of these outliers were likely impacted by blending sources, reducing the final sample size to 111 outliers.

Table 3.4.2 presents the list of 52 outliers that were previously known to be unusual. This list includes four objects that are confirmed or suspected to be double white dwarfs (PSO J010.0954-00.3584, J055.6249+00.4048, J063.1211−11.5012, and J173.7025+46.8094), 20 confirmed or suspected magnetic white dwarfs, seven DA + M dwarf systems, and 21 objects with an unusual atmospheric composition (DAB etc).

Table 3.4.2. The list of outliers that were previously known to be unusual. The horizontal line separates the UV-deficit (top) and the UV-excess (bottom) objects.

| Object | *Gaia* DR3 Source ID | Spectral Type | Reference |
|---|---|---|---|
| PSO J012.0395−01.4109 | 2530629365419780864 | DA(He) | Kilic et al. (2020) |
| PSO J017.4701+18.0000 | 2785085218267094784 | DA(He) | Kepler et al. (2015) |
| PSO J025.4732+07.7206 | 2571609886069150592 | DAB | Kepler et al. (2015) |
| PSO J027.3938+24.0130 | 291186211300158592 | DZA | Gentile Fusillo et al. (2017) |
| PSO J033.0221+06.7391 | 2521035817229538688 | DA:H: | Kleinman et al. (2013) |
| PSO J038.5646−04.1025 | 2489275328645218560 | DABZ | Gentile Fusillo et al. (2021) |
| PSO J055.6249+00.4048 | 3263696071424152704 | DA+DB | Limoges & Bergeron (2010) |
| PSO J119.5813+35.7453 | 906772187229375104 | DAH | Kleinman et al. (2013) |
| PSO J123.8841+21.9779 | 676473944873877248 | DAB | Kleinman et al. (2013) |
| PSO J125.6983+12.0296 | 649304840753259520 | DAH: | Kepler et al. (2015) |
| PSO J130.5623−02.3741 | 3072348715677121280 | DAH?DBH? | Kilic et al. (2020) |
| PSO J131.8174+48.7057 | 1015028491488955776 | DBH: | Kleinman et al. (2013) |
| PSO J132.3710+28.9556 | 705246450482748288 | DAH | Kleinman et al. (2013) |
| PSO J132.6463+32.1345 | 706974637946866304 | DABZ | Kong et al. (2019) |
| PSO J133.2881+58.7267 | 1037873899276147840 | DABZ | Gentile Fusillo et al. (2019) |
| PSO J136.6362+08.1209 | 584319855260594560 | DAH | Kleinman et al. (2013) |
| PSO J140.1791+04.8533 | 579476334742123904 | DA:B:Z: | Kleinman et al. (2013) |
| PSO J140.7411+13.2557 | 594146225037566976 | DABZ | Kepler et al. (2015) |
| PSO J143.7587+44.4946 | 815134799361707392 | DAH: | Kepler et al. (2015) |
| PSO J144.9871+37.1739 | 799763528023185280 | DAB | Kepler et al. (2015) |
| PSO J150.9846+05.6405 | 3873396705206744064 | DAH | Kleinman et al. (2013) |
| PSO J154.6449+30.5584 | 742562844335742208 | DAH | Kleinman et al. (2013) |
| PSO J179.9671+00.1309 | 3891115064506627840 | DA(He) | Kilic et al. (2020) |
| PSO J182.5106+18.0931 | 3949977724441143552 | DAB | Kepler et al. (2015) |
| PSO J196.1335+59.4594 | 1579147088331814144 | DAB | Wesemael et al. (1993) |
| PSO J198.6769+06.5415 | 3729586288010410496 | DA(He) | Kepler et al. (2015) |
| PSO J201.2108+29.5887 | 1462096958792720384 | DA(He) | Kepler et al. (2016) |
| PSO J206.1217+21.0809 | 1249447115013660416 | DABZ | Kleinman et al. (2013) |
| PSO J211.9610+30.1917 | 1453322271887656448 | DA:H: | Kleinman et al. (2013) |
| PSO J218.8923+04.5738 | 3668901977825959040 | DAX | Kepler et al. (2015) |
| PSO J223.2567+06.8724 | 1160931721694284416 | DA:H: | Kleinman et al. (2013) |

Table 3.4.2 (cont'd)

| Object | *Gaia* DR3 Source ID | Spectral Type | Reference |
|---|---|---|---|
| PSO J223.9933+18.2145 | 1188753901361576064 | DA:H: | Kleinman et al. (2013) |
| PSO J234.3569+51.8575 | 1595298501827000960 | DBA | Kleinman et al. (2013) |
| PSO J240.2518+04.7101 | 4425676551115360512 | DAH | Kleinman et al. (2013) |
| PSO J261.1339+32.5709 | 1333808965722096000 | DAH | Kepler et al. (2015) |
| PSO J341.2484+33.1715 | 1890785517284104960 | DAH/DQ | Kepler et al. (2016) |
| PSO J356.5226+38.8938 | 1919346461391649152 | DAH | Kleinman et al. (2013) |
| PSO J010.0954−00.3584 | 2542961560852591744 | DA+DA | Napiwotzki et al. (2020) |
| PSO J042.5074−04.6175 | 5184589747536175104 | DAH: | Kepler et al. (2016) |
| PSO J051.5805+13.5189 | 17709047809907584 | DAH | Kilic et al. (2020) |
| PSO J063.1211−11.5012 | 3189613692364776576 | DA+DA | Napiwotzki et al. (2020) |
| PSO J065.0980+47.5929 | 257933852944165120 | DAB | Verbeek et al. (2012) |
| PSO J094.8914+55.6121 | 997854527884948992 | DAO | Gianninas et al. (2011) |
| PSO J109.2922+74.0109 | 1112171030998592256 | DAM | Marsh & Duck (1996) |
| PSO J122.8223+57.4396 | 1035077806847142144 | DAM | Rebassa-Mansergas et al. (2016) |
| PSO J123.9537+47.6772 | 931238043230275968 | DAM | Farihi et al. (2010) |
| PSO J140.2868+13.0199 | 594229753561550208 | DAH | Kleinman et al. (2013) |
| PSO J173.7025+46.8094 | 785521450828261632 | DD? | Bédard et al. (2017) |
| PSO J182.0967+06.1655 | 3895444662122848512 | DAM | Rebassa-Mansergas et al. (2016) |
| PSO J224.1602+10.6747 | 1180256944222072704 | DAM | Rebassa-Mansergas et al. (2016) |
| PSO J337.4922+30.4024 | 1900545847646195840 | DAM? | Rebassa-Mansergas et al. (2019) |
| PSO J344.9451+16.4879 | 2828888597582293760 | DAM | Farihi et al. (2010) |

Figure 3.4.6 shows the spectral energy distributions for two of these outliers. The top panels show the fits to the optical and UV + optical spectral energy distributions of the previously known double-lined spectroscopy binary WD 0037−006 (Napiwotzki et al., 2020). Under the assumption of a single star, the Pan-STARRS photometry for WD 0037−006 indicates $T_{\rm eff} = 10330 \pm 380$ K and $\log g = 7.36 \pm 0.05$. Adding the GALEX FUV and NUV data, the best-fitting solution significantly changes to $T_{\rm eff} = 12590 \pm 100$ K and $\log g = 7.63 \pm 0.01$. In addition, this solution has problems matching the entire spectral energy distribution, indicating that there is likely a cooler companion contributing significant flux. This figure demonstrates that double-lined spectroscopic binaries with significant temperature differences between the primary and the secondary star could be identified based on an analysis similar to the one presented here. A similar and complementary method for identifying double-lined spectroscopic binaries was pioneered by Bédard et al. (2017), which use optical photometry and spectroscopy to identify systems with inconsistent photometric and spectroscopic solutions.

The bottom panels in Figure 3.4.6 show the fits to a previously confirmed DA + M dwarf system in our sample (Rebassa-Mansergas et al., 2016). Here the optical data is clearly at odds with a single

DA white dwarf, and GALEX FUV and NUV data reveal UV-excess from a hotter white dwarf. The analysis using $FNugrizy$ photometry confirms excess emission in the Pan-STARRS $zy$-bands, consistent with an M dwarf companion.

Table 3.4.3 presents the list of 59 newly identified outliers among the DA white dwarfs with GALEX data; 24 of them show flux deficits in the UV (their optical + UV temperatures are lower than the temperatures based on the optical data only), and 35 are UV-excess objects. We include the spectral types from the literature for each source.

Even though the 24 UV-deficit objects (shown in the top half of the table) are classified as DA in the literature, our analysis indicates that they are unusual. For example, re-inspecting the SDSS spectra for three of the sources classified as DAZ in the literature, we find that the Ca H and K lines are actually stronger than the Balmer lines, indicating that they are in fact DZA white dwarfs.

Similarly, re-inspecting the SDSS and LAMOST spectra for four of these sources (PSO J018.6848+35.4095, J151.1401+40.2417, J196.7725+49.1045, and J338.5445+25.1894), we find that their Balmer lines are much weaker than expected for these relatively warm white dwarfs with $T_{\rm eff} > 10,000$ K. Figure 3.4.7 shows the model fits to three of these objects based on the optical photometry. All three stars are significantly fainter than expected in the FUV and NUV bands compared to the pure H atmosphere models. The UV photometry and the weak Balmer lines indicate that these stars are likely DA(He) white dwarfs with helium dominated atmospheres.

The newly identified UV-excess sample likely includes many binaries, including white dwarf + main-sequence and double white dwarf systems. We classify 14 of these systems as likely DA + M dwarfs based on their spectral energy distributions, which are dominated by the white dwarf in the UV and by a redder source in the Pan-STARRS $zy$ bands. Four of these DA + M dwarf systems are also resolved in the Pan-STARRS $zy$ band stacked images, but the resolved companions are not included in the Pan-STARRS photometric catalog. However, one of these resolved systems is confirmed to be a physical binary through *Gaia* astrometry. Both components of PSO J211.4189+74.6498 are detected in *Gaia* with source IDs *Gaia* DR3 1712016196599965312 and 1712016196599171840.

Figure 3.4.8 shows the fits to the optical and optical + UV spectral energy distributions for three of the newly identified UV-excess sources that may be double white dwarfs. There are small but significant temperature discrepancies between the photometric solutions relying on optical and optical + UV data and also the optical spectroscopy. For example, for PSO J218.2047+01.7710 the model fits to the optical photometry give $T_{\rm eff} = 10341 \pm 329$ K and $\log g = 7.51 \pm 0.05$, while the fits to the optical + UV photometry give $T_{\rm eff} = 11793 \pm 98$ K and $\log g = 7.74 \pm 0.02$. Fitting the normalized Balmer line profiles, Tremblay et al. (2011) obtained $T_{\rm eff} = 11360 \pm 120$ K and $\log g = 8.19 \pm 0.06$ for the same star. The inconsistent $\log g$ estimates can be explained if the

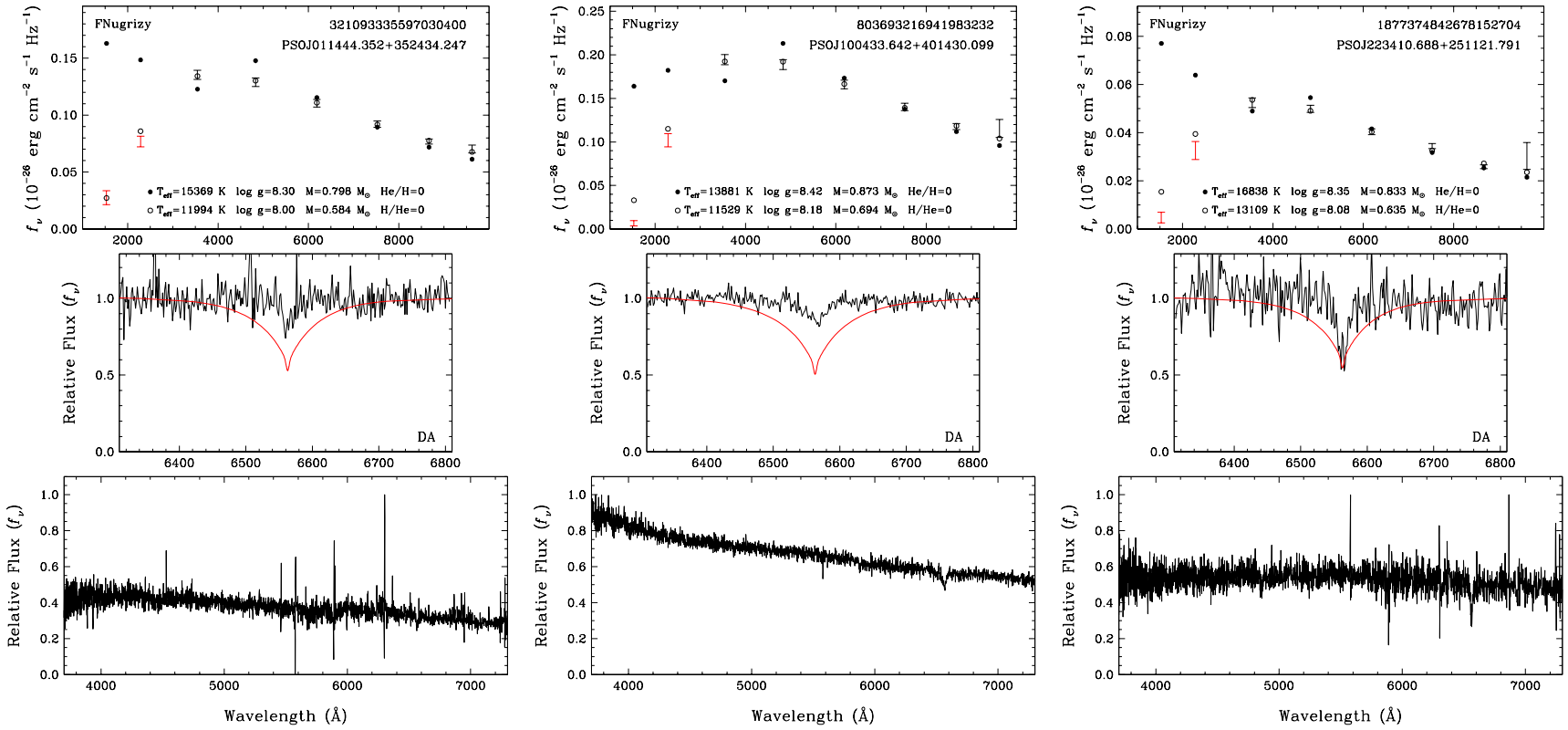


**Figure 3.4.7:** Model atmosphere fits to three DA white dwarfs with UV flux deficits. The top panels show the best-fitting H (filled dots) and He (open circles) atmosphere white dwarf models to the optical photometry (black error bars). The middle panels show the observed spectrum (black line) along with the predicted spectrum (red line) based on the pure H atmosphere solution. The bottom panels show a broader wavelength range. GALEX FUV and NUV data clearly favor the He-dominated atmosphere solutions, which are also confirmed by the relatively weak Balmer lines in their spectra.

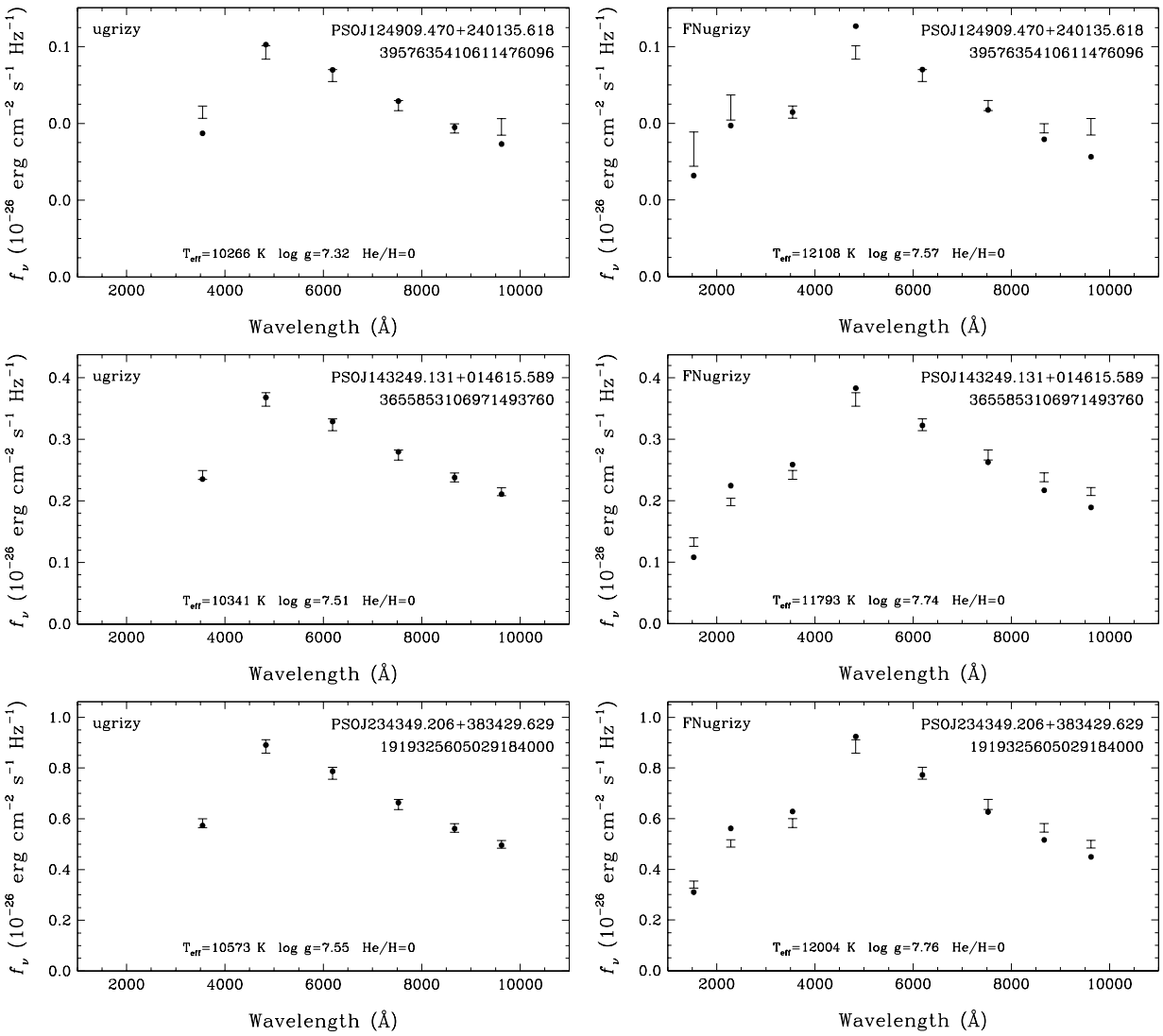


**Figure 3.4.8:** Fits to the optical (left) and optical + UV (right) spectral energy distributions of three of the newly identified UV-excess sources in our DA white dwarf sample. The inconsistent temperature estimates from the optical and UV photometry and optical spectroscopy indicate that they may be double white dwarfs.

Table 3.4.3. Newly identified outliers among the DA white dwarf population with GALEX data.
The horizontal line separates the UV-deficit (top) and the UV-excess (bottom) objects.

| Object | *Gaia* DR3 Source ID | Optical $T_{\rm eff}$ (K) | Optical + UV $T_{\rm eff}$ (K) | Spectral Type | Reference | Notes |
|---|---|---|---|---|---|---|
| PSO J018.6848+35.4095 | 321093335597030400 | 15369 ± 678 | 11872 ± 223 | DA | Gentile Fusillo et al. (2015) | DA(He) LAMOST |
| PSO J032.2011+12.2256 | 73623921366683008 | 27516 ± 1379 | 21586 ± 476 | DA | Kleinman et al. (2013) | |
| PSO J043.8655+02.6202 | 1559111783825792 | 8685 ± 254 | 7788 ± 117 | DA | Kilic et al. (2020) | |
| PSO J056.0479+15.1626 | 42871199614383616 | 8503 ± 241 | 7548 ± 90 | DA | Andrews et al. (2015) | |
| PSO J103.8966+29.6527 | 887758130788405504 | 19249 ± 849 | 15130 ± 168 | DA | Kilic et al. (2020) | massive |
| PSO J130.7484+10.6677 | 598412403168328960 | 15748 ± 731 | 12139 ± 293 | DAZ | Kepler et al. (2015) | DZA SDSS |
| PSO J132.2963+14.4454 | 608922974120358784 | 19793 ± 1038 | 11354 ± 226 | DA | Gentile Fusillo et al. (2019) | |
| PSO J139.0499+34.9872 | 714469355877947136 | 23646 ± 1571 | 14667 ± 545 | DA | Kleinman et al. (2013) | massive |
| PSO J151.1401+40.2417 | 803693216941983232 | 13881 ± 797 | 10816 ± 188 | DA | Kepler et al. (2015) | DA(He) SDSS |
| PSO J158.8293+27.2510 | 728222390915647872 | 17876 ± 998 | 12484 ± 307 | DA | Gentile Fusillo et al. (2019) | |
| PSO J159.5929+37.3533 | 751930335511863040 | 14891 ± 628 | 12383 ± 194 | DA:DC: | Kleinman et al. (2013) | DAB SDSS |
| PSO J163.5943−02.7860 | 3801901270848297600 | 25209 ± 1429 | 15858 ± 522 | DA | Croom et al. (2001) | massive |
| PSO J172.6518−00.3655 | 3797201653208863360 | 15198 ± 761 | 11058 ± 264 | DA:Z | Kleinman et al. (2013) | DZA SDSS |
| PSO J180.6015+40.5822 | 4034928775942285184 | 16551 ± 835 | 11880 ± 377 | DA | Kleinman et al. (2013) | DC: SDSS |
| PSO J196.7725+49.1045 | 1554826818838504576 | 14573 ± 736 | 11689 ± 225 | DA: | Kleinman et al. (2013) | DA(He) SDSS |
| PSO J213.8277+31.9308 | 1477633195532154752 | 16960 ± 829 | 13040 ± 608 | DAZ | Gentile Fusillo et al. (2019) | DZA SDSS |
| PSO J215.2971+38.9912 | 1484931581918492544 | 17743 ± 873 | 14159 ± 483 | DA: | Kleinman et al. (2013) | DC: SDSS |
| PSO J231.8495+06.7581 | 1162614902197098624 | 16792 ± 1013 | 12897 ± 411 | DA | Carter et al. (2013) | massive |
| PSO J249.3471+53.9644 | 1426634650780861184 | 16315 ± 761 | 12321 ± 257 | DAZ | Kepler et al. (2016) | |
| PSO J309.1036+77.8178 | 2290767158609770240 | 28040 ± 1427 | 21372 ± 486 | DA | Bédard et al. (2020) | |

Table 3.4.3 (cont'd)

| Object | *Gaia* DR3 Source ID | Optical $T_{\rm eff}$ (K) | Optical + UV $T_{\rm eff}$ (K) | Spectral Type | Reference | Notes |
|---|---|---|---|---|---|---|
| PSO J324.1725+01.0846 | 2688259922223271296 | 16404 ± 937 | 12078 ± 389 | DA | Vidrih et al. (2007) | |
| PSO J338.5445+25.1894 | 1877374842678152704 | 16838 ± 892 | 11787 ± 266 | DA | Gentile Fusillo et al. (2019) | DA(He) SDSS |
| PSO J342.5363+22.7580 | 2836800855054851456 | 26580 ± 1279 | 20752 ± 605 | DA | Bédard et al. (2020) | |
| PSO J348.7601+22.1674 | 2838958711048617856 | 26837 ± 1327 | 19773 ± 571 | DA | Kleinman et al. (2013) | |
| PSO J003.9449−30.1015 | 2320237751020937728 | 9768 ± 375 | 13816 ± 408 | DA | Vennes et al. (2002) | |
| PSO J009.0492−17.5443 | 2364297204875140224 | 13479 ± 1408 | 21203 ± 437 | DA | Gianninas et al. (2011) | |
| PSO J015.0435−28.1077 | 5033974938207807488 | 13023 ± 1105 | 17630 ± 337 | DA | Croom et al. (2004) | |
| PSO J019.3103+24.6726 | 294062563782633216 | 12160 ± 1007 | 17090 ± 490 | DA | Kleinman et al. (2013) | |
| PSO J021.9568+73.4798 | 535482641132742400 | 6422 ± 190 | 7259 ± 75 | DA | Limoges et al. (2015) | |
| PSO J023.0575−28.1766 | 5035296654263954304 | 12745 ± 931 | 17999 ± 527 | DA | Croom et al. (2004) | |
| PSO J029.9572−27.8589 | 5024390701506507648 | 11176 ± 562 | 14449 ± 337 | DA | Croom et al. (2004) | |
| PSO J041.4724−12.7058 | 5158731712247303040 | 9493 ± 307 | 24634 ± 504 | DA | Kilkenny et al. (2016) | DAM? |
| PSO J051.6792+69.4045 | 494644717692834944 | 13855 ± 1393 | 19565 ± 343 | DA | Gianninas et al. (2011) | |
| PSO J052.0294+52.9603 | 443375555640546944 | 10729 ± 467 | 13492 ± 282 | DA | Verbeek et al. (2012) | |
| PSO J052.2834+52.7335 | 443274778529615232 | 10363 ± 382 | 12680 ± 249 | DA | Verbeek et al. (2012) | |
| PSO J102.2271+38.4434 | 944388335442133888 | 13883 ± 1606 | 21741 ± 901 | DA | Kleinman et al. (2013) | |
| PSO J125.7399+57.8364 | 1034975243028553600 | 18178 ± 2420 | 31076 ± 1012 | DA | Bédard et al. (2020) | |
| PSO J143.4929+17.7146 | 632864633657062400 | 13811 ± 1864 | 24486 ± 883 | DA | Bédard et al. (2020) | DAM? |
| PSO J143.5436+22.4702 | 644043544469790720 | 14268 ± 1613 | 20245 ± 465 | DA | Kleinman et al. (2013) | DAM? |
| PSO J146.2852+62.7948 | 1063508669280315776 | 9623 ± 370 | 12604 ± 502 | DA | Kleinman et al. (2013) | DAM? |

Table 3.4.3 (cont'd)

| Object | *Gaia* DR3 Source ID | Optical $T_{\rm eff}$ (K) | Optical + UV $T_{\rm eff}$ (K) | Spectral Type | Reference | Notes |
|---|---|---|---|---|---|---|
| PSO J149.4751+85.4946 | 1147853241336105344 | 28499 ± 4417 | 50953 ± 4975 | DA | Gianninas et al. (2011) | |
| PSO J150.3866+01.5162 | 3835962526168788608 | 22704 ± 1127 | 27966 ± 821 | DA | Kepler et al. (2015) | |
| PSO J167.1417+31.8979 | 757803896562843392 | 14778 ± 1760 | 21458 ± 382 | DA | Gianninas et al. (2011) | |
| PSO J192.2894+24.0266 | 3957635410611476096 | 10266 ± 381 | 12108 ± 291 | DA | Kleinman et al. (2013) | |
| PSO J200.6206+01.0147 | 3688065808367722368 | 9383 ± 291 | 11459 ± 371 | DA | Croom et al. (2004) | DAM? |
| PSO J211.4189+74.6498 | 1712016196599965312 | 8237 ± 305 | 11420 ± 77 | DA | Mickaelian (2008) | resolved DAM |
| PSO J218.2047+01.7710 | 3655853106971493760 | 10341 ± 329 | 11793 ± 97 | DA | Kleinman et al. (2013) | |
| PSO J221.4238+41.2449 | 1489712503290614912 | 9786 ± 396 | 19274 ± 1067 | DA | Bédard et al. (2020) | DAM? |
| PSO J223.4269+46.9171 | 1590342178286505216 | 12174 ± 851 | 19440 ± 593 | DA | Kleinman et al. (2013) | |
| PSO J240.6992+43.8100 | 1384551977098980608 | 10070 ± 352 | 12113 ± 369 | DA | Kleinman et al. (2013) | resolved DAM? |
| PSO J240.8660+19.6618 | 1203265358904378880 | 10085 ± 401 | 15880 ± 632 | DA | Kleinman et al. (2013) | DAM? |
| PSO J244.6129+20.5911 | 1202035422006406400 | 9808 ± 394 | 12191 ± 410 | DA | Kleinman et al. (2013) | resolved DAM? |
| PSO J259.6449+01.9471 | 4387171623850187648 | 10215 ± 438 | 12685 ± 84 | DA | McCleery et al. (2020) | |
| PSO J263.1394+32.8366 | 4601788317833882240 | 9790 ± 353 | 11747 ± 336 | DA | Kepler et al. (2015) | DAM? |
| PSO J276.0344+35.2718 | 2095603539740855296 | 11063 ± 653 | 22229 ± 415 | DA | Mickaelian (2008) | DAM? |
| PSO J334.7157−29.4534 | 6615258025441899776 | 10838 ± 624 | 17254 ± 376 | DA | Croom et al. (2004) | DAM? |
| PSO J346.5586−28.0099 | 6606686198432918656 | 11516 ± 779 | 23961 ± 485 | DA | Croom et al. (2004) | resolved DAM? |
| PSO J352.1333−30.0610 | 2329285662270302976 | 12190 ± 1555 | 23284 ± 616 | DA | Vennes et al. (2002) | |
| PSO J355.9551+38.5749 | 1919325605029184000 | 10573 ± 344 | 12004 ± 78 | DA | Kleinman et al. (2013) | |

photometry is contaminated by a companion (see also Bédard et al., 2017), and the small temperature differences between the different solutions favor a white dwarf companion rather than a cool, late-type M dwarf star. Follow-up spectroscopy of these three systems, as well as the rest of the UV-excess sample would be helpful for constraining the nature of these objects and identifying additional double white dwarf binaries.

### 3.5. Results from UV Magnitude Comparison

The optical/UV temperature comparison method presented in the previous section provides an excellent method to identify sources with grossly different temperatures. However, it may miss some sources with unusual UV fluxes. Those model fits rely on three ($gri$) to six ($ugrizy$) optical filters versus one or two GALEX UV filters, hence the UV data have a lesser weight in constraining the temperatures.

To search for additional outliers that were potentially missed by the temperature comparison method, here we use model fits to the optical photometry plus *Gaia* parallaxes to predict the brightness of each star in the GALEX filters, and search for significant outliers using FUV and NUV data. To obtain the best constraints on the predicted FUV and NUV brightnesses of each source, we further require our stars to have photometry in the SDSS $u$ filter as well as all of the Pan-STARRS filters. Our final magnitude comparison sample contains 10049 DA white dwarfs with photometry in at least one of the GALEX filters, the SDSS $u$, and the Pan-STARRS $grizy$ filters.

Figure 3.5.1 shows a comparison of the observed and predicted FUV (top) and NUV (bottom panel) magnitudes of the 10049 DA white dwarfs in our magnitude comparison sample. The blue dashed line is the 1:1 correlation between observed and model magnitudes. The green diamonds are previously known DAB white dwarfs while the green triangles are DA white dwarfs that have significant amounts of helium in their atmospheres, making the use of pure hydrogen atmosphere models inappropriate. The yellow diamonds are previously known magnetic white dwarfs and the black triangles are previously known DA + M dwarf systems. The blue diamonds are white dwarfs with uncertain (e.g., DA:) classifications.

As with the temperature comparison sample, blending and contamination from background sources is an issue for some sources. We checked the Pan-STARRS stacked images for each of these outliers to identify nearby sources that could impact GALEX, SDSS, or Pan-STARRS photometry measurements. The outliers that were affected by contamination are marked by blue triangles in Figure 3.5.1. The red squares are 30 newly identified $3\sigma$ outliers. Table 3.5.1 presents this list along with their photometric and spectroscopic temperatures based on the optical data.

Figure 3.5.2 displays the spectral energy distributions for four of these outliers. Outliers with UV-excesses, such as PSO J226.4550+11.0849 shown in the top right panel of Figure 3.5.2, are likely binaries. Outliers with UV-deficits, such as PSO J253.3655+27.5061 shown in the bottom

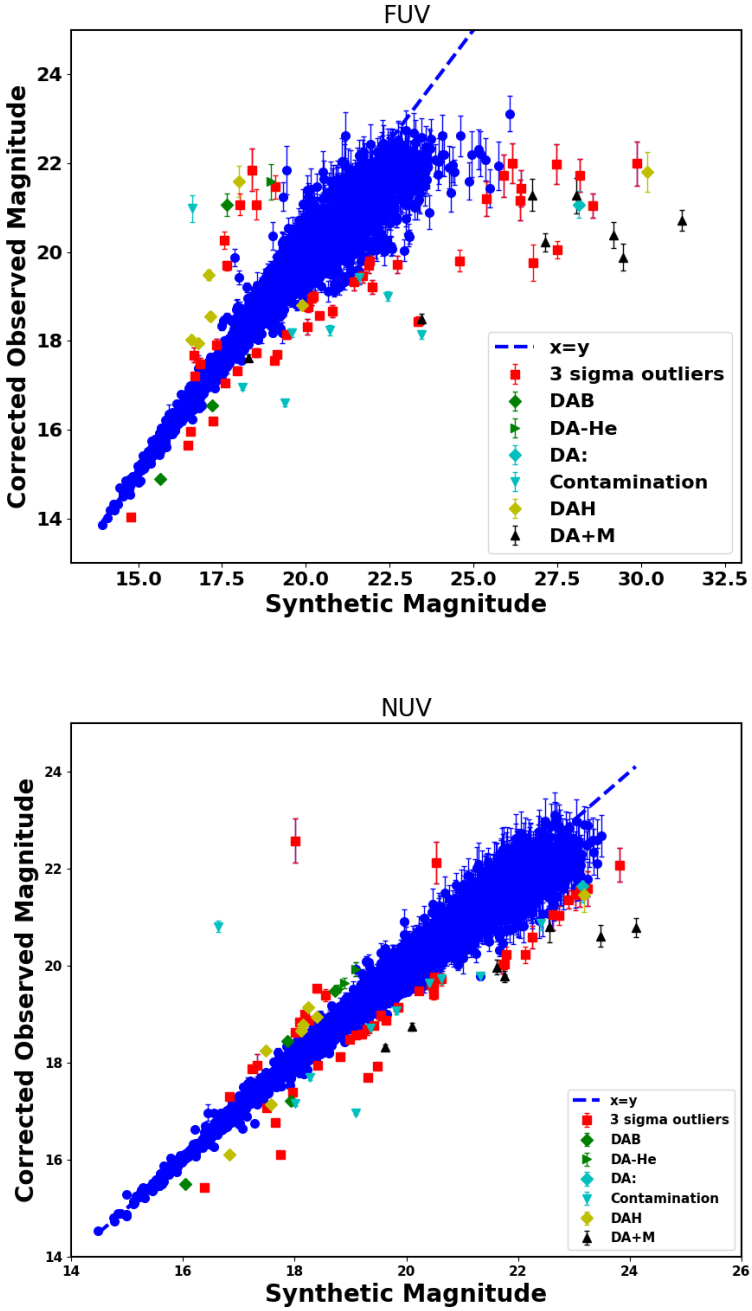


**Figure 3.5.1:** Comparison between observed and model FUV (top) and NUV (bottom) magnitudes. The blue dashed line is the 1:1 correlation. The green diamonds are previously known DAB white dwarfs, the green triangles are previously known DA-He white dwarfs, the cyan diamonds are white dwarfs with uncertain classifications, the cyan triangles are objects with contaminated photometry, and the yellow diamonds are previously known magnetic white dwarfs. Previously unknown $3\sigma$ outliers are plotted as red squares.

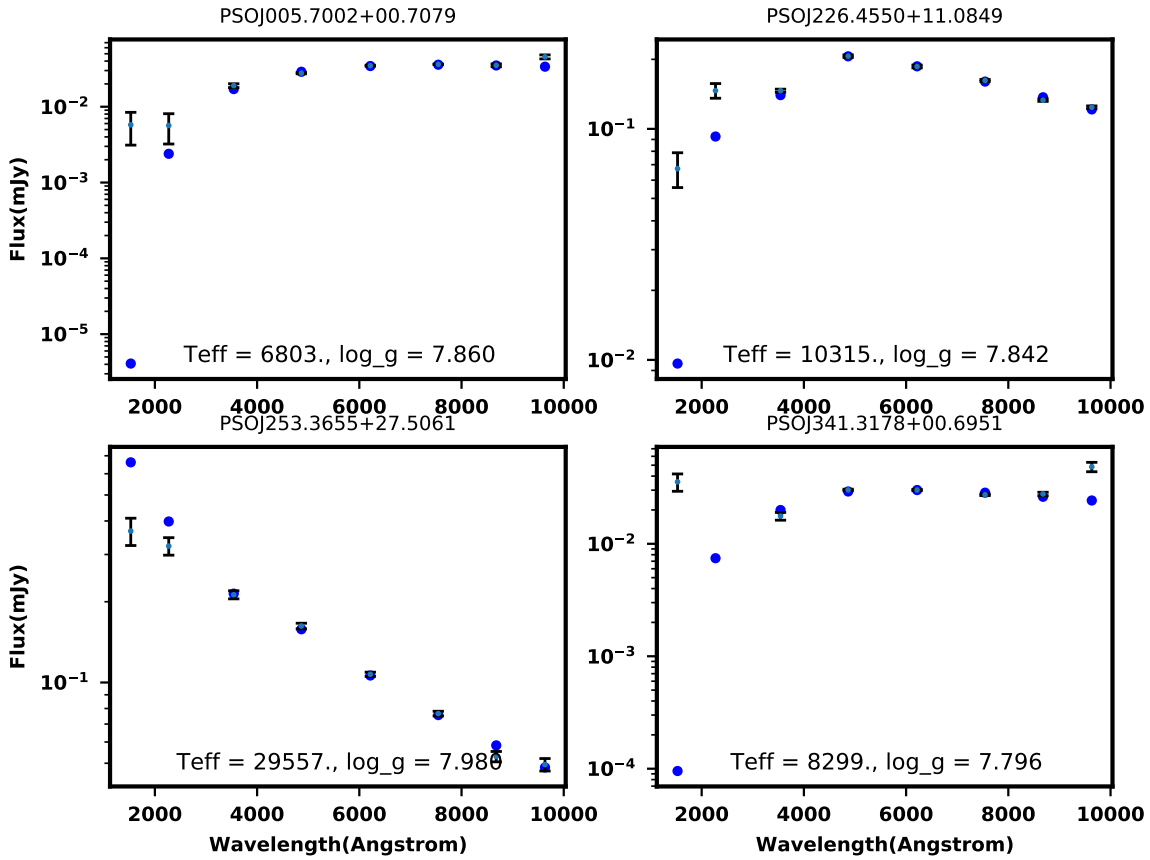


**Figure 3.5.2:** Spectral energy distributions of four newly identified outliers in the magnitude comparison sample. The filled dots are the model fluxes and the error bars are the observed photometry.

Table 3.5.1. Additional outliers identified through a comparison of the observed and predicted UV magnitudes.

| Object | *Gaia* DR3 Source ID | Photometric $T_{\rm eff}$ (K) | Spectroscopic $T_{\rm eff}$ (K) | Spectral Type | Reference | Notes |
|---|---|---|---|---|---|---|
| PSO J001.0830+23.8334 | 2849729771768028544 | 27453 | 34738 | DA | Kepler et al. (2016) | |
| PSO J004.9372+33.6842 | 2864011530163554816 | 7513 | 8982 | DA | Kepler et al. (2016) | |
| PSO J005.7002+00.7079 | 2546893650655427840 | 6803 | 6992 | DA | Kleinman et al. (2013) | DAM? |
| PSO J021.8549+27.6214 | 296372465914661248 | 6823 | 6723 | DA | Kepler et al. (2016) | |
| PSO J056.0308-05.2121 | 3244802712151826048 | 10331 | 12371 | DA | Kleinman et al. (2013) | DAM? |
| PSO J118.9063+21.1283 | 673549759340742272 | 9270 | 9941 | DA | Kleinman et al. (2013) | DAM? |
| PSO J126.3419+17.4310 | 662102679359467648 | 7867 | 7838 | DA | Kleinman et al. (2013) | |
| PSO J137.9380+35.5266 | 714377928911156992 | 14027 | 19527 | DA | Kleinman et al. (2013) | |
| PSO J149.4951+57.6078 | 1046386971133757184 | 10292 | 11288 | DA | Kleinman et al. (2013) | DAM? |
| PSO J152.4806+00.1622 | 3831830527112439936 | 10569 | 10513 | DA | Kleinman et al. (2013) | |
| PSO J176.3500+24.1592 | 4004972723377902592 | 7188 | 7403 | DA | Kepler et al. (2016) | |
| PSO J189.9978+33.1080 | 1514768341766532992 | 10348 | 10957 | DA | Kleinman et al. (2013) | DAM? |
| PSO J204.9827+60.1751 | 1662524184641472640 | 7888 | 9463 | DA | Kleinman et al. (2013) | |
| PSO J205.8897+23.2339 | 1443624343108905216 | 9516 | 10373 | DA | Kleinman et al. (2013) | |
| PSO J210.9347+37.1660 | 1483513830393895680 | 8703 | 11040 | DA | Kepler et al. (2015) | DAM? |
| PSO J213.9910+62.5129 | 1666750569898974208 | 9593 | 10114 | DA | Kleinman et al. (2013) | |
| PSO J226.4550+11.0849 | 1180520345976350208 | 10315 | 11354 | DA | Kleinman et al. (2013) | |
| PSO J226.6089+06.6459 | 1160300056558791168 | 9500 | 10670 | DA | Farihi et al. (2012) | |

Table 3.5.1 (cont'd)

| Object | *Gaia* DR3 Source ID | Photometric $T_{\rm eff}$ (K) | Spectroscopic $T_{\rm eff}$ (K) | Spectral Type | Reference | Notes |
|---|---|---|---|---|---|---|
| PSO J227.2923+37.1129 | 1292306146987734784 | 8264 | 8526 | DA | Kepler et al. (2015) | |
| PSO J244.4451+40.3379 | 1380686815769537920 | 7600 | 13013 | DA | Kepler et al. (2015) | DAM? |
| PSO J248.9274+26.3827 | 1304383217063475968 | 30346 | 34544 | DA | Kleinman et al. (2013) | |
| PSO J249.2986+12.8853 | 4459617994029737216 | 7824 | 7904 | DA | Kepler et al. (2015) | DAM? |
| PSO J250.5693+22.9411 | 1299405148103896832 | 11188 | 12763 | DA | Kleinman et al. (2013) | |
| PSO J251.3785+41.0348 | 1356243233471452288 | 7884 | 8068 | DA | Kepler et al. (2015) | |
| PSO J253.3655+27.5061 | 1306991499163308160 | 29557 | 30472 | DA | Kleinman et al. (2013) | |
| PSO J328.6059-00.6697 | 2680152673235328768 | 17608 | 20257 | DA | Kleinman et al. (2013) | |
| PSO J331.0859+24.2120 | 1795394701659196032 | 6847 | 6873 | DA | Kepler et al. (2015) | DAM? |
| PSO J341.3178+00.6951 | 2653703714870987648 | 8299 | 9611 | DA | Kleinman et al. (2013) | DAM? |
| PSO J349.8567+07.6224 | 2664938112366990080 | 7394 | 8519 | DA | Kepler et al. (2016) | |
| PSO J358.8416+16.8000 | 2773308246143281920 | 7149 | 7066 | DA | Kepler et al. (2016) | |

left of Figure 3.5.2, do not fit the expectations from pure hydrogen atmosphere models in the UV. Their atmospheres might be dominated by helium or might contain metals, making the use of pure hydrogen models inappropriate. Alternatively, they could also be magnetic. Further observations are needed to confirm the nature of these UV-excess and UV-deficit objects.

## 3.6. Conclusions

We analyzed the UV to optical spectral energy distributions of 14001 DA white dwarfs from the Montreal White Dwarf Database, taking advantage of the GALEX FUV and NUV data and *Gaia* DR3 parallaxes. Using the 100 pc sample where extinction is negligible, we demonstrated that there are no major systematic differences between the best-fit parameters derived from optical only data and the optical + UV photometry. The effective temperatures derived from optical and UV + optical data differ by only $50^{+215}_{-71}$ K. The addition of GALEX FUV and NUV data in the model atmosphere analysis helps improve the statistical errors in the fits, especially for hot white dwarfs.

We used two different methods to identify UV-excess or UV-deficit objects. In the first method, we compared the temperatures obtained from fitting the optical data with those obtained from fitting optical + UV data. We identified 111 significant outliers with this method, including 52 outliers that were previously known to be unusual. These include DA white dwarfs with helium dominated atmospheres, magnetic white dwarfs, double white dwarfs, and white dwarf + M dwarf systems. Out of the 59 newly identified systems, 35 are UV-excess and 24 are UV-deficit objects. In the second method, we used the optical photometry to predict the FUV and NUV magnitudes for each source, and classified sources with $3\sigma$ discrepant FUV and/or NUV photometry as outliers. Using this method, we identified 30 additional outliers.

Combining these two methods, our final sample includes 89 newly identified outliers. The nature of these outliers cannot be constrained by our analysis alone. Many of the UV-excess objects are likely binaries, including double degenerates and white dwarfs with late-type stellar companions. Follow-up spectroscopy and infrared observations of these outliers would help constrain their nature.

## Acknowledgements

This work is supported by NASA under grant 80NSSC22K0479, the NSERC Canada, the Fund FRQ-NT (Québec), and by NSF under grants AST-1906379 and AST-2205736. The Apache Point Observatory 3.5-meter telescope is owned and operated by the Astrophysical Research Consortium.

This work has made use of data from the European Space Agency (ESA) mission *Gaia* (https://www.cosmos.esa.int/Gaia), processed by the *Gaia* Data Processing and Analysis Consortium (DPAC, https://www.cosmos.esa.int/web//dpac/consortium). Funding for the DPAC has been provided by national institutions, in particular the institutions participating in the *Gaia* Multilateral Agreement.

# CHAPTER 4

# Conclusions

## 4.1. Chapter Summaries

In this dissertation, I have presented our work on the study of DA white dwarfs using GALEX photometry. Here I will give a brief summary of that work.

### 4.1.1. Chapter 2

In chapter 2, I presented our work deriving corrections for local nonlinearity in GALEX data as well as our derivation of empirical extinction coefficients for the GALEX FUV and NUV bands. We had an initial sample of 1837 DA white dwarfs that were observed by both SDSS and GALEX. We first considered our $d < 100$ pc sample, for which extinction is not an issue, for improving the corrections for local nonlinearity originally presented in Camarota & Holberg (2014). We found that our sample lacked white dwarfs brighter than 14th magnitude, so we combined our 100 pc sample with the bright white dwarf samples form Camarota & Holberg (2014) and Gianninas et al. (2011). Using this combined sample, we determined an improved linearity correction to the GALEX data. We determined that our linearity corrections are only necessary for objects brighter than 15.95 mag and 16.95 mag for the FUV and NUV bands, respectively.

We then turned our attention to our $d > 250$ pc sample, which suffers from full extinction, for the derivation of empirical extinction coefficients. Before beginning our derivations, we used our improved linearity corrections on the bright stars in our sample. We calculated the $R$ values for each star and then took the weighted mean. Our final extinction coefficients for the GALEX bands are $R_{\rm FUV} = 8.01 \pm 0.07$ and $R_{\rm NUV} = 6.79 \pm 0.04$. These white dwarfs currently provide the best constraints on the linearity corrections and extinction coefficients for GALEX data.

We used our improved linearity corrections and extinction coefficients to search for unusual white dwarfs within our sample. We identified seven previously known objects and five previously unknown objects. The UV-excesses of two of the previously unknown objects (WD 0846+335, SDSS J083029.77+085014.20) can be explained by contaminating background sources. The UV-excesses of SDSS J212411.99−072648.70 can be explained by an inaccurate photometric solution. The remaining two outliers, SDSS J091145.12+353135.60 and SDSS J060255.98+632304.80, require follow-up spectroscopy to verify their nature. SDSS J060255.98+632304.80 is likely to be a previously unknown ZZ Ceti as it's $T_{\rm eff}$ and $\log g$ measurements lie within the ZZ Ceti instability strip.

### 4.1.2. Chapter 3

In chapter 3, I presented our work on DA white dwarfs from the Montreal White Dwarf Database. Taking advantage of the GALEX FUV and NUV data and *Gaia* DR3 parallaxes, we analyzed the UV to optical spectral energy distributions of 14001 DA white dwarfs. We performed two sets of fits on our sample. In the first we used only optical data and in the second we used both the optical and UV data. Using the 100 pc sample where extinction is negligible, we demonstrated that there are no major systematic differences between the best-fit parameters derived from optical only data and the optical + UV photometry. However, the addition of GALEX FUV and NUV data in the model atmosphere analysis does help improve the statistical errors in the fits, especially for hot white dwarfs.

We used two different methods to identify UV-excess or UV-deficit objects. In the first method, we compared the temperatures obtained from fitting the optical data with those obtained from fitting optical + UV data. Using this temperature comparison method, we identified 111 significant outliers. 52 of these outliers were previously known to be unusual. These include DA white dwarfs with helium dominated atmospheres, magnetic white dwarfs, double white dwarfs, and white dwarf + M dwarf systems. Only four out of the 52 previously known outliers are confirmed or suspected double white dwarfs. The majority of the 52 previously known outliers are either magnetic white dwarfs (20 outliers) or have an unusual atmospheric composition (21 outliers). Out of the 59 newly identified systems, 35 are UV-excess and 24 are UV-deficit objects. Our analysis of the spectra of the 24 UV-deficit outliers indicates that, although they are classified as DA white dwarfs in the literature, they have unusual atmospheres. For example, PSO J018.6848+35.4095, J151.1401+40.2417, and J338.5445+25.1894, whose model fits are shown in figure 3.4.7, have Balmer lines that are much weaker than expected given their temperatures. This indicates that these white dwarfs have helium dominated atmospheres. Of the 35 newly identified UV-excess objects, 14 are likely to be DA + M dwarf systems.

In the second method, we used the optical photometry to predict the FUV and NUV magnitudes for each source and compared the predicted GALEX magnitudes to the observed GALEX magnitudes. This magnitude comparison method was used to supplement the temperature comparison method since the UV data, of which there are one or two filters, have a lesser weight in constraining the temperatures than the optical data , of which there are three to six filters. We classified sources with $3\sigma$ discrepant FUV and/or NUV photometry as outliers. Using this magnitude comparison method, we identified 30 additional outliers. 10 of these outliers are likely to be DA + M dwarf systems.

Combining the results of the two methods used to identify UV-excess and UV-deficit objects, our final sample includes 89 newly identified outliers. The nature of these outliers cannot be

constrained by our analysis alone. Many of the UV-excess objects are likely binaries, including double degenerates and white dwarfs with late-type stellar companions. Based on our analysis alone, it is likely that 24 of these objects are DA + M dwarf systems. Follow-up spectroscopy and infrared observations of these outliers would help constrain their nature.

## 4.2. Future Work

There is still a lot of valuable information that GALEX has to offer. In GUVcat alone there are 82,992,086 unique objects covering 24,790 square degrees of the sky. There are many data archives, such as the Montreal White Dwarf Database, containing DA white dwarfs that can be cross matched with GUVcat. The updated linearity correction along with the new empirical GALEX extinction coefficients derived in chapter 2 can be used to accurately study the UV photometry of white dwarfs beyond 100 pc, such as the 758 white dwarfs with distances between 100 pc and 250 pc from our initial sample in chapter 2. This will greatly expand the sample size of white dwarfs that can be studied in the UV.

There are several current and upcoming surveys that are specifically targeting large numbers of white dwarfs spectroscopically. For example, the Dark Energy Spectroscopic Instrument Data Release 1 is expected to contain spectra for over 47000 white dwarf candidates (Manser et al., 2023). There is also the new multi-object survey spectrograph, WEAVE, on the 4.2 m William Herschel Telescope. This spectrograph allows astronomers to take optical spectra of up to ≈1000 objects over a 2 degree field of view in a single exposure. DA white dwarfs make up the majority of the white dwarf population. Hence, the number of spectroscopically confirmed DA white dwarfs will increase significantly in the near future. In addition to these spectroscopic surveys, *Gaia*'s EDR3 contains 259,687 high probability white dwarfs ($P_{\rm WD} > 0.7$) with relatively warm temperatures ($T_{\rm eff} \geq 6500$ K) (Gentile Fusillo et al., 2021). These white dwarfs should be detected by the Ultraviolet Transient Astronomy Satellite (ULTRASAT, Ben-Ami et al., 2022).

### 4.2.1. ULTRASAT

ULTRASAT will perform an all-sky survey during the first 6 months of the mission to a limiting magnitude of 23 to 23.5 in its 230-290 nm NUV passband. This survey will be about an order of magnitude deeper than GALEX. Using the data from the ULTRASAT all-sky survey in combination with *Gaia* DR3 parallaxes and ground- and space-based optical and infrared photometry, we will be able to constrain the masses, temperatures, and cooling ages of a much larger sample of DA white dwarfs. In addition to characterizing the physical parameters of these white dwarfs, the temperature and magnitude comparison methods from chapter 3 can be used to identify unusual objects among the DA white dwarf population.

ULTRASAT will also perform a high-cadence survey. It will observe 2 fields for 6 months with

continuous 300 s exposures. This data can be used to perform a study of the UV variability of a large number of white dwarfs. Using *Kepler* data, Maoz, Mazeh, & McQuillan (2015) found that about half of their white dwarf sample show low-level periodic photometric modulations. These modulations have periods ranging from 1 hr to 10 days. So, ULTRASAT's high-cadence survey will reveal a large number of photometrically varying white dwarfs within the solar neighborhood. This study can reveal several different phenomena.

#### 4.2.2. Binaries

In binary systems, photometric variability can be caused by a number of affects: relativistic beaming, ellipsoidal variations, eclipses, and reflection or re-radiation of the primary white dwarfs light by the secondary companion. These secondary companions can be stellar or sub-stellar, including planetary mass objects.

For stellar or sub-stellar companions, short period binary systems are of particular interest. If the secondary is also a white dwarf, the binary system could be the progenitor of a type Ia supernova, as well as a gravitational wave source for the upcoming *LISA* mission.

For planetary companions, the fate of planetary systems after their host star evolves has long been a question in astronomy. In recent years, several interesting planetary mass objects have been discovered around white dwarfs. Vanderburg et al. (2015) discovered a disintegrating planetesimal around WD 1145+017. Vanderburg et al. (2020) discovered a giant planet candidate around WD 1856+534. A large scale variability survey such as ULTRASAT's high-cadence survey could find other planetary companions around white dwarfs. It can also help to constrain the frequency of planetary mass objects around white dwarfs.

#### 4.2.3. Pulsations

For single white dwarfs, the most common forms of variability are rotation and pulsations. The amplitude of pulsations is significantly higher in the UV, so ULTRASAT will be a very sensitive instrument for detecting DAV and DBV white dwarfs. The 6 month long light curves produced by ULTRASAT's high-cadence survey will provide an excellent opportunity to put constraints on white dwarf pulsation modes and physical parameters, e.g., core composition and surface H layer thickness (Fontaine & Brassard, 2008; Winget & Kepler, 2008; Córsico et al., 2019).

#### 4.2.4. Beyond DA white dwarfs

Although DA white dwarfs make up the majority of the white dwarf population, they are not the only type of white dwarfs. There are thousands of other types of spectroscopically confirmed white dwarfs in the MWDD and the SDSS archives. For example, using a cross-match between the MWDD, *Gaia* DR3, GUVcat, and Pan-STARRS, we found 1445 spectroscopically confirmed white

dwarfs from the MWDD with GALEX FUV and NUV data, Pan-STARRS optical photometry, and $3\sigma$ significant parallax measurements from *Gaia*. Methods similar to those used in this dissertation can be used to study non-DA white dwarfs using GALEX data and, in the future, ULTRASAT data. There is a wealth of information yet to be unearthed in the GALEX archive and many future opportunities to further the study of white dwarfs in the UV.

# References


Andrews J. J., Agüeros M. A., Gianninas A., Kilic M., Dhital S., Anderson S. F., 2015, ApJ, 815, 63

Badenes C., Mullally F., Thompson S. E., Lupton R. H., 2009, ApJ, 707, 971. doi:10.1088/0004-637X/707/2/971

Bailer-Jones C. A. L., Rybizki J., Fouesneau M., Demleitner M., Andrae R., 2021, AJ, 161, 147

Baxter R. B., Dobbie P. D., Parker Q. A., Casewell S. L., Lodieu N., Burleigh M. R., Lawrie K. A., et al., 2014, MNRAS, 440, 3184. doi:10.1093/mnras/stu464

Bédard A., Bergeron P., Fontaine G., 2017, ApJ, 848, 11

Bédard A., Bergeron P., Brassard P., Fontaine G., 2020, ApJ, 901, 93

Ben-Ami S., et al., 2022, in den Herder J.-W. A., Nikzad S., Nakazawa K., eds, Society of Photo-Optical Instrumentation Engineers (SPIE) Conference Series Vol. 12181, Space Telescopes and Instrumentation 2022: Ultraviolet to Gamma Ray. p. 1218105 (arXiv:2208.00159), doi:10.1117/12.2629850

Bergeron P., Saffer R. A., Liebert J., 1992, ApJ, 394, 228. doi:10.1086/171575

Bergeron P., Saumon D., Wesemael F., 1995, ApJ, 443, 764. doi:10.1086/175566

Bergeron P., Wesemael F., Lamontagne R., Fontaine G., Saffer R. A., Allard N. F., 1995, ApJ, 449, 258. doi:10.1086/176053

Bergeron P., Ruiz M. T., Leggett S. K., 1997, ApJS, 108, 339. doi:10.1086/312955

Bergeron P., Leggett S. K., Ruiz M. T., 2001, ApJS, 133, 413. doi:10.1086/320356

Bergeron P., Fontaine G., Billères M., Boudreault S., Green E. M., 2004, ApJ, 600, 404. doi:10.1086/379808

Bergeron P., Dufour P., Fontaine G., Coutu S., Blouin S., Genest-Beaulieu C., Bédard A., Rolland B., 2019, ApJ, 876, 67

Bianchi L., 2011, Ap&SS, 335, 51. doi:10.1007/s10509-011-0612-2

Bianchi L., Shiao B., Thilker D., 2017, ApJS, 230, 24

Bohlin R. C., Dickinson M. E., Calzetti D., 2001, AJ, 122, 2118. doi:10.1086/323137

Bohlin R. C., Koester D., 2008, AJ, 135, 1092. doi:10.1088/0004-6256/135/3/1092

Bours M. C. P., Marsh T. R., Gänsicke B. T., Tauris T. M., Istrate A. G., Badenes C., Dhillon V. S., et al., 2015, MNRAS, 450, 3966. doi:10.1093/mnras/stv889

Bragaglia A., Renzini A., Bergeron P., 1995, ApJ, 443, 735. doi:10.1086/175564

Brown W. R., Kilic M., Gianninas A., 2017, ApJ, 839, 23. doi:10.3847/1538-4357/aa67e4

Camarota L., Holberg J. B., 2014, MNRAS, 438, 3111. doi:10.1093/mnras/stt2422

Cardelli J. A., Clayton G. C., Mathis J. S., 1989, IAUS, 135, 5

Carter P. J., et al., 2013, MNRAS, 429, 2143

Chandrasekhar S., 1931, ApJ, 74, 81. doi:10.1086/143324

Córsico A. H., Althaus L. G., Miller Bertolami M. M., Kepler S. O., 2019, A&ARv, 27, 7. doi:10.1007/s00159-019-0118-4

Croom S. M., Smith R. J., Boyle B. J., Shanks T., Loaring N. S., Miller L., Lewis I. J., 2001, MNRAS, 322, L29

Croom S. M., Smith R. J., Boyle B. J., Shanks T., Miller L., Outram P. J., Loaring N. S., 2004, MNRAS, 349, 1397

Dufour P., Blouin S., Coutu S., Fortin-Archambault M., Thibeault C., Bergeron P., Fontaine G., 2017, in Tremblay P. E., Gaensicke B., Marsh T., eds, Astronomical Society of the Pacific Conference Series Vol. 509, 20th European White Dwarf Workshop. p. 3 (arXiv:1610.00986)

Eisenstein D. J., et al., 2006, ApJS, 167, 40

Farihi J., Becklin E. E., Zuckerman B., 2005, ApJS, 161, 394. doi:10.1086/444362

Farihi J., Hoard D. W., Wachter S., 2010, ApJS, 190, 275

Farihi J., Gänsicke B. T., Steele P. R., Girven J., Burleigh M. R., Breedt E., Koester D., 2012, MNRAS, 421, 1635. doi:10.1111/j.1365-2966.2012.20421.x

Fitzpatrick E. L., 1999, PASP, 111, 63. doi:10.1086/316293

Fontaine G., Brassard P., Bergeron P., 2001, PASP, 113, 409. doi:10.1086/319535

Fontaine G., Brassard P., 2008, PASP, 120, 1043. doi:10.1086/592788

Foreman-Mackey D., Hogg D. W., Lang D., Goodman J., 2013, PASP, 125, 306. doi:10.1086/670067

Genest-Beaulieu C., Bergeron P., 2019, ApJ, 882, 106

Gentile Fusillo N. P., et al., 2015, MNRAS, 452, 765

Gentile Fusillo N. P., Gänsicke B. T., Farihi J., Koester D., Schreiber M. R., Pala A. F., 2017, MNRAS, 468, 971

Gentile Fusillo N. P., et al., 2019, MNRAS, 482, 4570

Gentile Fusillo N. P., et al., 2021, MNRAS, 504, 2707

Gentile Fusillo N. P., Tremblay P.-E., Cukanovaite E., Vorontseva A., Lallement R., Hollands M., Gänsicke B. T., et al., 2021, MNRAS, 508, 3877. doi:10.1093/mnras/stab2672

Gianninas A., Bergeron P., Ruiz M. T., 2011, ApJ, 743, 138

Green R. F., Liebert J., 1981, PASP, 93, 105

Harris H. C., et al., 2006, AJ, 131, 571

Holberg J. B., Bergeron P., 2006, AJ, 132, 1221. doi:10.1086/505938

Kawka A., Vennes S., Dupuis J., Chayer P., Lanz T., 2008, ApJ, 675, 1518. doi:10.1086/526411

Kepler S. O., et al., 2015, MNRAS, 446, 4078

Kepler S. O., et al., 2016, MNRAS, 455, 3413

Kilic M., Bergeron P., Kosakowski A., Brown W. R., Agüeros M. A., Blouin S., 2020, ApJ, 898, 84

Kilkenny D., Worters H. L., O'Donoghue D., Koen C., Koen T., Hambly N., MacGillivray H., Stobie R. S., 2016, MNRAS, 459, 4343

Kleinman S. J., et al., 2013, ApJS, 204, 5

Koester D., Voss B., Napiwotzki R., Christlieb N., Homeier D., Lisker T., Reimers D., et al., 2009, A&A, 505, 441. doi:10.1051/0004-6361/200912531

Koester D., Gänsicke B. T., Farihi J., 2014, A&A, 566, A34. doi:10.1051/0004-6361/201423691

Kong X., Luo A. L., Li X.-R., 2019, Research in Astronomy and Astrophysics, 19, 088

Korol V., Rossi E. M., Groot P. J., Nelemans G., Toonen S., Brown A. G. A., 2017, MNRAS, 470, 1894. doi:10.1093/mnras/stx1285

Korol V., Rossi E. M., Barausse E., 2019, MNRAS, 483, 5518. doi:10.1093/mnras/sty3440

Kowalski P. M., Saumon D., 2006, ApJL, 651, L137. doi:10.1086/509723

Kulkarni S. R., van Kerkwijk M. H., 2010, ApJ, 719, 1123. doi:10.1088/0004-637X/719/2/1123

Lajoie C.-P., Bergeron P., 2007, ApJ, 667, 1126. doi:10.1086/520926

Lallement R., Welsh B. Y., Vergely J. L., Crifo F., Sfeir D., 2003, A&A, 411, 447. doi:10.1051/0004-6361:20031214

Lamberts A., Blunt S., Littenberg T. B., Garrison-Kimmel S., Kupfer T., Sanderson R. E., 2019, MNRAS, 490, 5888. doi:10.1093/mnras/stz2834

Lawrence A., Warren S. J., Almaini O., Edge A. C., Hambly N. C., Jameson R. F., Lucas P., et al., 2007, MNRAS, 379, 1599. doi:10.1111/j.1365-2966.2007.12040.x

Liebert J., Dahn C. C., Monet D. G., 1988, ApJ, 332, 891. doi:10.1086/166699

Limoges M. M., Bergeron P., 2010, ApJ, 714, 1037

Limoges M. M., Bergeron P., Lépine S., 2015, ApJS, 219, 19

Magnier E. A., et al., 2013, ApJS, 205, 20

Manser C. J., et al., 2023, MNRAS,

Maoz D., Mazeh T., McQuillan A., 2015, MNRAS, 447, 1749. doi:10.1093/mnras/stu2577

Marsh T. R., Duck S. R., 1996, MNRAS, 278, 565

Marsh T. R., Gänsicke B. T., Steeghs D., Southworth J., Koester D., Harris V., Merry L., 2011, ApJ, 736, 95. doi:10.1088/0004-637X/736/2/95

Martin D. C., Fanson J., Schiminovich D., Morrissey P., Friedman P. G., Barlow T. A., Conrow T., et al., 2005, ApJL, 619, L1. doi:10.1086/426387

Martin D. C., GALEX Science Team, 2005, AAS

McCleery J., et al., 2020, MNRAS, 499, 1890

Mestel L., 1952, MNRAS, 112, 583. doi:10.1093/mnras/112.6.583

Mickaelian A. M., 2008, AJ, 136, 946

Morrissey P., GALEX Science Team, 2005, AAS

Morrissey P., Schiminovich D., Barlow T. A., Martin D. C., Blakkolb B., Conrow T., Cooke B., et al., 2005, ApJL, 619, L7. doi:10.1086/424734

Morrissey P., et al., 2007, ApJS, 173, 682

Napiwotzki R., et al., 2020, A&A, 638, A131

Nelemans G., Yungelson L. R., Portegies Zwart S. F., 2001, A&A, 375, 890. doi:10.1051/0004-6361:20010683

Nissanke S., Vallisneri M., Nelemans G., Prince T. A., 2012, ApJ, 758, 131. doi:10.1088/0004-637X/758/2/131

O'Donnell J. E., 1994, ApJ, 422, 158. doi:10.1086/173713

Press W. H., Flannery B. P., Teukolsky S. A., 1986, Numerical recipes. The art of scientific computing

Rebassa-Mansergas A., et al., 2016, MNRAS, 463, 1137

Rebassa-Mansergas A., Toonen S., Korol V., Torres S., 2019, MNRAS, 482, 3656

Redfield S., 2006, ASPC, 352, 79. doi:10.48550/arXiv.astro-ph/0601117

Reid I. N., 1996, AJ, 111, 2000. doi:10.1086/117936

Schlafly E. F., Finkbeiner D. P., 2011, ApJ, 737, 103. doi:10.1088/0004-637X/737/2/103

Schlegel D. J., Finkbeiner D. P., Davis M., 1998, ApJ, 500, 525. doi:10.1086/305772

Schmidt G. D., West S. C., Liebert J., Green R. F., Stockman H. S., 1986, ApJ, 309, 218

Stecher T. P., 1965, ApJ, 142, 1683. doi:10.1086/148462

Tremblay P. E., Bergeron P., Gianninas A., 2011, ApJ, 730, 128

Vanderburg A., Johnson J. A., Rappaport S., Bieryla A., Irwin J., Lewis J. A., Kipping D., et al., 2015, Natur, 526, 546. doi:10.1038/nature15527

Vanderburg A., Rappaport S. A., Xu S., Crossfield I. J. M., Becker J. C., Gary B., Murgas F., et al., 2020, Natur, 585, 363. doi:10.1038/s41586-020-2713-y

Vennes S., Smith R. J., Boyle B. J., Croom S. M., Kawka A., Shanks T., Miller L., Loaring N., 2002, MNRAS, 335, 673

Verbeek K., et al., 2012, MNRAS, 426, 1235

Vidrih S., et al., 2007, MNRAS, 382, 515

Vincent O., Bergeron P., Dufour P., 2023, arXiv, arXiv:2301.05209. doi:10.48550/arXiv.2301.05209

Wall R. E., Kilic M., Bergeron P., Rolland B., Genest-Beaulieu C., Gianninas A., 2019, MNRAS, 489, 5046

Wesemael F., Greenstein J. L., Liebert J., Lamontagne R., Fontaine G., Bergeron P., Glaspey J. W., 1993, PASP, 105, 761

Wheeler J. C., 2000, coca.book, 304

Winget D. E., Hansen C. J., Liebert J., van Horn H. M., Fontaine G., Nather R. E., Kepler S. O., et al., 1987, ApJL, 315, L77. doi:10.1086/184864

Winget D. E., Kepler S. O., 2008, ARA&A, 46, 157. doi:10.1146/annurev.astro.46.060407.145250

Yuan H. B., Liu X. W., Xiang M. S., 2013, MNRAS, 430, 2188. doi:10.1093/mnras/stt039